Bruno Miguel do Carmo Barroca

Graduate in Mechanical Engineering Sciences

Optimal shape and topology of multi-material microstructures in min-max stress design problems

Dissertation submitted in partial fulfillment
of the requirements for the degree of

Master of Science in
Mechanical Engineering

Adviser: Dr. Pedro Samuel Gonçalves Coelho,
Auxiliar Professor, NOVA University of Lisbon

Examination Committee

Chair: Prof. Dr. João Mário Burguete Botelho Cardoso
Rapporteur: Prof. Dr. José Arnaldo Pereira Leite Miranda Guedes

FACULDADE DE
CIÊNCIAS E TECNOLOGIA
UNIVERSIDADE NOVA DE LISBOA

December, 2019

Optimal shape and topology of multi-material microstructures in min-max stress design problems

"There is hardly any other branch of mathematical sciences in which abstract mathematical speculation and concrete physical evidence go so beautifully together and complement each other so perfectly."
Cornelius Lanczos

Acknowledgements

First off, I would like to thank my adviser, Professor Pedro Coelho, in particular for his invaluable guidance and fruitful discussions during the development of this dissertation, but also in general, for being a great teacher in the field of structural mechanics. I am deeply grateful for the introduction to the structural optimization subject, which culminated in the best experience I could ever imagine.

I acknowledge Professor José Miranda Guedes for sharing the software PREMAT and POSTMAT, the computational implementation of the asymptotic homogenization method for the planar elasticity problem. I would also like to thank him for his introductory classes on that same subject, which albeit not essential to the dissertation, I valued tremendously.

I would also like to thank the Department of Mechanical and Industrial Engineering of the Faculty of Sciences and Technology, for providing the necessary equipment to develop the dissertation. Furthermore, I am grateful to its professors for sharing their knowledge with me for the five year duration of my stay. Out of that group, I highlight Professor João Cardoso, who taught me Mechanics of Materials, and whose passion for the subject influenced me to choose structural mechanics as my specialization.

I am thankful for the structural mechanics colleagues with whom I shared office with, and the great spirit of companionship that was developed in this eight month time frame. I am grateful for how amazing the good moments were, but above all, how insignificant the bad ones actually felt, by having this group of people around me. I am particularly indebted to Tiago Pratas, for the countless hours spent both in and out of the laboratory, sharing and discussing out problems, as this was immensely important for the outcome of my work.

A massive shout out to all my friends, for making this academic journey as incredible as it turned out to be. I would particularly like to express my gratitude towards my closest group of friends, who throughout became almost like family for me.

Last, but certainly not least, I want to thank my parents for making all of this possible. Although they were far away, they always stood by my side, no matter what. They showed unconditional support through all my life, with my academic journey being no exception.

Abstract

The present dissertation seeks to optimize the unit cell of a two-dimensional cellular material, pursuing the minimization of the peak equivalent stress in the microstructure. This class of materials is particularly relevant to the design of lightweight structures. By minimizing the peak stress in the microstructure, it is possible to use material in a more rational way.

Given the periodic nature of the problem, asymptotic homogenization is employed to compute the stress distribution in the microstructure when a macroscopic load is applied, since periodicity boundary conditions are imposed. With this being a purely conceptual study, only three macroscopic loads are considered: the hydrostatic, biaxial, and pure shear ones.

Initially, the single-material problem is solved through shape optimization. Then, the potential to reduce the peak equivalent stress through the introduction of additional material phases is explored. Also with shape optimization, the influence of one additional material phase is studied. Additionally, topology optimization is used to discover the functionally graded material that minimizes the peak stress in the microstructure.

The obtained results show that an increased design flexibility always leads to milder stress states. The known theoretical results were successfully replicated, with minimal error measures associated. By increasing the number of material phases in the microstructure, peak stress reduction are attainable. A uniformly stressed microstructure is possible to obtain, by means of a functionally graded material.

Keywords: Homogenization, microstructure, multi-material, cellular material, shape optimization, topology optimization, functionally graded material, equivalent stress

Resumo

Esta dissertação tem como principal objetivo a otimização da célula unitária de um material celular bidimensional, tendo em vista a minimização do pico de tensão equivalente na microstrutura. Esta classe de materiais compósitos é relevante em aplicações onde o compromisso entre o baixo peso e a resistência mecânica são de grande importância. Ao minimizar a tensão máxima que se verifica na microstrutura, é possível uma utilização mais racional de material.

Dada a natureza periódica do problema, a homogeneização assintótica foi utilizada para simular o campo de tensões presente na microstrutura quando esta é sujeita a um carregamento macroscópico, pois pressupõe condições de fronteira de periodicidade. Sendo este trabalho de carácter conceptual, são apenas estudados três carregamentos distintos: o hidrostático, o biaxial, e o corte puro.

Inicialmente, é resolvido o problema para uma única fase de material através da otimização de forma. De seguida, é explorado o potencial de reduzir o pico de tensão para valores menores que o teórico, através da introdução de fases de material adicionais. Para uma fase de material adicional, é usada a otimização de forma. Adicionalmente, a otimização topológica é usada para descobrir o material com gradiente funcional que minimiza o pico de tensão.

Os resultados mostram que parametrizações mais flexíveis conduzem sempre a estados de tensão menos adversos. Os resultados teóricos foram replicados, obtendo-se medidas de erro bastante baixas. Ao aumentar o número de fases de material, é possível reduzir o pico de tensão, atingindo-se até a situação limite de um estado de tensão unifome em toda a microstrutura, com recurso a um material com gradiente funcional.

Palavras-chave: Homogeneização, microstrutura, multimaterial, material celular, otimização de forma, otimização topológica, material com gradiente funcional, tensão equivalente

Contents

List of Figures

List of Tables

Acronyms

FGM Functionally Graded Material

HS Hashin-Shtrikman

KKT Karush-Kuhn-Tucker

KM Kolosov-Muskelishvili

KS Kreisselmeier-Steinhauser

MMA Method of Moving Asymptotes

MMSO Multi-material Shape Optimization

RAMP Rational Approximation of Material Properties

SIMP Solid Isotropic Material Penalization

SMSO Single Material Shape Optimization

SQP Sequential Quadratic Programming

Symbols

ϕ Airy's stress function

z Artificial variable

f_i Body force

Γ Boundary of the domain

κ Bulk modulus (two-dimensional)

K Bulk modulus (three-dimensional)

χ^{mn} Characteristic displacement fields of a unit cell

$\boldsymbol{D}$ Characteristic macroscopic length

$\boldsymbol{d}$ Characteristic microscopic length

C_{ijkl} Compliance Tensor

ω Conformal mapping function

ρ Density variable

$\mathbf{u}$ Displacement field

Ω Domain

ε Ratio between the microscopic and macroscopic lengths

β Exponent of the EXP law for the volume calculation

$\mathbf{H}$ Hessian matrix

δ_{ij} Kronecker's delta

$\mathscr{L}$ Lagrangian function

λ Lamé's Constant

γ Lamination factor

$\mathbf{x}$ Macroscopic position

$\mathbf{u}^1$ Microscopic displacement field

$\mathbf{y}$ Microscopic position

n^e Number of elements

n^p Number of solid material phases

σ_{oct} Octahedral normal stress

τ_{oct} Octahedral shear stress

ν Poisson's ratio

ζ Position coordinate in the conformal mapping domain

μ Shear modulus, characteristic dimension of the rank-2 laminate

E_{ijkl} Stiffness tensor

w Strain energy density

ε_{ij} Strain tensor

σ_{ij} Stress tensor

$e^{0(mn)}$ Unit load step

Y Volume

$\boldsymbol{V}$ Volume fraction

σ^{VM} von-Mises equivalent stress

E Young's modulus

Chapter 1

Introduction

1.1 Motivation

Optimal design plays an important role on the design of structures where weight is a major concern, since it leads to the most effective distribution of material for the desired performance measure. However, the structures obtained through optimal design are frequently of very high complexity, meaning they are either impossible to manufacture with the current technology, or are highly cost-inefficient to. With the perfecting of the existing technological processes, and the introduction of new ones, like additive manufacturing, the boundary of what is possible to produce is in expansion. Thus, the mass production of components obtained by optimal design methodologies will likely grow, justifying the interest of structural optimization.

Usually, structural optimization is used in the context of the optimal design of macrostructures. Only in recent years has the optimization of microstructures gained relevancy. By considering two length scales (macro and microscale), the resulting optimal design is certainly different. As a consequence of the investigation efforts in this area, a new class of composite materials has arisen, cellular materials. These materials are composed by one solid phase and void, and are characterized by a unit cell that is repeated periodically in two or three dimensions.

Traditionally, structural optimization has revolved the problem of minimizing the strain energy, while imposing a maximum volume, or mass, of material. However, in real world applications, the stiffness of a structure is usually not the limiting factor, with the failure of the material usually being the main concern,which can be predicted through a criterion like the von-Mises equivalent stress for metallic materials.

Therefore, the discovery of cellular microstructures that minimize the peak equivalent stress would aid in the construction of lightweight macrostructures, while still guaranteeing failure

that does not occur, both at the macro and microscales.

1.2 Objectives

The present dissertation aims to be an exploratory work in the field of optimal microstructure design. For any particular macroscopic load, there is an optimal design of the microstructure that is able to minimize the peak stress to a minimum. As a proof of concept, three different macroscopic loads are used, being the hydrostatic, biaxial, and shear load.

For a single material microstructure, there is an attempt to replicate the existent theoretical results concerning the minimum peak stress value attainable, though in the particular case of the shear load there is no such benchmark. For this application, shape optimization will be employed.

Then, a homogeneous ring of a material phase softer than the base material of the plate will be added around the hole, in order to reduce the peak equivalent stress below the theoretical minimum. This method will be applied to the hydrostatic and biaxial load cases, and approached through shape optimization, using two different parametrization with varying complexity.

Finally, the potential to lower the maximum equivalent stress on the plate will be explored, through the use of a functionally graded material. At first, a shape optimization framework will be used, which involves a large number of homogeneous material rings around the hole. Subsequently, a topology optimization methodology is employed to allow for maximum flexibility of the Young's modulus distribution on the plate. This method guarantees a certain volume fraction of void, while allowing for a varying Young's modulus field throughout the plate.

Through the use of these approaches with increasing flexibility, the potential to lower the peak equivalent stress beyond the theoretical single material minimum will be unravelled.

1.3 Structure of the dissertation

The main body of this dissertation is divided in seven chapters, with the first being the current one, stating the motivation and objectives to be accomplished with this work, as well presenting the structure of the dissertation.

The second chapter is focused on the theory of linear elasticity. In its first part, the basics concepts behind it are briefly exposed, as the equations of equilibrium, the stiffness tensor of a material, among others. Then, an overview of the analytical stress determination methods is made, before exposing the application of the asymptotic homogenization to the linear elasticity problem.

Chapter 3 is dedicated to the theoretical foundations of structural optimization, where the standard optimization problem, approaches to the min-max problem and optimization algorithms are presented.

The fourth chapter is the state of the art, where a literature revision is made on the subject of this dissertation. It is divided in three sections. Firstly, the analytical advances to the problem of periodically repeating holes in a plate. Next, a brief review of the numerical advances is presented, with the main focus being stress constrained optimization of microstructures. Lastly, some literature concerning the stress field of a plate with a hole with a functionally graded ring of material around it is exposed, with those articles having mainly a theoretical nature.

Chapter 5 is focused on the implementation of the optimization problems. In the first place, the shape optimization problem is formulated, all the parametrizations used are disclosed, and the main practical issues encountered are presented, discussing the way in which they were solved. Then, the topology optimization problem is formulated. A few volume calculation schemes are presented, which allow for the solution of the optimization problem to be a functionally graded unit cell. With them come some complications, which are also discussed.

The sixth chapter is where the obtained results for every macroscopic load and respective parametrization are discussed, comparing the various approaches with the known theoretical results, and with one another. An attempt is made to explain why every technique to lower the peak equivalent stress actually works, and if not, the reason why.

Lastly, in the seventh chapter, an overview of the results obtained is made, recognizing the potential of the methods used. Also, some future developments regarding this subject are presented, as a follow-up to the work developed in the present dissertation.

Chapter 2

Theory of Linear Elasticity

2.1 Introduction

The property of elasticity is common to almost all materials. When an elastic body is subject to an arbitrary load, it deforms in such a way that equilibrium is attained. If the external loads do not exceed a certain limit, the body returns to its undeformed state, prior to the application of the external forces. In practice, every material has a yield strength associated with it. If stresses caused by the boundary conditions surpass that limit, the material enters the plastic domain, and the body is no longer able to completely resume its initial form.

In the context of this dissertation, bodies are said to be perfectly elastic, therefore plasticity is never attained. All material phases are assumed to be homogeneous and linear elastic, meaning its elastic properties have no dependence on strain, and do not vary from point to point. Only statics problems are considered, thus there are enough constraints to prevent rigid body motion and inertia forces are negligible, so no oscillatory motion is possible. Solving a linear elasticity problem translates to solving the differential equations of equilibrium for certain imposed boundary conditions, as will be shown. This chapter is mainly based on [3, 50].

2.2 The Basics

2.2.1 Differential Equations of Equilibrium

Consider the equilibrium of an infinitesimal cube (figure 2.1). When the length of the edges approaches zero, the equilibrium equations are obtained in the differential form, as in:

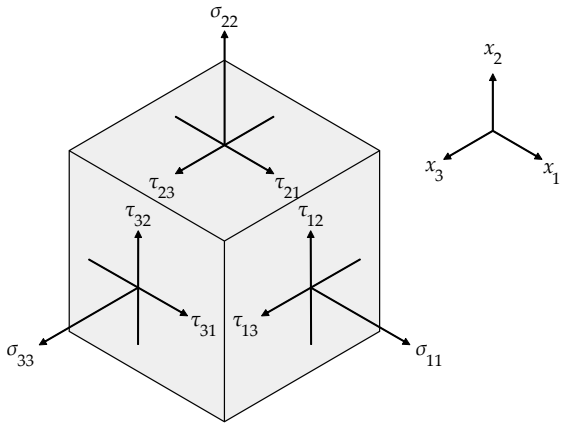

Figure 2.1: Static equilibrium of an infinitesimal cube

$$\begin{aligned}
\frac{\partial \sigma_{11}}{\partial x_1} + \frac{\partial \tau_{21}}{\partial x_2} + \frac{\partial \tau_{31}}{\partial x_3} + f_1 = 0 \\
\frac{\partial \tau_{12}}{\partial x_1} + \frac{\partial \sigma_{22}}{\partial x_2} + \frac{\partial \tau_{32}}{\partial x_3} + f_2 = 0 \\
\frac{\partial \tau_{13}}{\partial x_1} + \frac{\partial \tau_{23}}{\partial x_2} + \frac{\partial \sigma_{33}}{\partial x_3} + f_3 = 0
\end{aligned} \tag{2.1}$$

The terms f_i correspond to body forces acting on the cube, such as the effect of gravity or a magnetic field. The stress state of any given point of a body is fully defined if all the stress components represented in 2.1 are known, for any orientation of the three directions considered, as long as they are orthogonal between them. Cauchy's stress tensor, σ_{ij} is defined as:

$$\sigma_{ij} = \begin{bmatrix} \sigma_{11} & \tau_{12} & \tau_{13} \\ \tau_{21} & \sigma_{22} & \tau_{23} \\ \tau_{31} & \tau_{32} & \sigma_{33} \end{bmatrix} \tag{2.2}$$

In order for the body to be in an equilibrium state, there must exist equilibrium in both forces and momentums. Referring to 2.1, it can be stated that static equilibrium is only possible if Cauchy's stress tensor is symmetric, and thus, it is fully defined with 6 components.

2.2.2 Compatibility Equations

The equations of equilibrium and the boundary conditions are not sufficient for the determination of the six stress components. The problem is a statically indeterminate one, and in order to obtain the solution the elastic deformation of the body must also be considered.

When a body is subject to a load, every point in the material domain assumes a position, in its new equilibrium state. The displacement field, **u**, is the change of position for every macroscopic material point **x**.

$$\mathbf{u}(\mathbf{x}) = \begin{bmatrix} u_1(x_1, x_2, x_3) \\ u_2(x_1, x_2, x_3) \\ u_3(x_1, x_2, x_3) \end{bmatrix} \tag{2.3}$$

Once knowing the displacement field, it is possible to calculate the strain field. Strain is a measure of how much a particular point contributes to the displacement function, thus, for its determination, the value of the displacement function is of no particular interest, only its rate of change in each direction. Assuming small displacements:

$$\varepsilon_{ij} = \frac{1}{2}\left(\frac{\partial u_i}{\partial x_j} + \frac{\partial u_j}{\partial x_i}\right) = \begin{bmatrix} \varepsilon_{11} & \varepsilon_{12} & \varepsilon_{13} \\ \varepsilon_{21} & \varepsilon_{22} & \varepsilon_{23} \\ \varepsilon_{31} & \varepsilon_{32} & \varepsilon_{33} \end{bmatrix} \tag{2.4}$$

As seen in 2.4, six components of strain, ε_{ij}, are fully determined only by the three components of **u**. Therefore, the strain components cannot be arbitrary functions, independent of one another, which could lead to a solution with no sensible physical meaning. In fact, through manipulation of the definition of strain it is possible to obtain six differential relations, known as conditions of compatibility.

$$\begin{aligned}
&\frac{\partial^2 \varepsilon_{11}}{\partial x_2^2} + \frac{\partial^2 \varepsilon_{22}}{\partial x_1^2} = 2\frac{\partial^2 \varepsilon_{12}}{\partial x_1 \partial x_2} && \frac{\partial^2 \varepsilon_{11}}{\partial x_2 \partial x_3} = \frac{\partial}{\partial x_1}\left(-\frac{\partial \varepsilon_{23}}{\partial x_1} + \frac{\partial \varepsilon_{13}}{\partial x_2} + \frac{\partial \varepsilon_{12}}{\partial x_3}\right) \\
&\frac{\partial^2 \varepsilon_{22}}{\partial x_3^2} + \frac{\partial^2 \varepsilon_{33}}{\partial x_2^2} = 2\frac{\partial^2 \varepsilon_{23}}{\partial x_2 \partial x_3} && \frac{\partial^2 \varepsilon_{22}}{\partial x_1 \partial x_3} = \frac{\partial}{\partial x_2}\left(\frac{\partial \varepsilon_{23}}{\partial x_1} - \frac{\partial \varepsilon_{13}}{\partial x_2} + \frac{\partial \varepsilon_{12}}{\partial x_3}\right) \\
&\frac{\partial^2 \varepsilon_{33}}{\partial x_1^2} + \frac{\partial^2 \varepsilon_{11}}{\partial x_3^2} = 2\frac{\partial^2 \varepsilon_{13}}{\partial x_1 \partial x_3} && \frac{\partial^2 \varepsilon_{33}}{\partial x_1 \partial x_2} = \frac{\partial}{\partial x_3}\left(\frac{\partial \varepsilon_{23}}{\partial x_1} + \frac{\partial \varepsilon_{13}}{\partial x_2} - \frac{\partial \varepsilon_{12}}{\partial x_3}\right)
\end{aligned} \tag{2.5}$$

2.2.3 Constitutive Law

In the context of mechanics of materials, a constitutive law is a mathematical model that can accurately predict the mechanical behaviour of a structure subject to any load. Linear relations between stress and strain are known as Hooke's Law. Introducing the fourth order stiffness tensor E_{ijkl} , Hooke's Law states that the stress and strain tensors may be related by the expression:

$$\sigma_{ij} = E_{ijkl}\varepsilon_{kl} \tag{2.6}$$

Hooke's Law can also be considered in its inverse form, by inverting the stiffness tensor, introducing the compliance tensor C_{ijkl}.

$$\varepsilon_{ij} = C_{ijkl}\sigma_{kl} \tag{2.7}$$

Due to the dimension of the stiffness tensor, the inverse fourth order tensor can be computed as follows:

$$E_{ijkl}C_{ijkl} = \frac{1}{2}(\delta_{ik}\delta_{jl} + \delta_{il}\delta_{jk}) \tag{2.8}$$

Due to the symmetric nature of both stress and strain tensors, it is found that the stiffness also has symmetries, meaning that the ij and kl are interchangeable between them, as in equation 2.9a. Furthermore, the relation in 2.9b comes as an implication of Schwarz theorem when calculating the strain energy of a body.

$$E_{ijkl} = E_{jikl} = E_{ijlk} \tag{2.9a}$$

$$E_{ijkl} = E_{klij} \tag{2.9b}$$

It comes as a consequence that E_{ijkl} only has, at most, 21 independent coefficients. It is possible to write 2.6 in its matrix form:

$$\begin{bmatrix} \sigma_{11} \\ \sigma_{22} \\ \sigma_{33} \\ \sigma_{23} \\ \sigma_{13} \\ \sigma_{12} \end{bmatrix} = \begin{bmatrix} E_{1111} & E_{1122} & E_{1133} & E_{1123} & E_{1113} & E_{1112} \\ E_{2211} & E_{2222} & E_{2233} & E_{2223} & E_{2213} & E_{2212} \\ E_{3311} & E_{3322} & E_{3333} & E_{3323} & E_{3313} & E_{3312} \\ E_{2311} & E_{2322} & E_{2333} & E_{2323} & E_{2313} & E_{2312} \\ E_{1311} & E_{1322} & E_{1333} & E_{1323} & E_{1313} & E_{1312} \\ E_{1211} & E_{1222} & E_{1233} & E_{1223} & E_{1213} & E_{1212} \end{bmatrix} \begin{bmatrix} \varepsilon_{11} \\ \varepsilon_{22} \\ \varepsilon_{33} \\ \varepsilon_{23} \\ \varepsilon_{13} \\ \varepsilon_{12} \end{bmatrix} \tag{2.10}$$

In fact, a fair amount of practical applications may be simplified to cases of planar stress or strain, meaning they have no components in one direction, as exemplified on 2.2. In those particular situations, the general Hooke's Law is simplified.

For an isotropic material, the relations shown on 2.11a and 2.11b are valid for plane stress, and 2.11c and 2.11d for plane strain, in both stiffness and compliance forms respectively.

$$\begin{bmatrix} \varepsilon_{11} \\ \varepsilon_{22} \\ 2\varepsilon_{12} \end{bmatrix} = \frac{1}{E}\begin{bmatrix} 1 & -\nu & 0 \\ -\nu & 1 & 0 \\ 0 & 0 & 2(1+\nu) \end{bmatrix} \begin{bmatrix} \sigma_{11} \\ \sigma_{22} \\ \sigma_{12} \end{bmatrix} \tag{2.11a}$$

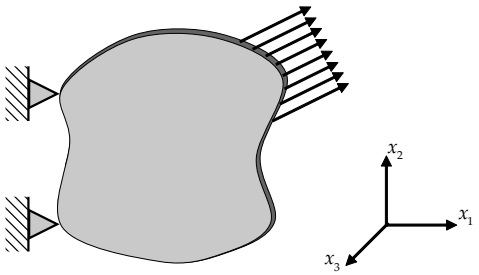

Figure 2.2: Plane stress

$$\begin{bmatrix}\sigma_{11}\\ \sigma_{22}\\ \sigma_{12}\end{bmatrix} = \frac{E}{1-\nu^2}\begin{bmatrix}1 & \nu & 0\\ \nu & 1 & 0\\ 0 & 0 & \frac{1-\nu}{2}\end{bmatrix}\begin{bmatrix}\varepsilon_{11}\\ \varepsilon_{22}\\ 2\varepsilon_{12}\end{bmatrix} \tag{2.11b}$$

$$\begin{bmatrix}\varepsilon_{11}\\ \varepsilon_{22}\\ 2\varepsilon_{12}\end{bmatrix} = \frac{1}{E}\begin{bmatrix}1-\nu^2 & -\nu(1+\nu) & 0\\ -\nu(1+\nu) & 1-\nu^2 & 0\\ 0 & 0 & 2(1+\nu)\end{bmatrix}\begin{bmatrix}\sigma_{11}\\ \sigma_{22}\\ \sigma_{12}\end{bmatrix} \tag{2.11c}$$

$$\begin{bmatrix}\sigma_{11}\\ \sigma_{22}\\ \sigma_{12}\end{bmatrix} = \begin{bmatrix}\lambda+2\mu & \lambda & 0\\ \lambda & \lambda+2\mu & 0\\ 0 & 0 & \mu\end{bmatrix}\begin{bmatrix}\varepsilon_{11}\\ \varepsilon_{22}\\ 2\varepsilon_{12}\end{bmatrix} \tag{2.11d}$$

E is the Young's Modulus and ν is the Poisson's Ratio, which are known as the engineering constants. $\mu = \frac{E}{2(1+\nu)}$ is the Shear Modulus, and $\lambda = \frac{E\nu}{(1+\nu)(1-2\nu)}$ is Lamé's Constant. Additionally there is the three-dimensional Bulk Modulus, $K = \frac{E}{3(1-2\nu)}$. The latter is of importance for studies in theory of elasticity, namely the optimal stress distribution on a perforated plate.

The two-dimensional stiffness tensor plays an important role in the mathematical methods of theory of elasticity, since it can be diagonalized, allowing to rewrite Hooke's Law in a way that allows for simplifications. This diagonalized version of the stiffness tensor is presented in equation 2.12. Its usefulness in the context of the present dissertation is an expedite way to calculate the macroscopic elastic coefficients of a material. When the material is isotropic, the two-dimensional Bulk Modulus, κ, is obtained as an eigenvalue of the stiffness matrix (the largest eigenvalue), with the two other being the Shear Modulus, $\mu = \mu_1 = \mu_2$. However, if the material has cubic symmetry, the two lower eigenvalues correspond to two different Shear Moduli values, μ_1 and μ_2. This version of the stiffness tensor has no physical interpretation, and

is used only to evaluate the bulk modulus of a material in an expedite way, when the stiffness tensor is already known.

$$E_{ij} = \begin{bmatrix} 2\kappa & 0 & 0 \\ 0 & 2\mu_1 & 0 \\ 0 & 0 & 2\mu_2 \end{bmatrix} \tag{2.12}$$

The two-dimensional bulk modulus does not have as much of a physical interpretation as its three-dimensional counterpart. For an isotropic material, it is defined as $\kappa = \frac{E}{2(1-\nu)}$.

2.2.4 Stress Function

In sections 2.2.1 and 2.2.2, the equations that govern the elasticity problem were presented. It has been shown that the solution of two-dimensional elasticity problems corresponds to the integration of the differential equations of equilibrium along with the compatibility equations, by imposing the boundary conditions. In two dimensions, equations 2.13a and 2.13b must be satisfied, assuming no body forces. Equation 2.13b is obtained manipulating the condition of compatibility, assuming plane stress.

$$\begin{aligned} \frac{\partial \sigma_{xx}}{\partial x} + \frac{\tau_{xy}}{\partial y} &= 0 \\ \frac{\partial \sigma_{yy}}{\partial y} + \frac{\tau_{xy}}{\partial x} &= 0 \end{aligned} \tag{2.13a}$$

$$\left(\frac{\partial^2}{\partial x^2} + \frac{\partial^2}{\partial y^2}\right)(\sigma_{xx} + \sigma_{yy}) = 0 \tag{2.13b}$$

In order to facilitate the analytical stress determination procedure, Airy's Stress Function ϕ was introduced, which can be obtained by differentiating the stress at any given point, as in

$$\begin{aligned} \sigma_{xx} &= \frac{\partial^2 \phi}{\partial x^2} \\ \sigma_{yy} &= \frac{\partial^2 \phi}{\partial y^2} \\ \tau_{xy} &= -\frac{\partial^2 \phi}{\partial x \partial y} \end{aligned} \tag{2.14}$$

Such formulation of the stress field guarantees they respect both the equilibrium and compatibility equations. By substituting Hooke's Law and Airy's Stress Function into 2.5, it is obtained a relation that every suitable stress function must verify, in order to generate a feasible stress field.

$$\frac{\partial^4\phi}{\partial x^4} + 2\frac{\partial^4\phi}{\partial x^2\partial y^2} + \frac{\partial^4\phi}{\partial y^4} \equiv \nabla^2(\nabla^2\phi) \equiv \nabla^4\phi = 0 \tag{2.15}$$

Any function $\phi(x, y)$ that satisfies this relation will satisfy the governing equations for equilibrium and geometric compatibility, assuming linear elasticity. In order to obtain a non-trivial solution, the boundary conditions must be imposed. Although it results in a difficult task, since a general solution for the equation does not exist, it can be proven that a solution exists, and is unique.

2.2.5 Failure Criterion

In its most generic form, any given point of the material domain has six independent components of stress, but the yield stress is known for a linear elastic isotropic material only when it is subject to an uniaxial load. In order to understand if the material surpasses its elastic limit, an equivalent stress is used to compare with the yield stress. Such equivalent stress must contemplate the effects of every component of the stress tensor, and combine them into one single scalar value.

Von-Mises's equivalent stress is among the most used criteria in engineering. It starts by remarking that the strain energy density, w, of a body can be separated into two components: one associated with volumetric contraction or expansion, and the shear strain energy.

$$w^e = \frac{1}{2K}\sigma_{oct}^2 + \frac{3}{4\mu}\tau_{oct}^2 \tag{2.16}$$

Normal octahedral stress, σ_{oct}, does not contribute for the entry on the plastic zone, only the shear component, τ_{oct}, does. This statement leads to von-Mises's failure criterion, also known as maximum distortion energy criterion, which states that plasticity is attained when the distortion energy reaches a critical value:

$$w_d^e = \frac{3}{4G}\tau_{oct}^2 \leq w_{crit} \tag{2.17}$$

Thus, by knowing the distortion energy associated with entering the plastic domain by means of an uniaxial load, it is possible to check if the material yields, given any stress state. The critical energy value for an uniaxial load is:

$$w_{crit} = \frac{3}{4G}\left[\frac{1}{3}\sqrt{2\sigma_y^2}\right]^2 = \frac{1}{6G}\sigma_y^2 \tag{2.18}$$

By writing down the octahedral shear stress as a function of the components of Cauchy's stress tensor, it is now possible to determine if plasticity is attained for any complex stress state

on a given material point, assuming the material is a linear elastic isotropic one. The von-Mises equivalent stress (equation 2.19), σ^{VM}, should be compared with the yield stress for the uniaxial load, σ_y, in order to evaluate the failure, or not, of the material.

$$\sigma^{VM} = \sqrt{\frac{1}{2}\left[(\sigma_{11} - \sigma_{22})^2 + (\sigma_{22} - \sigma_{33})^2 + (\sigma_{33} - \sigma_{11})^2\right] + 3\left(\tau_{12}^2 + \tau_{23}^2 + \tau_{13}^2\right)} \tag{2.19}$$

2.3 Analytical Stress Function Determination

2.3.1 Introduction

The theory of elasticity has a considerable number of applications in engineering problems. Although nowadays most problems can be swiftly solved by using the finite element method, it is fundamental to have a solid knowledge of the theoretical approaches to simple elasticity problems, as it helps to make sense and critically judge the numerically obtained results.

2.3.2 The Circular Hole

Probably the most well known explicit expression for stress distributions is the one around a circular hole, derived by Kirsch [31], in 1898. Figure 2.3 represents an infinite plate with a circular hole, subject to a uniform tension of magnitude σ_∞. If there is a geometrical perturbation in the plate, the stress distribution on its neighbourhood is changed, but when far enough, the change is negligible. Equation 2.15 can be expressed in terms of polar coordinates, as in:

$$\left(\frac{\partial^2}{\partial r^2}+\frac{1}{r}\frac{\partial}{\partial r}+\frac{1}{r^2}\frac{\partial^2}{\partial\theta^2}\right)\left(\frac{\partial^2\phi}{\partial r^2}+\frac{1}{r}\frac{\partial\phi}{\partial r}+\frac{1}{r^2}\frac{\partial^2\phi}{\partial\theta^2}\right)=0 \tag{2.20}$$

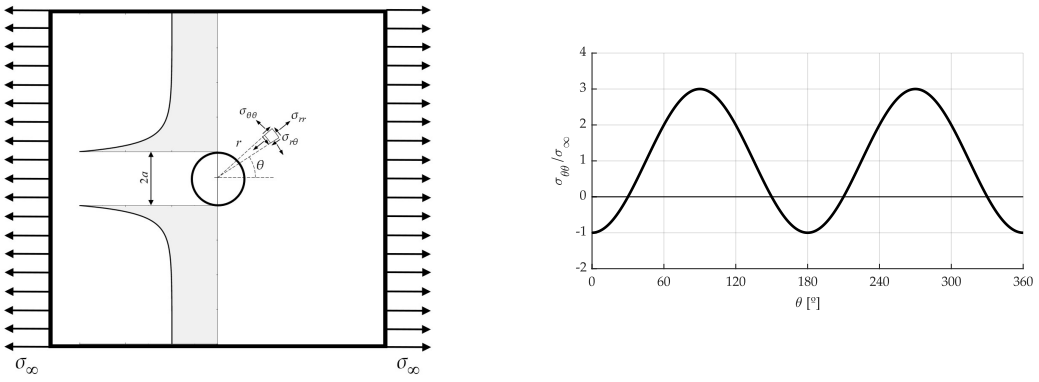

a. Stress distribution along r

b. Stress distribution along θ

Figure 2.3: Effect of circular hole on stress distribution on an infinite plate - uniaxial load

By noticing the problem has symmetry about the lines $\theta = 0$ and $\theta = \pi/2$, the stress function must be of the form:

$$\phi = f(r)\cos 2\theta \tag{2.21}$$

Once the form of the stress function is inserted into the compatibility equation, it is possible to obtain the general solution of the differential equation:

$$f(r) = Ar^2 + Br^4 + C\frac{1}{r^2} + D \tag{2.22}$$

There are four integration constants, thus four boundary conditions must be found. When distant enough from the hole, the stresses are the same as in a plate that is not weakened (equation 2.23a). Furthermore, since the edge of the hole is free from external forces, the stresses along the radius direction must be zero, as expressed in equation 2.23b.

$$\begin{aligned} \sigma_{rr}\Big|_{r=\infty} &= \frac{1}{2}\sigma_\infty(1+\cos 2\theta) \\ \tau_{r\theta}\Big|_{r=\infty} &= -\frac{1}{2}\sigma_\infty \sin 2\theta \end{aligned} \tag{2.23a}$$

$$\begin{aligned} \sigma_{rr}\Big|_{r=a} &= 0 \\ \tau_{r\theta}\Big|_{r=a} &= 0 \end{aligned} \tag{2.23b}$$

By imposing the boundary conditions, the integration constants can be obtained. It is found that $A = \frac{\sigma_\infty}{4}$, $B = 0$, $C = -\frac{a^2}{4}\sigma_\infty$ and $D = \frac{a^2}{2}\sigma_\infty$. By substituting these values into 2.22, the stress distribution is now known.

$$\begin{aligned} \sigma_{rr} &= \frac{\sigma_\infty}{2}\left(1-\frac{a^2}{r^2}\right) + \frac{\sigma_\infty}{2}\left(1+\frac{3a^4}{r^4}-\frac{4a^2}{r^2}\right)\cos 2\theta \\ \sigma_{\theta\theta} &= \frac{\sigma_\infty}{2}\left(1+\frac{a^2}{r^2}\right) - \frac{\sigma_\infty}{2}\left(1+\frac{3a^4}{r^4}\right)\cos 2\theta \\ \tau_{r\theta} &= -\frac{\sigma_\infty}{2}\left(1-\frac{3a^4}{r^4}+\frac{2a^2}{r^2}\right)\sin 2\theta \end{aligned} \tag{2.24}$$

It can be seen that $\sigma_{\theta\theta}$ is greatest in the edge of the circular hole, when $\theta = \pi/2$ or $3\pi/2$. The stress state in that point is the harshest of the whole domain, of value $3\sigma_\infty$. When $\theta = 0$ and π, the material is subject to compression in the angular direction, with the same intensity as the uniform stress applied at the edge of the plate, as can be seen in figure 2.3b. There is no shear stress in the cross section $\theta = \pi/2$, as a direct consequence of Kirsch's equations. Furthermore, by analysing the normal components of stress, it can be noticed that the equivalent von-Mises stress rapidly converges to the unity, as shown in figure 2.3a, meaning the stress concentration around a hole has a localized character, and its effects may be neglected when far enough from the geometrical perturbation.

The stress distribution for any combination of uniform stresses applied on the edges of the plate can be obtained by superposition of the uniaxial case, since it is linear elasticity. As such, the solutions for the unit hydrostatic and shear loads are presented in figures 2.4 and 2.5.

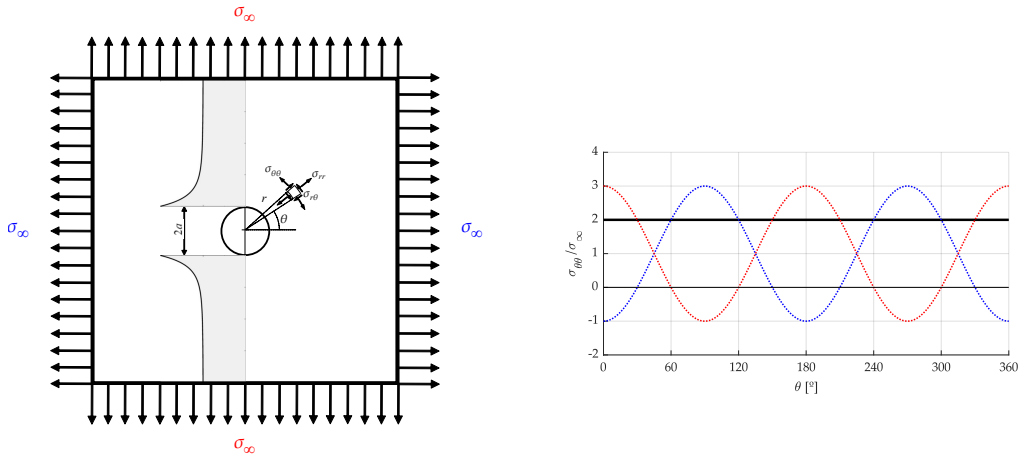

a. Stress distribution along r b. Stress distribution along θ

Figure 2.4: Effect of circular hole on stress distribution on an infinite plate - hydrostatic load

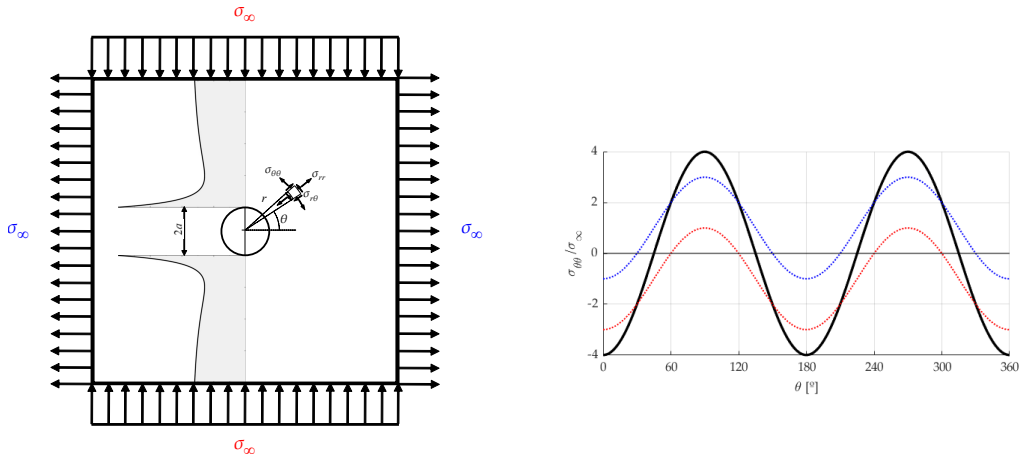

a. Stress distribution along r b. Stress distribution along θ

Figure 2.5: Effect of circular hole on stress distribution on an infinite plate - shear load

2.3.3 Complex Potentials

In broad terms, an analytical function of complex variable $f(z)$ can be regarded as a function of x and y ($z = x + iy$), having a defined derivative with regards to z, being the same for all directions of Δz in the point z. Thus

$$\begin{aligned} \frac{\partial}{\partial x} f(z) &= \frac{\partial}{\partial z} f(z) \frac{\partial z}{\partial x} = f'(z) \frac{\partial z}{\partial x} = f'(z) \\ \frac{\partial}{\partial y} f(z) &= \frac{\partial}{\partial z} f(z) \frac{\partial z}{\partial y} = f'(z) \frac{\partial z}{\partial y} = i f'(z) \end{aligned} \tag{2.25}$$

If $f(z)$ is put in the form $\alpha(x, y) + i\beta(x, y)$, the Cauchy-Riemann equations may be derived, which every analytical function verifies.

$$\frac{\partial \alpha}{\partial x} = \frac{\partial \beta}{\partial y} \qquad \frac{\partial \alpha}{\partial y} = -\frac{\partial \beta}{\partial x} \tag{2.26}$$

By differentiation and addition, α or β may be eliminated, originating Laplace's equation. Any function solution of that equation is said to be a harmonic function.

$$\frac{\partial^2 \alpha}{\partial x^2} + \frac{\partial^2 \alpha}{\partial y^2} = 0 \qquad \frac{\partial^2 \beta}{\partial x^2} + \frac{\partial^2 \beta}{\partial y^2} = 0 \tag{2.27}$$

In order to have stress defined as a function of complex variable, a function in the same form of 2.15 is going to be considered. Should ψ be any harmonic function of x and y, by applying the laplacian operator.

$$\nabla^2(x\varphi) \equiv \left(\frac{\partial^2}{\partial x^2} + \frac{\partial^2}{\partial y^2} \right)(x\varphi) = x\left(\frac{\partial^2 \varphi}{\partial x^2} + \frac{\partial^2 \varphi}{\partial y^2} \right) + 2\frac{\partial \varphi}{\partial x} \tag{2.28}$$

By the definition of harmonic function, the right parenthesis of equation 2.28 is zero, and $\partial\psi/\partial x$ is also harmonic. Through a second application of the laplacian operator, an equation similar to 2.15 is obtained.

$$\nabla^2\left(\nabla^2(x\varphi)\right) \equiv \left(\frac{\partial^4}{\partial x^4} + 2\frac{\partial^4}{\partial x^2 \partial y^2} + \frac{\partial^4}{\partial x^4} \right)(x\varphi) = 0 \tag{2.29}$$

The same can be said to the ψ function itself, or $y\psi$. It can be shown that $r^2\psi \equiv (x^2 + y^2)\psi$ too satisfies the differential equation. Recalling equation 2.13b and noticing $\nabla^2\phi$ is harmonic, comes that $\sigma_{xx} + \sigma_{yy}$ is also a harmonic function. This comes in useful when considering the general solution of a problem in polar coordinates.

It is possible to prove that any stress function is expressible in the form

$$\phi = \mathrm{Re}[\bar{z}\varphi(z) + \chi(z)] \tag{2.30}$$

Where $\bar{z}$ denotes the conjugate of z, and $\varphi(z)$ and $\chi(z)$ are two suitably chosen analytical functions. For every choice of $\varphi(z)$ and $\chi(z)$, 2.30 is always a solution of the differential equation 2.15. By defining $\psi(z) = d\chi/dz$, field equations for the plane problem can be expressed as

$$\sigma_{xx} + \sigma_{yy} = 4\,\mathrm{Re}[\varphi'(z)] \tag{2.31a}$$

$$\sigma_{yy} - \sigma_{xx} + 2i\tau_{xy} = 2[\overline{z}\varphi''(z) + \psi'(z)] \tag{2.31b}$$

φ and ψ are known as KM (Kolosov-Muskelishvili) potentials. They can be determined by imposing the stress and displacement boundary conditions (equations 2.32a and 2.32b respectively).

$$\varphi(z) + z\overline{\varphi'(z)} + \overline{\psi(z)} = \pm i \int_S \left(X_n + iY_n\right) ds \tag{2.32a}$$

$$\kappa\varphi(z) + z\overline{\varphi'(z)} - \overline{\psi(z)} = 2G(u + iv) \tag{2.32b}$$

2.3.4 Muskhelishvili's Method

The determination of the stress function by the classical method requires a suitable set of coordinates, and a clever selection of the general form of the complex potentials. As such, it is limited to solving problems involving simple shapes and parametrizations. More powerful and general methods have been developed for deducing the potentials directly from the boundary conditions [49].

In order to find the two complex potentials that lead to the solution of the elasticity problem, it is advantageous to replace the general complex variable z by a new complex variable ζ, defined by the relation shown in 2.33, given that $\omega(\zeta)$ is a suitably chosen function of ζ. Any point given by the complex coordinate $\zeta = \xi + i\eta$ in the ζ plane has a corresponding point in the z plane, with $z = \omega(\zeta)$.

$$z = \omega(\zeta) \tag{2.33}$$

The function $\omega(\zeta)$ is an analytical function such that a point P' in the ζ plane maps into only one point P on the original plane. In general, smooth curves $P'Q'$ map into another smooth curve PQ. For elasticity problems involving one singular noncircular hole in an infinite material medium, the mapping function $\omega(\zeta)$ is chosen so that the curve L maps from the unit circle centered at the origin in the ζ plane, as can be seen in figure 2.6.

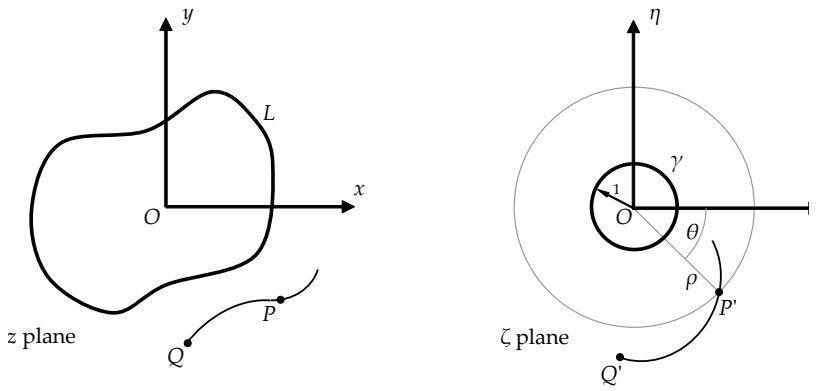

Figure 2.6: Conformal Mapping

Essentially, the introduction of the conformal mapping function allows for the problem to be solved in the ζ domain, and revert the change of variables back to the original problem. This allows for more complicated problems to be solved, where boundaries are not necessarily defined by an explicit analytical equation, or where the form of the final solution is known beforehand. As an example, this makes the problem of calculating the stress field on an infinite plate with an elliptic hole (figure 2.7) much easier than with the simple complex potential method.

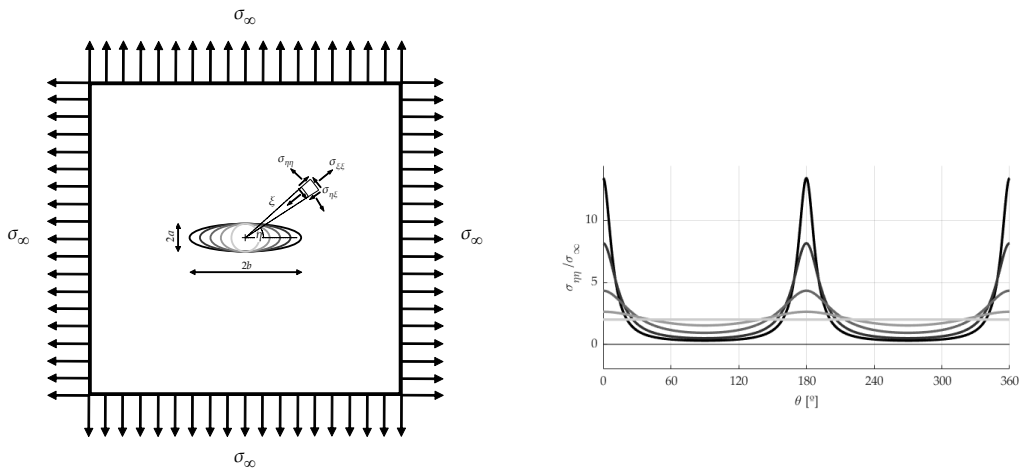

a. Infinite plate with an elliptic hole

b. Stress distribution along the free edge of the hole

Figure 2.7: Effect of an elliptic hole on the stress distribution on an infinite plate - hydrostatic load

2.4 Asymptotic Homogenization

In the context of this dissertation, every evaluation of the objective function implies solving an elasticity problem in a microstructure, when subject to some macroscopic applied load. In order to make the optimization process both faster and more accurate, one can use the homogenization theory to solve said elasticity problem [26, 43].

Consider the elasticity problem comprised by an heterogeneous medium, for example, a fibrous composite or a porous material. It is intended to understand the mechanical behaviour (displacements $\mathbf{u}^\epsilon$ and stresses $\boldsymbol{\sigma}^\epsilon$) of a representative volume of the periodic domain subject to body forces $\mathbf{f}$, applied stresses on the boundary $\mathbf{t}$ and imposed displacements $\mathbf{u}$. This is the classic elasticity problem seen in 2.8, which can be translated to a system of differential equations, and solved by imposing its boundary conditions.

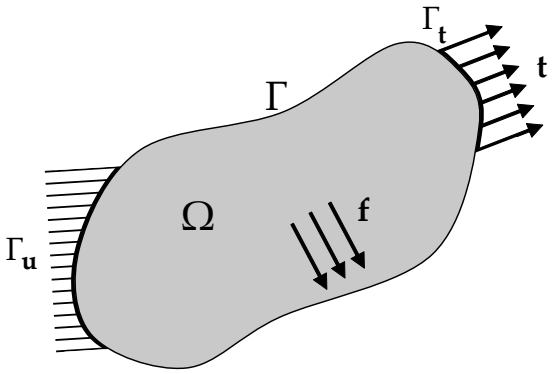

Figure 2.8: Generic elasticity problem

When there is a low amount of heterogeneities, the stress field may be obtained analytically, for example, by means of the Airy stress function, or numerically, using the finite element method. In the particular case of a material with periodic microstructure, the use of the finite element method is limited by the refinement of the mesh used and the number of periodicities modelled. The computational cost associated with the problem may become prohibitive, as the number of degrees of freedom of the system increases dramatically.

The general idea of homogenization theory is to replace the heterogeneous medium by an homogeneous equivalent one, with the average mechanical properties of the former. This approximation, as will be shown ahead, is a linear combination of the effects of both the macro and microscales, and should replicate the real behaviour of said heterogeneous material. The homogenization process involves solving elasticity problems in the periodic unit cell (local

problem, where the equilibrium equations and constitutive laws are known) and then contemplating its effect on the macroscopic scale (global problem). Figure 2.9 briefly exposes the three fundamental parts of the asymptotic homogenization method.

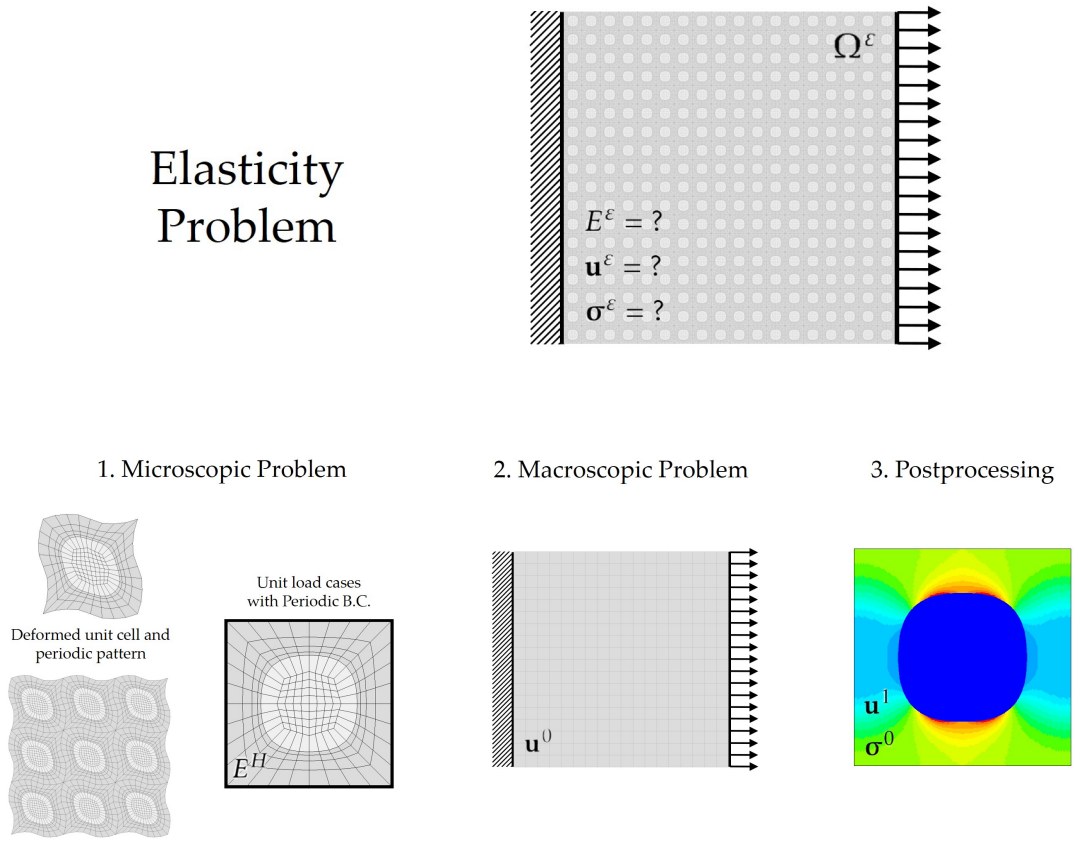

Figure 2.9: Homogenization process

The present dissertation applies the homogenization theory to periodic media based on an asymptotic expansion on two scales. This approach allows for a expeditious and precise approximation of the stress field of a unit cell subject to a load, without the need to numerically model a large amount of periodicities to guarantee accurate results. Such simplification may be made to the real problem provided that four hypotheses can be verified, which are presented in the following subsection.

2.4.1 Simplifying Assumptions

The homogenization theory assumes that the distribution of heterogeneity is periodic throughout the macroscopic domain. Let $\mathbf{u}(\mathbf{x}, \mathbf{y})$ be a generic multivariable function. The function is said to be periodic in the variable $\mathbf{y}$ should it verify the following condition:

$$\mathbf{x} \in \Omega, (\mathbf{x} + \mathbf{y}) \in \Omega \Rightarrow \mathbf{u}(\mathbf{x} + \mathbf{y}) = \mathbf{u}(\mathbf{x}) \tag{2.34}$$

The periodicity condition does not imply that the microstructure is the same all over the macroscopic domain. Smooth transitions of topology of the unit cell are acceptable as long as periodicity is still verified locally. Therefore, asymptotic homogenization is only applicable to periodic, or *quasi*-periodic materials.

Secondly, the macroscopic boundary conditions attributed to each unit cell of the macroscopic domain are assumed to be uniform. Thus, this technique in not valid in situations where those macroscopic fields have significant variations, as in the case of cracks, which display high stress concentration factors.

The homogenization theory should be employed to solve linear elasticity problems. Its application on nonlinear elasticity problems may or may not produce accurate results. A prime example of such problem an analysis of a thin-walled cellular material that results in the buckling phenomenon. Regardless of the linearity or nonlinearity of the situation, the displacement of every structure verifies the principle of minimum total potential energy. Homogenization assumes the periodicity of its unit cells macroscopic fields, so the unit cell's displacements are assumed to be periodic. In some instances, the elastic energy of such configuration is vastly superior to a situation where the displacements of the unit cells are not periodic. Therefore, the theory can still see use in nonlinear analysis, provided it is used with caution.

Lastly, in order for the homogenization theory to be valid, there should exist a unit cell with a small characteristic dimension d, far smaller than the characteristic dimension of the macroscopic domain, D. Its ratio is responsible for the rapidly oscillating nature of the elliptic differential equations, and is defined as:

$$\varepsilon = \frac{d}{D} \tag{2.35}$$

In the homogenization of the elasticity problem, the macroscopic dimension is considered to be far larger than the microscopic one, and as such, it assumes that $\varepsilon \to 0$. Such condition fails to be verified in real materials, since both characteristic dimensions are finite values, ε too is a finite value. Yet, in practice, if both scales are a couple of orders of magnitude apart, homogenization is able to produce results that precisely portray reality.

2.4.2 Homogenization of the Elasticity Problem

Assume a generic structure composed by a periodic medium characterized by a small parameter ε is subject to boundary conditions. The resulting stresses and strains vary from point to point in the macroscopic scale $\mathbf{x}$. However, those same fields also vary in a small neighbourhood of point $\mathbf{x}$ if one moves in the microscopic scale, say $\mathbf{x}/\varepsilon$. Therefore, it can be said that those fields depend on two variables, one for each scale, as in the displacement function $\mathbf{u}(\mathbf{x}, \mathbf{x}/\varepsilon)$. Given that the material is periodic on a microscopic scale, said fields too are periodic on the microscopic variable $\mathbf{y} = \mathbf{x}/\varepsilon$. Knowing that the solution of the problem $\mathbf{u}^\varepsilon$ has a dependence on both scales, it can be expressed as an asymptotic expansion with respect to the parameter ε, as in:

$$\mathbf{u}^\varepsilon(\mathbf{x}) = \boldsymbol{u}^0(\mathbf{x}, \boldsymbol{y}) + \varepsilon\mathbf{u}^1(\mathbf{x}, \mathbf{y}) + \varepsilon^2\mathbf{u}^2(\mathbf{x}, \mathbf{y}) + \ldots = \sum_{i=0}^{\infty} \varepsilon^i \mathbf{u}^i(\mathbf{x}, \mathbf{y}), \quad \mathbf{y} = \mathbf{x}/\varepsilon \tag{2.36}$$

As will be seen ahead, the term $\mathbf{u}^0$ only has a dependence on the macroscopic variable $\mathbf{x}$, and it translates the behaviour of the heterogeneous periodic material in the macroscopic scale as if it was an equivalent homogeneous one. It is common to only consider the expansion 2.36 up to the term of first order of ε. That term is responsible for correcting the macroscopic term on a microscopic level, in order for the homogeneities to be considered in the global solution.

The elasticity problem, seen in 2.8, consists of finding the displacement $\mathbf{u}$, solution of the elliptic differential equation that translates the equilibrium of stresses, due to body forces in its domain and applied stress boundary conditions (natural boundary conditions), and verifies the imposed displacements (essential boundary conditions). The equilibrium equations are as follows:

$$\frac{\partial \sigma_{ij}^\varepsilon}{\partial x_i} + f_j = 0 \text{ in } \Omega_\varepsilon \tag{2.37}$$

$$\sigma_{ij} n_j = t_i \text{ in } \Gamma_\mathbf{t} \tag{2.38}$$

$$\mathbf{u}^\varepsilon = \mathbf{u}_i \text{ in } \Gamma_\mathbf{u} \tag{2.39}$$

Although there are several ways to obtain the homogenization theory formulation, the principle of the minimal total potential energy will be used. That way, whichever is the order of magnitude of ε of the asymptotic expansion used, the solution is guaranteed to the the best out of all the kinematically admissible ones, therefore, it is the actual solution of the problem. The total potential energy, Π, of an arbitrary structure associated with a displacement field $\mathbf{v}$ is related to the elastic strain energy U and the potential of the applied forces $\mathcal{P}$ as:

$$\Pi(\mathbf{v}) = U(\mathbf{v}) - \mathcal{P}(\mathbf{v}) = \frac{1}{2}\int_\Omega \sigma_{ij}(\mathbf{v})\varepsilon_{ij}(\mathbf{v})\, dV - \left(\int_\Omega f_i v_i\, dV + \int_{\Gamma_\mathbf{t}} t_i v_i\, dA\right) \tag{2.40}$$

The generic function $\mathbf{v}$ is to be approximated up to the ε term in the asymptotic expansion:

$$\mathbf{v}(\mathbf{x},\mathbf{y}) \simeq \mathbf{v}^0(\mathbf{x}) + \varepsilon \mathbf{v}^1(\mathbf{x},\mathbf{y})\Big|_{\mathbf{y}=\mathbf{x}/\varepsilon} \tag{2.41}$$

Knowing that the actual deformed structure has the minimal total potential energy of all the kinematically admissible deformed states of that same structure, it can be stated that the displacement field $\mathbf{u}^0(\mathbf{x})+\varepsilon\mathbf{u}^1(\mathbf{x},\mathbf{y})$ is the approximate solution of the problem. Thus, if the solution is slightly perturbed in any direction, the total potential energy will surely increase. Then, displacement field $\mathbf{v}$ can defined in terms of the actual solution and an arbitrary $\mathbf{w}$ function:

$$\begin{aligned} \mathbf{v}^0(\mathbf{x}) &= \mathbf{u}^0(\mathbf{x}) + \alpha \mathbf{w}^0(\mathbf{x}) \\ \mathbf{v}^1(\mathbf{x},\mathbf{y}) &= \mathbf{u}^1(\mathbf{x},\mathbf{y}) + \beta \mathbf{w}^1(\mathbf{x},\mathbf{y}) \end{aligned} \tag{2.42}$$

Since $\mathbf{u}$ implies the minimization of the total potential energy, the derivative of the total potential energy (2.43) with regards to the α and β parameters (2.42)is zero when both their values are zero, since it is a stationary point.

$$\begin{aligned} &\frac{\partial}{\partial\alpha}\left[\Pi\Big(\mathbf{u}^0(\mathbf{x}) + \varepsilon\mathbf{u}^1(\mathbf{x},\mathbf{y}) + \alpha\mathbf{w}^0(\mathbf{x}) + \varepsilon\beta\mathbf{w}^1(\mathbf{x},\mathbf{y})\Big)\right]\Bigg|_{\alpha=0,\beta=0} = 0 \\ &\frac{\partial}{\partial\beta}\left[\Pi\Big(\mathbf{u}^0(\mathbf{x}) + \varepsilon\mathbf{u}^1(\mathbf{x},\mathbf{y}) + \alpha\mathbf{w}^0(\mathbf{x}) + \varepsilon\beta\mathbf{w}^1(\mathbf{x},\mathbf{y})\Big)\right]\Bigg|_{\alpha=0,\beta=0} = 0 \\ &\forall \mathbf{w}^0, \mathbf{w}^1 \text{ smooth enough, } \mathbf{w}^0\big|_{\Gamma_u} = 0, \ \mathbf{w}^1 \text{ Y-periodic} \end{aligned} \tag{2.43}$$

Also, the strain and stress functions are linear in terms of $\mathbf{v}$, thus:

$$\begin{aligned} \sigma_{ij}(\mathbf{u}+\alpha\mathbf{w}) &= \sigma_{ij}(\mathbf{u}) + \alpha\sigma_{ij}(\mathbf{w}) \\ \varepsilon_{ij}(\mathbf{u}+\alpha\mathbf{w}) &= \varepsilon_{ij}(\mathbf{u}) + \alpha\varepsilon_{ij}(\mathbf{w}) \end{aligned} \tag{2.44}$$

Taking in consideration equations 2.40, 2.43, 2.44, the symmetries of E_{ijkl} presented in 2.9 and assuming small displacements (equation 2.4), comes:

$$\int_\Omega E_{ijkl}\frac{du_k^0}{dx_l}\frac{dw_i^0}{dx_j}\,dV + \varepsilon\int_\Omega E_{ijkl}\frac{du_k^1}{dx_l}\frac{dw_i^0}{dx_j}\,dV - \int_\Omega f_i w_i^0\,dV - \int_{\Gamma_t} t_i w_i^0\,dA = 0 \tag{2.45}$$

$$\varepsilon\int_\Omega E_{ijkl}\frac{du_k^0}{dx_l}\frac{dw_i^1}{dx_j}\,dV + \varepsilon^2\int_\Omega E_{ijkl}\frac{du_k^1}{dx_l}\frac{dw_i^1}{dx_j}\,dV - \varepsilon\int_\Omega f_i w_i^1\,dV - \varepsilon\int_{\Gamma_t} t_i w_i^1\,dA = 0 \tag{2.46}$$

$$\forall \mathbf{w}^0, \mathbf{w}^1 \text{ smooth enough, } \mathbf{w}^0\big|_{\Gamma_u} = 0, \ \mathbf{w}^1 \text{ Y-periodic}$$

The terms of first order of the asymptotic expansion have both an explicit and implicit dependence on $\mathbf{x}$, as seen using the chain rule:

$$\left.\frac{d\mathbf{w}^1(\mathbf{x},\mathbf{y})}{d\mathbf{x}}\right|_{\mathbf{y}=\mathbf{x}/\varepsilon} = \left.\left(\frac{\partial \mathbf{w}^1(\mathbf{x},\mathbf{y})}{\partial \mathbf{x}} + \frac{1}{\varepsilon}\frac{\partial \mathbf{w}^1(\mathbf{x},\mathbf{y})}{\partial \mathbf{y}}\right)\right|_{\mathbf{y}=\mathbf{x}/\varepsilon} \tag{2.47}$$

Additionally, one property from variational calculus is required. Let $\mathbf{g}$ be an arbitrary function periodic in the variable $\mathbf{y}$. Should the $\mathbf{g}$ be smooth enough, then:

$$\lim_{\varepsilon\to 0}\int_{\Omega^\varepsilon} \mathbf{g}(\mathbf{x},\mathbf{y})\Big|_{\mathbf{y}=\mathbf{x}/\varepsilon} d\Omega = \int_\Omega \frac{1}{|Y|}\int_Y \mathbf{g}(\mathbf{x},\mathbf{y})\, dY\, d\Omega \tag{2.48}$$

In the context of the homogenization theory, equation 2.48 has a physical interpretation. For any macroscopic point $\mathbf{x}$, assuming small values of ε, the value of the limit calculated at a $\mathbf{y}$ coordinate is the same as considering the integral of the average value of the function $\mathbf{g}$ in a small enough neighbourhood of $\mathbf{y}$. Physically, it implies the possibility of not considering the value of the displacement function for every microscopic point in order to characterize the macroscopic behaviour. Instead, the same result is obtained by computing the volumetric average of the displacement function in the domain of a unit cell. This further reinforces the idea that the behaviour of the macroscopic medium is not directly impacted by what happens on a microscopic level.

Introducing the results of equations 2.47 and 2.48 into 2.46, taking the limit $\varepsilon \to 0$, through clever choice of the generic $\mathbf{w}^1$ function and applying the fundamental lemma of variational calculus, the microscopic elasticity problem (local problem) may be formulated, resulting in:

$$\int_Y E_{ijkl}\frac{\partial u_k^1(\mathbf{x},\mathbf{y})}{\partial y_l}\frac{\partial \bar{w}_i^1(\mathbf{y})}{\partial y_j}\, dY = -\frac{\partial u_k^0}{\partial x_l}\int_Y E_{ijmn}\frac{\partial \bar{w}_i^1(\mathbf{y})}{\partial y_j}\, dY \tag{2.49}$$

The microscopic displacement field $\mathbf{u}^1$ may be obtained (up to an additive constant $\hat{\mathbf{u}}(\mathbf{x})$) through the equation 2.50. Even though that constant term may not be calculated, its value is not relevant. The macroscopic problem has no dependence on it, and the microscopic stress field is only dependant on its derivative with regards to $\mathbf{y}$, as presented ahead in 2.56.

$$u_k^1 = \chi_k^{mn}\frac{\partial u_m^0}{\partial x_n} + \hat{\mathbf{u}}^1(\mathbf{x}) \tag{2.50}$$

The function $\boldsymbol{\chi}^{mn}(\mathbf{y})$ is defined as the solution of a modified local elasticity problem:

$$\int_Y E_{ijkl}\frac{\partial \chi_k^{mn}(\mathbf{x},\mathbf{y})}{\partial y_l}\frac{\partial \bar{w}_i^1(\mathbf{y})}{\partial y_j}\, dY = -\int_Y E_{ijmn}\frac{\partial \bar{w}_i^1(\mathbf{y})}{\partial y_j}\, dY \tag{2.51}$$

In other words, the microscopic displacement field $\mathbf{u}^1(\mathbf{x}, \mathbf{y})$ is a linear combination of the characteristic displacements $\boldsymbol{\chi}^{mn}$, weighted by the components of the macroscopic strain $\dfrac{\partial \mathbf{u}_0}{\partial \mathbf{x}}$ in that point, plus an unknown additive constant. In equation 2.50 , $\boldsymbol{\chi}^{mn}$ may be interpreted as the term that relates how each component of the applied macroscopic strain affects the actual displacement field verified on a unit cell. Also, it is clear that the macroscopic strain has no contribution to the microscopic displacement field other that its amplitude, since $\mathbf{u}^1$ is linear with regards to it.

It should be noted that equation 2.51 is in the weak form of the typical finite element method equation. In order to numerically compute the entries of $\boldsymbol{\chi}^{mn}$, the following problem is solved through the finite element method:

$$\int_Y E_{ijkl} \frac{\partial \chi_k^{mn}(\mathbf{x}, \mathbf{y})}{\partial y_l} \frac{\partial \bar{w}_i^1(\mathbf{y})}{\partial y_j} \, dY = - \int_Y E_{ijmn} e_{kl}^{0(mn)} \frac{\partial \bar{w}_i^1(\mathbf{y})}{\partial y_j} \, dY \tag{2.52}$$

$\boldsymbol{\chi}^{mn}$ is necessarily a Y-periodic function, as is $\mathbf{u}^1$, and corresponds to the displacement field for the unit load step $e^{0(mn)}$. The approximated microscopic displacement field is then calculated by adding the macroscopic strain fields weighed by $\boldsymbol{\chi}^{mn}$.

Introducing the same equations and principles to 2.45 as was done to 2.46, and additionally the results 2.51 and 2.50, the macroscopic displacement field may be obtained once the microscopic one is computed, through the equation:

$$\int_\Omega \frac{1}{|Y|} \int_Y E_{ijkl} \left(\delta_{km}\delta_{ln} - \frac{\partial \chi_k^{mn}}{\partial y_l} \right) dY \frac{\partial u_m^0}{\partial x_n} \frac{\partial w_i^0}{\partial x_j} \, dV - \int_\Omega \langle f_i \rangle w_i^0 \, dV - \int_{\Gamma_t} t_i w_i^0 \, d\Gamma = 0 \tag{2.53}$$

Where δ_{ij} is the Kronecker's delta. The macroscopic problem, also known as the global one, can be written function of an homogenized stiffness tensor, as such:

$$\int_\Omega \frac{1}{|Y|} \langle E_{ijkl} \rangle \frac{\partial u_m^0}{\partial x_n} \frac{\partial w_i^0}{\partial x_j} \, dV - \int_\Omega \langle f_i \rangle w_i^0 \, dV - \int_{\Gamma_t} t_i w_i^0 \, d\Gamma = 0 \tag{2.54}$$

The homogenized stiffness tensor $\langle E_{ijkl} \rangle$ is the one associated with an homogeneous material with the same macroscopic behaviour as the original material, an heterogeneous medium characterized by a periodic microstructure, and is obtained by:

$$\langle E_{ijmn} \rangle = \frac{1}{|Y|} \int_Y E_{ijkl} \left(\delta_{km}\delta_{ln} - \frac{\partial \chi_k^{mn}}{\partial y_l} \right) dY \tag{2.55}$$

Once the approximated displacement fields and the homogenized elastic properties are discovered the elasticity problem is solved. Through post-processing of the solution, the stress field may be calculated, by direct substitution on Hooke's Law.

$$\sigma_{ij}^0 = E_{ijkl}\left(\delta_{km}\delta_{ln} - \frac{\partial \chi_k^{mn}}{\partial y_l}\right)\frac{\partial u_m^0}{\partial x_n} \tag{2.56}$$

Equation 2.56 corresponds to an approximation of degree 0 with regards to the order or magnitude of ε. Further terms of ε can be considered. The macroscopic stress the structure is subject to can easily be calculated recalling the property presented in 2.48.

$$\sigma_{ij}^H = \langle \sigma_{ij}^0 \rangle = \langle E_{ijkl} \rangle \frac{\partial u_m^0}{\partial x_n} \tag{2.57}$$

The body forces $\mathbf{f}$ seem to not contribute to the microscopic stress field. Although counter-intuitive, the microscopic scale is so small in comparison with macroscopic one that the effect of the body forces is not felt. Should the asymptotic expansion terms considered be up to ε^2, a body force $\mathbf{f}$ contribution would exist, weighted by ε.

Chapter 3

Structural Optimization

3.1 Relevance of Optimal Design

Generally speaking, structural optimization consists in determining the structure that maximizes or minimizes the desired objective function while respecting the imposed constraints. For the engineers, it is an ongoing challenge to design structures as light and cheap as possible, while never compromising the structural integrity of the system. The design process relies heavily on the intuition, experience and knowledge of the designer. Traditionally, the end goal has always been to obtain a good design, as in a final solution that verifies the imposed constraints while being reasonably cheap and easy to build. This process has always been iterative. In the development of a project, after an initial phase of conceptualization and problem formulation, a few iterations are made, in which the various possible solutions are analysed and improved, until they converge to the best solution. The relation of the various optimization typed with the design stages is demonstrated in figure 3.1. The writing of this chapter is heavily based in [1].

Like the traditional design process, structural optimization too is iterative, though instead of a team of designers, an algorithm is now responsible for changing the design between iterations. The optimum design formulation is mathematically rigorous, by having to explicitly define design variables, an objective function to minimize, and the constraints the project is obliged to verify. This usually comes as an advantage, as it forces the designer to better understand the problem before tackling it.

The designer's sensibility is the main advantage in the conventional design. This is particularly true in the earlier stages of the design, as it can swiftly lead to good projects and allows for easier conceptual changes than an algorithm does. When it gets to the detailed design stage,

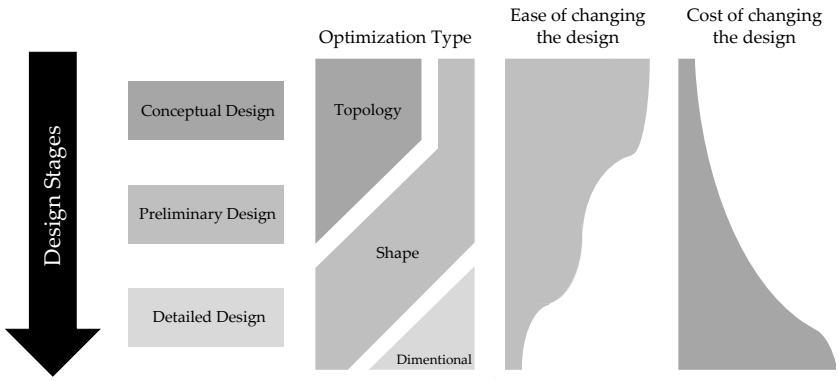

Figure 3.1: Relation between the different optimization types and the design stages - adapted from [16]

optimal design is able to deal with constraints in a way no human can, specially when it comes to complex ones, as multiple load cases or natural frequency limitations. In complex projects this may lead to structurally weak designs, or uneconomical ones. The main limitation of optimal design is its disregard about the feasibility of production of the final solution, although efforts are being made to improve this.

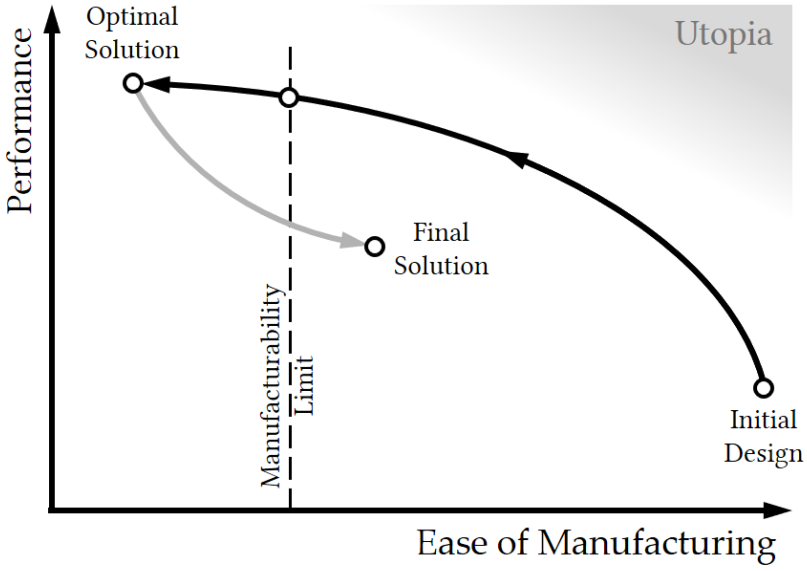

Figure 3.2: Relevance of optimal design in the design of components, and its relation with their ease of manufacturing and performance - adapted from [39]

The implications of the optimal design on a component can be seen in figure 3.2. The final

design is clearly improved when compared to the initial one, at a cost of being much harder to produce. Without any technique to prevent infeasible geometries, the solutions of an optimal design problem are sometimes not manufacturable, meaning it needs to be altered manually. That process brings a huge drop in the performance of a component, while guaranteeing a cost-effective manufacturing process (which is well below the manufacturability limit).

3.1.1 Dimensional Optimization

In a dimensional optimization problem, the design variables are the dimensions that characterize the cross section of the component subject to a load. This is the simplest type of optimization, as the domain's boundary Γ remains unchanged, that is, both the shape and topology of the system are preserved. The most frequent application of this type of optimization is the optimal design of lattice structures, where each design variable corresponds to the area of the cross section of every bar in the structure. The number of bars as well as the position of each node remains constant, as seen in.

The lack of flexibility associated with dimensional optimization means its usefulness is limited to the very last stages of the design process. It is only able to tweak and improve an already existing design, since it cannot bring about any major changes in the structure. In the earlier stages of the design it is preferable to use a formulation with more freedom to make changes, as shape and topology optimization do.

3.1.2 Shape Optimization

In shape optimization, the boundary Γ of the material domain Ω is variable, but the structure's topology is maintained. The boundary is usually defined by lines, which can have an analytical mathematical expression, or be defined by points and interpolation splines. This kind of optimization strives to achieve the optimal shape of the material boundaries. The design variables are the parameters that define the boundary, whether they are the coefficients of the expression that defines the curve or the coordinates of the nodes to be interpolated by a spline.

Since the design's initial topology remains untouched throughout the optimization, there is no guarantee the obtained optimal solution is actually the best, it's only optimal for that particular topology. If the considered topology is sub-optimal, the end result of the optimization is certainly not the best possible one, although optimal for said fixed topology.

Although its flexibility pales in comparison to topology optimization, it allows for very diversified results, as its flexibility is only limited by the parametrization chosen. The reduced flexibility may even be an advantage if the optimal topology is known, or if a specific topology is of particular interest.

One of the main drawbacks of shape optimization is how hard it is to create a finite element analysis robust enough to deal with the possible boundary variations. Should mesh not be adaptive enough, the optimization algorithm will often deform the mesh in a way that favours the objective function. It is desirable that the objective function as independent of the mesh as possible, being influenced only by the design variables that give birth to it.

3.1.3 Topology Optimization

The design of the topology of a structure consists in determining the best possible arrangement of material over a predefined design space. In this type of optimization, the intended final design is usually a black and white representation of a structure, where the black denotes a solid phase and the white is void phase. With the design variables representing the existence, or lack thereof, of material in a discretized point in the design space, the optimization algorithm is free to alter both the shape of the boundaries in the domain and its topology, by being able to create new boundaries and dismiss existing ones.

Topology optimization is a very powerful tool, since it does not favour any solution in detriment of another from the outset (the initial design should be totally neutral). The algorithm is the sole responsible for discovering the optimal design, considering the given objective and constraint functions. Unlike dimensional and shape optimization, the designer does not have control over the topology of the optimal design, which may lead to unexpected solutions to the optimization problem, often better ones than a human can conceptualize. However, the flexibility associated with this method comes with a major drawback, in the form of solutions which are often too complex to cost-effectively produce.

3.2 Standard Formulation

The first step in the standard optimal design process is a deep understanding of the problem that is is going to be solved, to then be able to translate the desired outcome of the optimization into a suitable objective function, along with the constraints inherent to the specific application. Once they are correctly identified, it should be clear what is the type of optimization best suited to tackle the problem efficiently, thus defining the design variables of the problem. The standard formulation of a problem is in the form of equation 3.1.

$$\begin{aligned} \min_{\mathbf{x}} \quad & f(\mathbf{x}) \\ s.t. \quad & \underline{x_i} \leq x_i \leq \overline{x_i}, \qquad i = 1, \ldots, n \\ & g_j(\mathbf{x}) \leq 0, \qquad j = 1, \ldots, m \\ & h_k(\mathbf{x}) = 0, \qquad k = 1, \ldots, p \end{aligned} \tag{3.1}$$

The constraints may be upper and lower bounds on each design variable, denoted as $\underline{x_i}$ and $\overline{x_i}$ respectively, and there are p equality and m inequality constraints, meaning some functions depending on the design variables must respect certain conditions.

Optimal design can be applied to every property of a mechanical system that can be translated into a mathematical formulation. However, the most common applications are related to the minimization of volume, strain energy, or a failure criterion, as the maximum equivalent stress on the material, with whatever the imposed constraints are.

3.3 Minmax Problems

Traditionally, structural optimization has revolved around the problem of minimizing the strain energy with a volume constraint. This problem is well posed, as the objective function is continuous and at least twice differentiable, and there is a mathematical proof of the existence of a single global minimum, as both volume and strain energy functions are convex.

On the other hand, most projects in engineering are not limited by their stiffness, since concerning stresses arise before any major deformations. In a practical sense, the minimization of the maximum failure criterion, like the equivalent stress, is a very useful problem. The typical problem of minimizing the peak equivalent stress is formulated as in equation 3.2.

$$\begin{aligned} \min_{\mathbf{x}} \quad & \max_{\mathbf{y}} \left[\sigma^{VM}(\mathbf{x}, \mathbf{y})\right] \\ s.t. \quad & \underline{x_j} \leq x_j \leq \overline{x_j}, \qquad j = 1, \ldots, n \end{aligned} \tag{3.2}$$

However, the minimum of the maximum of a set of functions is not differentiable. To further aggravate the problem, the local or global minima in the design space usually corresponds to points with discontinuous gradient, as shown graphically in figure 3.3.

To circumvent this issue, strategies were developed to transform the maximum of a set of functions into an equivalent differentiable problem. The idea may be to come up with a function whose value mostly depends on maximum term of the set, as in one of the earlier and most popular approaches, the P-norm function. For P values high enough, the value of the function converges to the maximum stress value in the set [9]. This function is mainly used because of

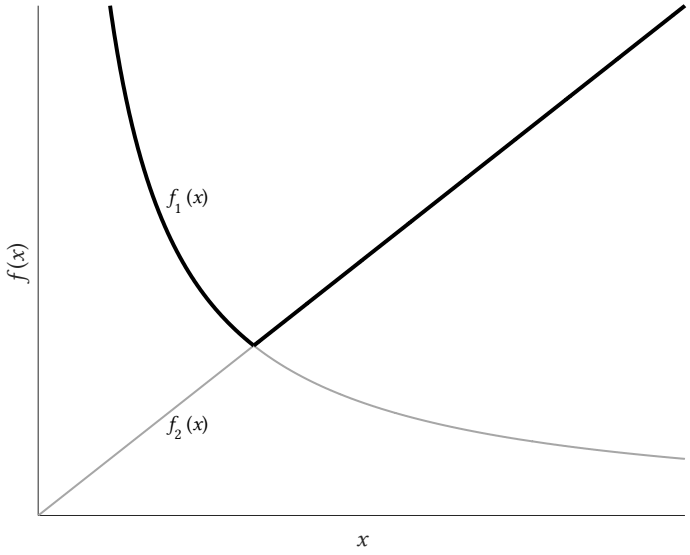

Figure 3.3: Non-differentiability of the minmax problem

its simplicity, and the fact that its intermediate calculations do not result in numbers as big as other methods, meaning there is less numerical error.

$$\max\left[\boldsymbol{\sigma}^{VM}(\mathbf{x})\right] \approx \left[\sum_{i=1}^{n}\left[\sigma_i^{VM}(\mathbf{x})\right]^P\right]^{\frac{1}{P}} \tag{3.3}$$

Another function that accomplishes that is the one in equation, known as the Kreisselmeier-Steinhauser (KS) function [10, 33]. This function makes use of an exponential depend more heavily on the biggest term of the set, while still being differentiable. While this method does a better job than the P-norm at approximating the maximum value of a given set, it is more prone to accumulation of numerical error, since the intermediate calculations involve rather large numbers.

$$\max\left[\boldsymbol{\sigma}^{VM}(\mathbf{x})\right] \approx \frac{1}{\rho}\ln\left(\sum_{i=1}^{n} e^{\rho\sigma_i^{VM}(\mathbf{x})}\right) \tag{3.4}$$

The final method presented to make the minmax problem differentiable is to formulate an equivalent problem, by minimizing an artificial variable, z. Every value of equivalent stress is then constrained by z, as formulated in equation 3.5. This way, the artificial variable z can be minimized, guaranteeing that every stress value is below z. While the additional constraints demand more computational power than the aforementioned functions, this imposes a local

constraint on every element of the mesh rather than controlling a function that aggregates the contribution of every element.

$$\begin{aligned} \min_{\mathbf{x},z} \quad & z \\ s.t. \quad & \sigma_i^{VM} \leq z, \qquad i = 1, \ldots, n^e \\ & \underline{x_j} \leq x_j \leq \overline{x_j}, \qquad j = 1, \ldots, n^v \end{aligned} \tag{3.5}$$

3.4 Optimality Conditions

A generic multivariable function $f(\mathbf{x})$ can be approximated in the neighbourhood of a point $\mathbf{x}^*$ by means of the multidimensional form of Taylor series. In equation 3.6a, the approximation is a polynomial of second degree, and the rate of change is given by equation 3.6b, where $\mathbf{d} = (\mathbf{x} - \mathbf{x}^*)$ and R is a residual term, corresponding to the error of the approximation of the original function by a second degree polynomial.

$$f(\mathbf{x}) = f(\mathbf{x}^*) + \nabla f(\mathbf{x}^*)^T \mathbf{d} + \frac{1}{2}\mathbf{d}^T \mathbf{H}(\mathbf{x}^*)\mathbf{d} + R \tag{3.6a}$$

$$\Delta f(\mathbf{x}) = \nabla f(\mathbf{x}^*)^T \mathbf{d} + \frac{1}{2}\mathbf{d}^T \mathbf{H}(\mathbf{x}^*)\mathbf{d} + R \tag{3.6b}$$

The Hessian matrix $\mathbf{H}(\mathbf{x}^*)$ is the derivative of the gradient of the function with regards to the design variables, assuming the function is at least twice differentiable.

$$H(\mathbf{x}) = \frac{\partial^2 f}{\partial \mathbf{x} \partial \mathbf{x}} = \begin{bmatrix} \frac{\partial^2 f}{\partial x_1^2} & \frac{\partial^2 f}{\partial x_1 \partial x_2} & \cdots & \frac{\partial^2 f}{\partial x_1 \partial x_n} \\ \frac{\partial^2 f}{\partial x_2 \partial x_1} & \frac{\partial^2 f}{\partial x_2 \partial x_2} & \cdots & \frac{\partial^2 f}{\partial x_2 \partial x_n} \\ \vdots & \vdots & & \vdots \\ \frac{\partial^2 f}{\partial x_n \partial x_1} & \frac{\partial^2 f}{\partial x_n \partial x_2} & \cdots & \frac{\partial^2 f}{\partial x_n^2} \end{bmatrix} \tag{3.7}$$

3.4.1 Unconstrained Optimization

Assuming $\mathbf{x}^*$ is a local minimum of the function $f(\mathbf{x})$ implies $\Delta f(\mathbf{x}^*) \geq 0$, whichever is the variation $\mathbf{d}$, given it is small enough. Considering only the first order terms, this condition may only be verified if an infinitesimal perturbation in any direction of the design space results in no change in the function in study, that is, the gradient of said function must be zero in the point $\mathbf{x}^*$.

$$\nabla f(\mathbf{x}^*) \equiv \frac{\partial f(\mathbf{x}^*)}{\partial x_i} = 0, \qquad i = 1, \ldots, n^v \tag{3.8}$$

Points in the design space that respect the condition expressed in equation 3.8 are referred as stationary points. Furthermore, now considering the second order term of the Taylor series, $\Delta f(\mathbf{x}^*)$ is guaranteed to be positive if $\mathbf{d}^T\mathbf{H}\mathbf{d} > 0$. This will be true if the Hessian is positive definite, i.e. its eigenvalues are strictly positive. If the matrix's eigenvalues are only non-negative, it classifies as a positive indefinite one, and $\mathbf{x}^*$ may or may not be a local minimum.

3.4.2 Constrained Optimization

Most structural optimization problems have constraints associated with them, whether they impose equality or inequality. By means of the Lagrange multiplier theorem, the constraints may be moved into the objective function, and it becomes an unconstrained problem. The theorem may only be employed for equality constraints, therefore it is introduced an additional variable per inequality constraint, and the original problem seen in equation 3.1 should now be in the form of equation 3.9.

$$\begin{aligned} \min_{\mathbf{x}} \quad & f(\mathbf{x}) \\ s.t. \quad & g_j(\mathbf{x}) + s_j^2 = 0, \qquad j = 1, \dots, m \\ & h_k(\mathbf{x}) = 0, \qquad k = 1, \dots, p \end{aligned} \tag{3.9}$$

The value of the slack variable s_j must be positive for an admissible design. If an arbitrary point outside the feasible domain is evaluated, the slack variables associated with the violated constraints will be imaginary. By application of the Lagrange multiplier theorem, the Lagrangian function, $\mathcal{L}$, can now be constructed as shown in equation, where v_i and u_j are the Lagrange multipliers associated with the equality and inequality constraints respectively.

$$\mathcal{L}(\mathbf{x}, \mathbf{u}, \mathbf{v}, \mathbf{s}) = f(\mathbf{x}) + \sum_{i=1}^{p} v_i h_i(\mathbf{x}) + \sum_{j=1}^{m} u_j \left(g_j(\mathbf{x}) + s_j^2\right) \tag{3.10}$$

The minimum of the function $f(\mathbf{x})$ with the imposed constraints corresponds to the minimum of the Lagrangian function.

3.5 Optimization Algorithms

The optimization algorithm is responsible for finding the set of design variables that leads to the minimization of a given functional. Optimization algorithms ate mainly divided in two groups: gradient-based ones, and heuristics. Gradient-based algorithms use the derivative of the objective and constraint functions with regards to the design variables to iteratively improve the design, leading to the final, optimal one. A starting point in the design space is given,

and is progressively updated until a convergence criterion is attained, whether the optimality conditions are verified, or a maximum number of iterations is reached. These algorithms are highlighted for being time-efficient, since a relatively low amount of function evaluations is required. That being said, they can't be directly used to solve discrete or non-differentiable problems, which are some of the most relevant in engineering, and they are prone to getting stuck in local minima. Heuristics are searching techniques that strive to achieve a good solution with a reasonable computational cost. Usually, it is not expected that these methods are able to reach the global minimum of a function, since there is no measure of how close to optimal the current design is. Most of these methods take inspiration from phenomena occurring in nature, like genetic combination of animal behaviour. These algorithms are employed in discrete problems, where a gradient-based approach is not applicable, or multimodal problems, since their randomness means they have a lower chance to get stuck in local minima. However, their elevated computational cost is undesirable and sometimes prohibitive, in problems with an expensive function evaluation procedure.

3.5.1 Sequential Quadratic Programming

The Sequential Quadratic Programming (SQP) algorithm transforms the original optimization problem into a second order approximation, and then solves the formulated quadratic programming (QP) problem. The objective function is approximated by a Taylor series expansion up to the term of second order, in the form of equation 3.6a. The constraint functions are approximated up to the first degree term.

The first derivative of every function with regards to every design variable is supplied to the algorithm. Then, it numerically evaluates the Hessian matrix of the objective function using the BFGS formula, presented in equation 3.11.

$$\begin{aligned} H\big(f(\mathbf{x}_{i+1})\big) &= H\big(f(\mathbf{x}_i)\big) + \frac{q_i q_i^T}{q_i^T s_i} - \frac{H_i q_i q_i^T H_i^T}{s_i^T H_i s_i}, \\ s_i &= \mathbf{x}_{i+1} - \mathbf{x}_i, \qquad q_i = \nabla f(\mathbf{x}_{i+1}) - \nabla f(\mathbf{x}_i) \end{aligned} \tag{3.11}$$

Then the algorithm solves the optimization subproblem by finding the point in the design space that verifies the KKT conditions. A new point is calculated, until a stopping criterion is verified.

3.5.2 Method of Moving Asymptotes

The Method of Moving Asymptotes (MMA) is well suited for large scale topology optimization problems, due to the separability of variables and convexity assumed in the construction of the approximated optimization sub-problem [5, 48]. These characteristics make it proper to use in optimization problems with a very high number of design constraints, as is the particular case of stress constrained optimal designs.

$$F(\mathbf{x}) \approx F(\mathbf{x}^0) + \sum_{i=1}^{n^v} \left(\frac{r_i}{U_i - x_i} + \frac{s_i}{x_i - L_i} \right) \tag{3.12}$$

The parameters r_i and s_i are a function of the sensitivity of the function F with regards to the variable x_i. U_i and L_i give asymptotes for the approximation of the function with regards to the variable x_i. The proximity of these values controls the range for which the approximation of F generates reasonable answers, and their value changes in-between iteration. If two successive iterations lower the value of the objective function, the distance between the asymptotes is reduced. If on the second iteration the objective function value increases, the interval where the function is approximated broadens.

Once the objective function is approximated by a sum of n^v functions, n_v optimization subproblems are solved, each of them being a convex function, depending of only one variable, x_i. Through this method, a new point in the design space is obtained, the x^0 of the next iteration. This goes on until a convergence criterion is verified.

3.6 Design Sensitivity Analysis

Sensitivity analysis in structural optimization deals with the computation of derivatives of functionals (both the objective function and constraints) with regards to the design variables. These functionals are function of the solution of an elasticity problem, which is in turn a function of the design variables in some way.

The simplest technique to determine the derivative of a function with regards to a design variable is the finite difference method. This method consists of computing the approximated partial derivative of an given function by causing a small enough perturbation to a design variable and checking the sensibility of the function to said perturbation. The most frequent finite differentiation method is the first order forward one, expressed in equation 3.13. The backwards finite difference is similar to the forwards, but the design variable perturbation is made in the opposite direction. Both these methods involve evaluating the objective function only one additional time.

$$\frac{\partial f(\mathbf{x})}{\partial x_i} \approx \frac{f(\mathbf{x} + \Delta x_i) - f(\mathbf{x})}{\Delta x_i} \tag{3.13}$$

If there is need for a more precise sensibility calculation, the second order central finite differences method may be employed, shown in equation 3.14. To compute the numerical derivative value, two extra function evaluations must be made.

$$\frac{\partial f(\mathbf{x})}{\partial x_i} \approx \frac{f(\mathbf{x} + \Delta x_i) - f(\mathbf{x} - \Delta x_i)}{2\Delta x_i} \tag{3.14}$$

When the finite differentiation method is employed to evaluate the sensitivities of a function, there are two sources of numerical error: condition and truncation errors [27]. The condition error is the difference between the numerical evaluation of the function and its actual value. While that would not be a problem concerning a function with a known analytical expression, if the function value is obtained through a long numerical process, the round-off error in the computation may of significance. The truncation error comes as a consequence of the neglected terms in the Taylor series expansion of the perturbed function. Using forward finite differentiation, only a first order approximation of the Taylor series is achieved, meaning the truncation error is the one presented in equation 3.15.

$$\varepsilon_T(\Delta x) = \frac{\Delta x}{2} \frac{\partial^2 f}{\partial x^2}(x + \zeta \Delta x), \qquad 0 \leq \zeta \leq 1 \tag{3.15}$$

The main advantage of finite differentiation is the easiness of implementation of the method. No requirement is needed other than additional computation time, in order to evaluate the desired function as many extra times as the number of design variables when considering a first order method, or twice as many for a second order one. That being said, the increased computational cost associated with finite differentiation, while sometimes not prohibitive, is certainly a major drawback in problems with a high number of design variables, such as topology optimization. Additionally, since it only uses a *n*th-degree polynomial to approximate the function in the considered point of the design space, there is numerical error associated with the method.

However, sensitivity information may be obtained through alternative, more efficient methods, namely the direct differentiation method or the adjoint variable method [15]. The former computes the dependency of every performance with regards to one design variable at a time, and through the chain rule of differentiation, the total derivative is obtained. Thus, there are as many problems to solve as design variables in the problem. In the adjoint variable method, the implicit part of the derivative is calculated for one performance at a time, for every design variable at once. This makes it suitable for the design sensitivity analysis of optimization problems with more design variables than constraints, in opposition to the direct differentiation method.

Chapter 4

State of the Art

4.1 Introduction

The optimal design of composite materials is an important problem in fields of study as material science, applied mathematics and structural optimization, with direct applications in engineering, as in the optimal design of lightweight structures. Throughout the years, most investigation efforts sought to optimize the macroscopic elastic constants of composite materials. This is a problem of material distribution on the microstructure scale, which in turn dictates the properties on a macroscopic level.

Along with recent advances in technological processes comes the possibility to cost-effectively produce structures with increasingly higher complexity and detail. From a designer's perspective, the stresses present in a structure are usually the concerning factor, which the original studies in topology optimization did not take into consideration. Nowadays, stress constrained topology optimization is increasing in popularity, and there is a new surge of interest around the addition of manufacturing constraints [8].

In this chapter, an historical overview of the analytical advances revolving optimal microstructures will be made, highlighting the main theoretical results. Then, some relevant numerical studies will be presented, using both shape and topology optimization methodologies.

4.2 Analytical Advances

4.2.1 Bounds on Mechanical Properties of Composite Materials

Optimal composite materials design was initially concerned with the bounds of the elastic constants. The broadest possible bounds of the homogenized bulk and shear moduli, K_0 and μ_0, were obtained by Hill [30], inspired by the Weiner bounds for the magnetic permeability of composites. These do not consider the detailed geometry of the microstructure, only the volume fraction of each material phase, and their respective elastic properties . The Hill Bounds are presented in equation 4.1.

$$\begin{aligned} \langle K^{-1} \rangle^{-1} \leq K_0 \leq \langle K \rangle \\ \langle \mu^{-1} \rangle^{-1} \leq \mu_0 \leq \langle \mu \rangle \end{aligned} \tag{4.1}$$

Hashin and Shtrikman [28] tightened the theoretical bounds for 'well-ordered' materials by using the same variational principles already employed to solve the magnetic permeability problem for a composite with two material phases. 'Well-ordered' materials means the bulk and shear moduli of material 1 are both bigger than those of material 2 (equation 4.2). The Hashin-Shtrikman Bounds (HS Bounds) also correspond to a rectangle in the referential of figure 4.1, and are those of equation 4.3. The parameters m_1 and m_2 correspond to the volume fractions of material phases 1 and 2 respectively.

$$(K_1 - K_2)(\mu_1 - \mu_2) \geq 0 \tag{4.2}$$

$$\begin{aligned} K_{HS}^{l} &= K_2 + m_1 \left(\frac{1}{K_1 - K_2} + \frac{m_2}{K_2 + \mu_2} \right)^{-1} \\ K_{HS}^{u} &= K_1 + m_2 \left(\frac{1}{K_2 - K_1} + \frac{m_1}{K_1 + \mu_1} \right)^{-1} \\ \mu_{HS}^{l} &= \mu_2 + m_1 \left(\frac{1}{\mu_1 - \mu_2} + \frac{m_2(K_2 + 2\mu_2)}{2\mu_2(K_2 + \mu_2)} \right)^{-1} \\ \mu_{HS}^{u} &= \mu_1 + m_2 \left(\frac{1}{\mu_2 - \mu_1} + \frac{m_1(K_1 + 2\mu_1)}{2\mu_1(K_1 + \mu_1)} \right)^{-1} \end{aligned} \tag{4.3}$$

Walpole obtained bounds for the case of "badly-ordered"initial materials. Most combinations of real materials in engineering correspond to the well-ordered case. When considering well-ordered base materials, the Walpole Bounds correspond to a rectangle inscribed in the HS rectangle. They have no significant meaning, but are related to the Cherkaev-Gibiansky Bounds discussed ahead.

Cherkaev and Gibiansky [13], in 1993, applied the translation method to obtain a new couple of bounds. While the bound of the bulk modulus remains the same, the limit for the attainable shear modulus has changed. Through the use of the translation method in the Y-Transform domain, new bounds for isotropic materials are discovered.

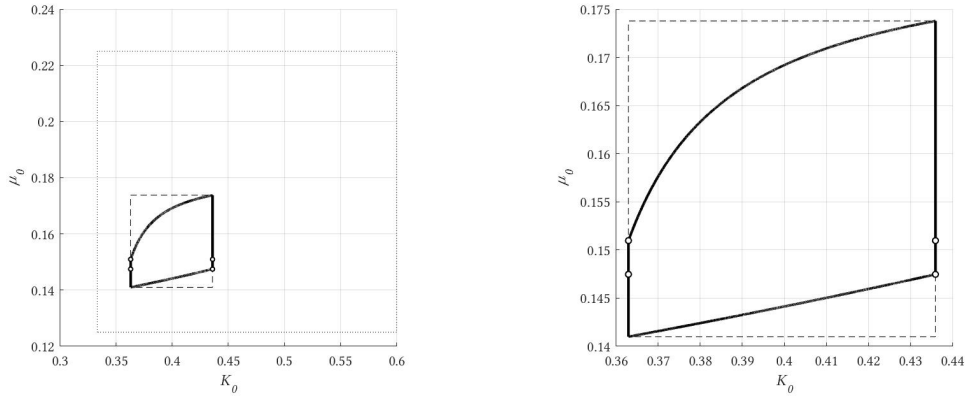

a. With the Hill bounds representation

b. Detail of the HS and coupled bounds

Figure 4.1: Bounds on the mechanical properties of materials - bulk vs shear moduli ($E_1 = 1$, $E_2 = 0.2$, $\nu_1 = \nu_2 = 1/3$, $m_1 = 0.2$)

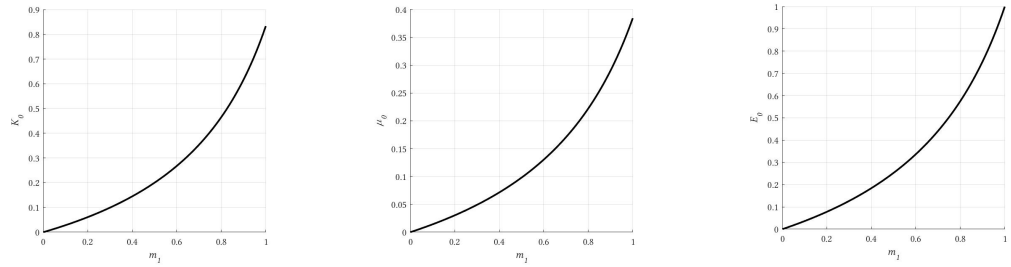

a. Bulk modulus

b. Shear modulus

c. Young modulus

Figure 4.2: Bounds on the mechanical properties of materials as a function of the volume fraction of solid phase

One use of the material bounds presented is to have a rough estimate of the resulting material's properties by knowing the elastic coefficients of its constituents. If the boundaries are tight enough they can accurately predict the resulting properties of the composite material, meaning the proportion of each material phase may be tuned to attain the desired effect. More importantly, these theoretical advances are closely related to the optimal design of composites

with extreme stiffness discussed ahead, and paved the way for material interpolation schemes in density-based topology optimization.

4.2.2 Composite Materials with Extremal Properties

By knowing the theoretical bounds on the effective properties of composite materials, the next step was to identify the microstructures that attain said bounds. The first microstructure to attain the maximum bulk modulus bound was an assemblage of coated spheres (see figure 4.3), discovered by Hashin, in 1962 [29].

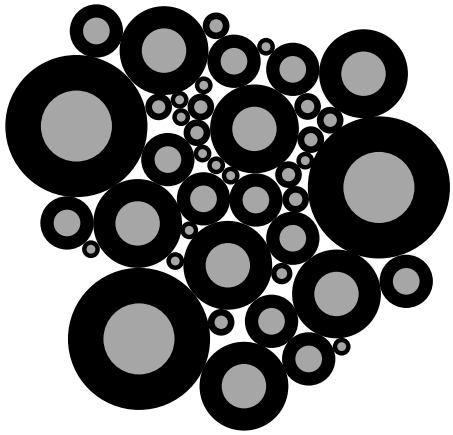

Figure 4.3: Coated Spheres Structure

Later, Francfort and Murat [22] introduced the concept of rank laminates, which are able to attain the bulk modulus's bounds. These microstructures are characterized by having constituents with multiple length-scales (see figure 4.6). Square symmetric two-dimensional rank-2 laminates can attain the extremal bounds on the bulk modulus [46]. They showed that through a rank-3 lamination (see figure 4.7), it is possible to conceptualize a material that attains the maximum bulk and shear moduli simultaneously, corresponding to the upper right corner of figure 4.1b. Although it is known that the whole domain delimited by the theoretical bounds is attainable when considering the conductivity problem (known as G-closure), that is not yet proven for the elasticity problem [35]. Lurie and Cherkaev have conjectured that through the use of n-rank laminates, the whole G-closure is attainable, given any material properties and volume fractions of the constituents. In 1995, Milton and Cherkaev proved the conjecture, for the particular case of two constituents, an infinitely rigid and an infinitely soft one [36].

In 1992, Cherkaev et al. [12] managed to find new invariant properties of stress for the planar elasticity problem. As a direct consequence, came the conclusion that the effective Young's

modulus of a doubly-periodic plate with holes has no dependence on the Poisson's ratio of the base material.

In 2000, Sigmund [46] introduced new composite materials that are able to attain the upper HS bound for the bulk modulus[1], in both two and three dimensions. Along with achieving the upper bound on the bulk modulus, these materials also have a very low shear modulus, almost reaching its lower bound with an hexagonal unit cell (see figure 4.4).

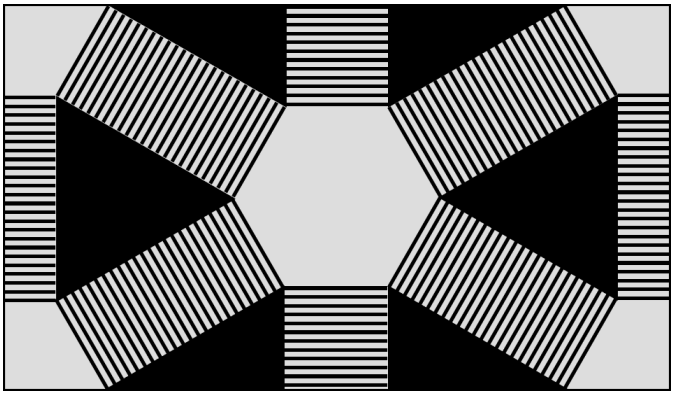

Figure 4.4: Rank-2 microstructure with an hexagonal unit cell

4.2.3 Microstructures Minimizing Peak Equivalent Stress

Prager [41], in 1968, proved the necessary condition of optimality for the minimization of the strain energy with a volume fraction constraint when subject to an arbitrary load. It states that the stress in the free boundaries of the system must be constant. In the particular case of a unit cell in a microstructure, the Equi-Stress condition may be stated as in equation 4.4. Furthermore, he proposed a sufficient condition of optimality, imposing that the strain energy on the unknown boundary is the minimal in the whole material domain.

$$\sigma_{\theta\theta}\big|_{\partial\Omega} = \text{const} \tag{4.4}$$

Cherepanov in 1974 solved the inverse elasticity problem [11]. By imposing the optimality conditions of a structural optimization problem, he managed to obtain the optimal free boundary of the hole on a plate for any load at infinity where $\sigma_1\sigma_2 > 0$. The optimal shape of the hole depends on the applied load. For macroscopic eigenstresses σ_1, σ_2, the optimal boundary of the hole is an ellipse, with the ratio between the major and minor axes equal to the ratio of applied loads, respecting the condition expressed in equation 4.5.

[1] And consequently the lower bound, by reversing the material phases on the microstructure

$$\left(\frac{x}{a}\right)^2 + \left(\frac{y}{b}\right)^2 = 1, \qquad \frac{a}{b} = \frac{\sigma_1}{\sigma_2} \tag{4.5}$$

Additionally, in 1977, Banichuk [2] proved that in order to minimize the maximum stress in the plane elasticity problem, its maximum value must be located only along the free boundary, and its numerical value is given by the sum of the two macroscopic loads, as stated in equation 4.6.

$$\sigma_{\theta\theta} = \sigma_1 + \sigma_2 \tag{4.6}$$

In 1986, Vigdergauz and Cherkaev [55] characterized the shape of the optimal single hole in a plate subject to a load where $\sigma_1\sigma_2 < 0$, meaning traction along one principal direction, and compression along the other. They noticed that, given the opposite sign of the loads at infinity, the tangential stress along the free boundary of the plate must also change its sign.

$$\text{sign } \sigma_{\theta\theta} \neq \text{constant on } \partial\Omega_{hole} \tag{4.7}$$

$$(\sigma_{\theta\theta})^2 = \text{constant on } \partial\Omega_{hole} \tag{4.8}$$

The Equi-Stress condition around the free boundary was expanded to include the possibility of maximum stresses of equal modulus, but different sign. By acknowledging the stress distribution along a smooth hole is continuous, the condition expressed in 4.7 can only be reached if the free boundary is non-smooth.

In 1995, Grabovsky and Kohn [25], by using the translation method developed by Cherepanov [11], managed to obtain the parametric equation of the doubly periodic holes in a plate that maximize the bulk modulus of the resulting material, while guaranteeing a desired volume fraction. This result was predicted by Vigdergauz in 1994 [51], and corresponds to a material with square symmetry. In 1999, Vigdergauz expanded these results to an isotropic material, using triangular or hexagonal unit cells [52].

4.3 Numerical Advances

In 1984, Braibant and Fleury [6, 20] tried to minimize the mass of a finite plate subject to a maximum admissible equivalent stress. To attain it, they used spline functions to describe the shape of the hole, using the coordinates of the seven nodes that define a quarter of the hole as design variables (the nodes have variable radius and a fixed angle, when considering polar coordinates). Even though the finite element mesh is quite coarse (see figure 4.5), the employed

method was able to achieve an optimal shape corresponding to a smooth curve resembling an ellipse.

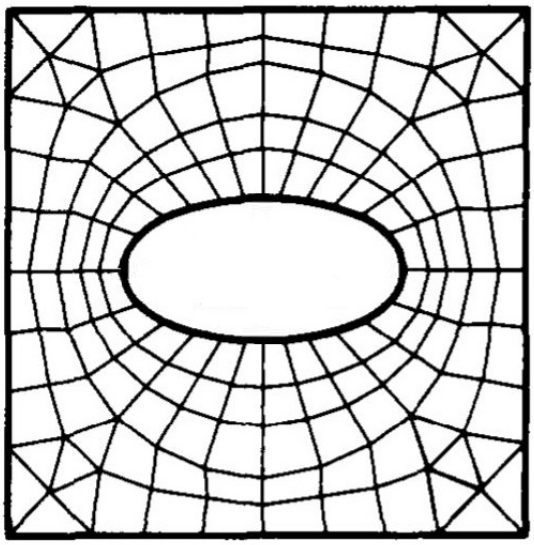

Figure 4.5: Finite element mesh of a finite plate with a hole - extracted from [20]

Though it is known analytically what is the best shape of a hole when the applied stress field has two positive eigenvalues (an ellipse), there isn't such a theoretical result when the eigenstress's sign differ. In 1986, Vigdergauz and Cherkaev [53] discussed some features of the optimal shape a single hole in an infinite plate subject to pure shear, when considering the minimization of the strain energy. Furthermore, they made a numerical experiment in an attempt to discover its optimal shape. In order to solve the physical problem, the complex potentials technique was used. The procedure consisted in optimizing the coefficients of the Laurent series that maps the optimal hole into a circular hole of radius 1. In 1998, the same problem was approached by Cherkaev [14]. Once again, the design variables of the problem were the coefficients of the conformal mapping function $\omega(\xi)$. The authors acknowledge that a single hole does not lead to the minimal possible strain energy on the plate, which may only be attained by a second rank laminate composite [32]. They manage to find a hole with a shape such that the stress is constant along the contour of the hole except on the sharp corners, which is a necessary condition of optimality. However, they could not achieve the sufficient optimality condition, as the maximum strain energy density is not located on a free edge. The discovered optimal shapes are similar to squares with rounded edges, with 102.6° angles at the sharp corners.

Another possible approach is to use coefficients of an analytical expression to define the

actual curvature of the hole. Pedersen [40], in 2000, used this method to find the optimal hole in a finite rectangular plate, using a superelliptic parametrization to define it. This leads to a problem with only one design variable, the exponent η of the superellipse. The problem he actually solved was the min-max of the strain energy density along the contour of the cavity, for a wide range of volume fractions. The obtained results are good, as they have a very close agreement with the Hashin-Shtrikman theoretical bounds.

In 1998, Duysinx and Bendsøe [21] characterized the mechanical behaviour of second rank laminate composites, by studying its mechanical properties and occurring stresses on both scales of the microstructure. The rank 2 laminate is displayed in figure 4.6, with the respective homogenized stiffness tensor being the one of equation 4.9.

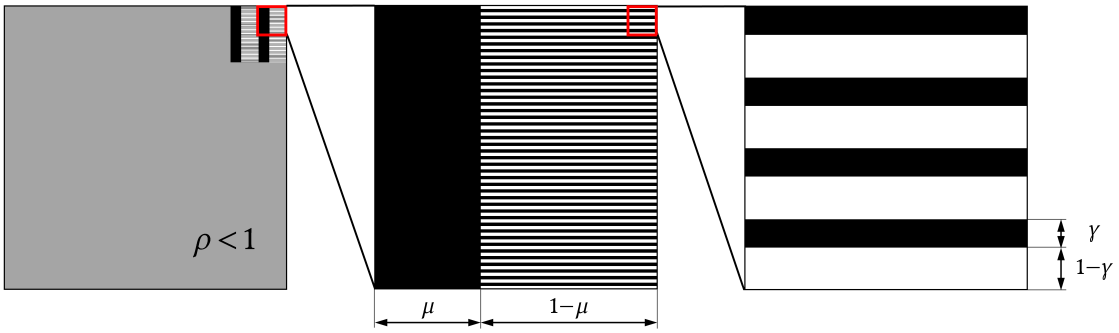

Figure 4.6: Second rank laminate schematic

$$E^H = \frac{E}{(1-\mu)+\mu\gamma(1-\nu^2)} \begin{bmatrix} \gamma & \mu\gamma\nu & 0 \\ \mu\gamma\nu & \mu(1-\mu(1-\gamma)) & 0 \\ 0 & 0 & 0) \end{bmatrix} \tag{4.9}$$

Considering this, they proposed a stress criterion for materials modelled by the SIMP law that contemplates both scales of the material, now giving physical meaning to intermediate density variables in topological optimization. Additionally, numerical examples were presented, including local stress constraints on every element of the finite element mesh. In the following year, Bendsøe and Sigmund [4] compared the SIMP interpolation law with the Young Modulus and Poisson coefficient corresponding to the Hashin-Shtrikman upper bounds for the bulk and shear moduli. They concluded that a SIMP formulation may lead to materials with unattainable characteristics, as they exceed the maximum possible mechanical properties for some values of the penalization exponent p.

In 2002, Lipton [34] introduced a global stress constraint on the problem of maximizing the torsional stiffness of a beam. This was accomplished by introducing an upper bound on the mean square stress on the elements of the cross section. For the roughly same volume

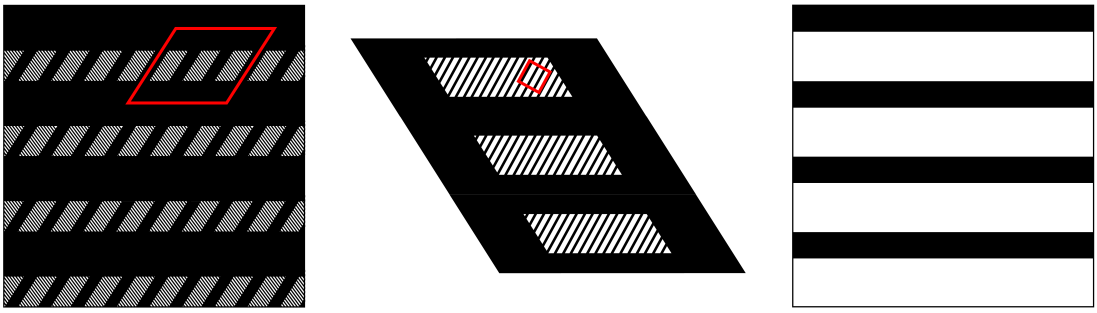

Figure 4.7: Third laminate schematic

fraction, three distinct final designs were obtained, concerning the problems of the minimum of the strain energy, the minimum of the mean square average stress, and the minimum of the strain energy with a mean square stress constraint. The solutions are totally different from one another, reinforcing the importance of including stress constraints in an optimal design formulation.

Nöel [38] in 2017 used a shape optimization approach to the problem of the optimal microstructure, in order to discover the microstructures that lead to the minimum von-Mises equivalent stress for a hydrostatic and shear loads. The level set method was employed, though the level set function used was the analytical expression of the superellipse, instead of the typical Hamilton-Jacobi equation. The elasticity problem was solved using XFEM (expanded finite element method). A comparison was made between the final optimal shapes obtained my minimizing the strain energy and the maximum equivalent stress.

Through a topology optimization framework, Collet [18] in 2018 aimed to find the optimal microstructure for three distinct problems, with and without stress constraints. The numerical examples included the optimal design of the microstructure with the maximum bulk modulus, the synthesis of an auxetic material, and the design of a material for seismic insulation.

In 2018, Coelho [17] applied topology optimization to the design of periodic microstructures with a density-based method. At first, the optimal design for a biaxial load was obtained for the problems of the minimum compliance and minimum compliance with stress constraint. Although the optimal design for both problems should theoretically be exactly the same, that does not happen in practice, by solving the problem numerically. As the compliance is a global measure of performance, it is very insensitive to the geometrical design details of the shape of the cavity, leading to a very uneven stress distribution along the contour of the hole. As for the strength-based design, the local nature of the stress constraints prevents the appearance of stress peaks due to the numerical weaknesses of the discretized physical model, meaning it now has a smoother, well-defined hole. The optimal design for the min-max problem corresponds to a fully

stress design in the elements of the free boundary, as is to expect by recalling the theoretical results. Additionally, a large disparity was found concerning the difference of the optimal shapes for the maximum strength design depending on the applied macroscopic boundary conditions being stress or strain. As for the shear load, it became apparent that the optimal designs are not the same for the stiffness and strength problems. The maximal stiffness design leads to a microstructure comprised of a single hole with the shape of a square with rounded edges. As compliance and stress constraints are imposed, the appearance of a laminate-like structure is favoured.

4.4 Functionally Graded Materials

Recently, some interest has developed on the subject of functionally graded materials. Functionally graded materials (FGMs) are composites in which the material properties vary continuously as a known function. This feature makes them useful in reducing the stress concentration occurring due to a geometric perturbation on the material such as a hole, by choosing a suitable variation of the material properties on the plate [56, 57]. Studies regarding this class of composite materials mainly use an analytical approach to solve the elasticity problem, through the complex variable method.

In 2011, Mohammadi [37] studied the stress concentration around a circular hole on an infinite plate. The material inhomogeneous, with varying elastic properties along the radius direction following an exponential law. When a hydrostatic load is applied, a closed form expression was derived describing the stress concentration in the plate, which could not be achieved for the pure shear load case.

The idea of an homogeneous ring of a softer material around a hole on an isotropic plate was first explored by Sburlati [45] in 2013. A direct comparison was made between a simple circular hole, a hole with a softer homogeneous ring around it, and a functionally graded ring in the radial direction around the hole, considering only the uniaxial traction load. As is to expect, the introduction of any of the rings contributes to the reduction of the peak stress, with the FGM ring leading to a greater reduction than the homogeneous one. In 2014, these results were expanded to include the hydrostatic and pure shear loads, displaying the potential to improve the design of holes in plates through the use of this class of materials [44].

The influence of a functionally graded layer around an elliptic hole in an infinite plate was investigated, by employing the conformal mapping technique [56]. The relevance of the thickness of the FGM layer and the distribution.

In 2019, Zheng [58] employed the same strategy to the reduction of the stress concentration around a spherical cavity in an infinite isotropic solid due to a uniaxial traction load, by

introducing a thick wall of a softer material around it. Analytical and numerical methods were used, showing that both homogeneous and FGM walls serve the intended purpose, with the latter having a better performance than the former.

Yang [57] studied the two-dimensional problem of a finite FGM plate with a circular hole under arbitrary loads. The theoretical approach consists of approximating the continuous mechanical properties variation as a discrete one, comprised of a large number N of concentric homogeneous rings with varying properties. Several exponential laws were considered to define the radial functional gradient. Moreover, the effects of the size of the plate and the positioning of the hole were also analysed.

Chapter 5

Implementation

5.1 Introduction

Depending on the macroscopic boundary conditions, there is a different optimal microstructure that minimizes a given objective function. In the context of the present dissertation, the recurrent goal is to minimize the peak stress in the microstructure, while guaranteeing an imposed amount of void phase in its domain.

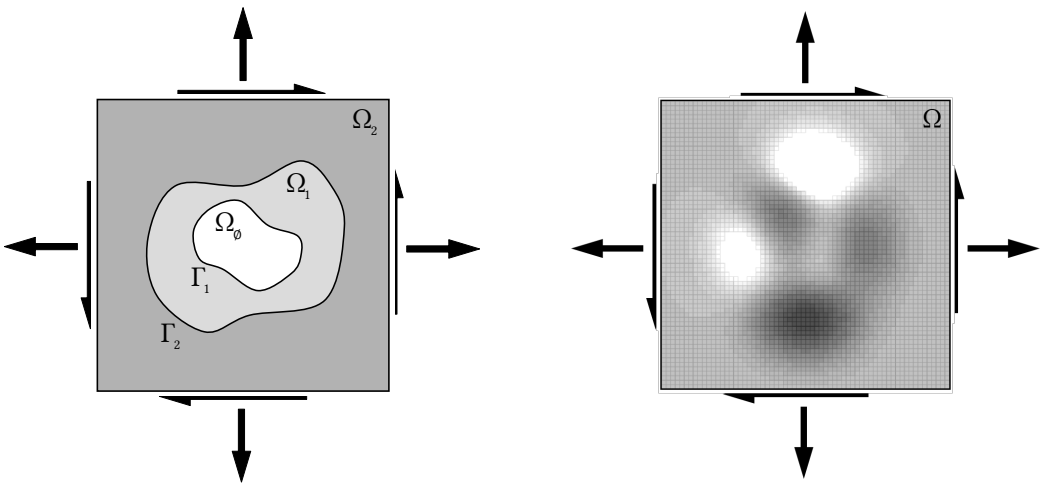

a. Shape optimization problem

b. Variable thickness plate problem

Figure 5.1: Generic optimization problems on a microstructure

With the proposed problem in mind, several approaches are employed. As discussed beforehand, an increased design freedom should lead to more efficient designs. Having that in mind, a range of increasingly more flexible problems are tackled. Ordering by increasing complexity (and potential for a better final design), the Single Material Shape Optimization (SMSO), Single Material Topology Optimization (SMTO), Multi-material Shape Optimization (MMSO) and a Variable Thickness Plate Approach are employed, as further explained in the current chapter. Figures 5.9a and 5.9b showcase a generic microstructure parametrized for shape and topology optimization.

5.2 Planar Elasticity Problem

Given the elasticity problem is the one of a periodic microstructure subject to a macroscopic load, the homogenization problem is employed to solve it. As presented in section 2.4, the homogenization problem consists in the computation of the characteristic displacement fields on the unit cell, χ_k^{mn}, when subject to three unit load steps, $e^{0(mn)}$, for the two-dimensional case.

$$\int_Y E_{ijkl} \frac{\partial \chi_k^{mn}(\mathbf{y})}{\partial y_l} \frac{\partial \bar{w}_i^1(\mathbf{y})}{\partial y_j} \, dY = -\int_Y E_{ijmn} e_{kl}^{0(mn)} \frac{\partial \bar{w}_i^1(\mathbf{y})}{\partial y_j} \, dY \tag{5.1}$$

Once the three $\frac{\partial \chi^{mn}}{\partial y_l}$ fields are obtained numerically, the homogenized stiffness tensor of the microstructure are calculated by direct application of equation 5.2.

$$\langle E_{ijmn} \rangle = \frac{1}{|Y|} \int_Y E_{ijkl} \left(\delta_{km}\delta_{ln} - \frac{\partial \chi_k^{mn}}{\partial y_l} \right) dY \tag{5.2}$$

The approximated microscopic stress field is proportional to the applied macroscopic strain, as can be seen in equation 5.4. Since the problems approached in this dissertation concern a macroscopic stress field boundary condition, the macroscopic strain is removed from the equation by introducing Hooke's Law. Since only the homogenized stiffness tensor is known at the moment, the compliance tensor must be computed through the relation expressed in equation 5.3.

$$\langle E_{ijmn} \rangle \langle C_{mnkl} \rangle = \frac{1}{2}(\delta_{ik}\delta_{jl} + \delta_{il}\delta_{jk}) \tag{5.3}$$

$$\sigma_{ij}^0 = E_{ijkl} \left(\delta_{km}\delta_{ln} - \frac{\partial \chi_k^{mn}}{\partial y_l} \right) \frac{\partial u_m^0}{\partial x_n}, \qquad \frac{\partial u_m^0}{\partial x_n} = \langle \varepsilon_{mn} \rangle = \langle C_{mnpq} \rangle \langle \sigma_{pq} \rangle \tag{5.4}$$

The finite element problems are solved using bilinear Q4 elements. As such, four integration points in every element are necessary. The von-Mises equivalent stress in an element is

calculated considering the volumetric averages of every component of the stress tensor of every Gauss point, as expressed in equation 5.5.

$$\sigma_e^{VM} = \sqrt{\frac{1}{2}\left[\sigma_{11_e}^2 + \sigma_{22_e}^2 + (\sigma_{11_e} - \sigma_{22_e})^2\right] + 3\sigma_{12_e}^2} \tag{5.5}$$

The computational implementation of this method was provided by Guedes, J. M., and is based on the computer programs PREMAT and POSTMAT [26].

5.3 Shape Optimization

5.3.1 Problem Formulation

The problem at hand is the minimization of the maximum equivalent stress in a microstructure, granting a maximum amount of solid phase, when a macroscopic stress field $\langle \sigma_{ij} \rangle$ is applied. In its continuous form, the problem is mathematically formulated as in equation 5.6, where $\underline{x}_l$ and $\overline{x}_l$ are the lower and upper bounds of the design variables x_l, and n^v denotes the number of design variables of the optimization problem.

$$\begin{aligned}
&\min_{\mathbf{x}} \quad \max_{\mathbf{y}} \quad \boldsymbol{\sigma}^{VM}(\mathbf{x}, \mathbf{y}) \\
&s.t. \quad \int_Y E_{ijkl} \frac{\partial \chi_k^{mn}(\mathbf{y})}{\partial y_l} \frac{\partial w_i^1(\mathbf{y})}{\partial y_j} \, dY = -\int_Y E_{ijmn} \frac{\partial w_i^1(\mathbf{y})}{\partial y_j} \, dY \qquad V \leq V^* \\
&\quad \underline{x}_l \leq x_l \leq \overline{x_l}, \qquad\qquad l = 1, \ldots, n^v \\
&\text{with} \quad V = \frac{\int_\Omega 1_{\Omega^{mat}} d\Omega}{\int_\Omega d\Omega} \\
&\quad 1_{\Omega^{mat}} = \begin{cases} 1, & \mathbf{y} \in \Omega^{mat} \\ 0, & \mathbf{y} \in \Omega \backslash \Omega^{mat} \end{cases}
\end{aligned} \tag{5.6}$$

In the continuous problem the void areas have a null Young's modulus, and as such, are not be included in the volume fraction calculation. When transitioning into the discretized version of the optimization problem, the void region of the plate must have a minimal value for the Young's modulus of every element, $E_\varnothing$, or else the global stiffness matrix of the finite element method would be singular. In the discretized formulation presented in equation 5.7, $1_{\Omega^{mat}}$ is now 0 when the element of the mesh has a Young's modulus of the value attributed to the void phase elements.

$$
\begin{aligned}
\min_{\mathbf{x}} \quad & \max_{e} \quad \boldsymbol{\sigma}_e^{VM}(\mathbf{x}), && e = 1, \dots n^e \\
s.t. \quad & \mathbf{K}\boldsymbol{\chi}_k = \mathbf{f}_k^0, && k = 1, 2, 3 \\
& V \leq V^* \\
& \underline{x_l} \leq x_l \leq \overline{x_l}, && l = 1, \dots, n^v \\
\text{with} \quad & V = \frac{\sum_{e=1}^{n^e} 1_{\Omega^{mat}} |Y_e|}{\sum_{e=1}^{n^e} |Y_e|} \\
& 1_{\Omega^{mat}} = \begin{cases} 1, & E_e > E_\varnothing \\ 0, & E_e = E_\varnothing \end{cases}
\end{aligned}
\tag{5.7}
$$

n^e is the number of elements in the finite element mesh, and E_e and $|Y_e|$ denote the Young's modulus and area of the element e respectively. However, the maximum value of a set of functions is not a differentiable function, and thus, a gradient-based algorithm would not be applicable with great success. An equivalent problem is formulated in equation 5.8, as explained in chapter 3.3.

$$
\begin{aligned}
\min_{\mathbf{x},z} \quad & z \\
s.t. \quad & \mathbf{K}\boldsymbol{\chi}_k = \mathbf{f}_k^0, && k = 1, 2, 3 \\
& \boldsymbol{\sigma}_e^{VM}(\mathbf{x}) \leq z, && e = 1, \dots, n^e \\
& V \leq V^* \\
& \underline{x_l} \leq x_l \leq \overline{x_l}, && l = 1, \dots, n^v \\
\text{with} \quad & V = \frac{\sum_{e=1}^{n^e} 1_{\Omega^{mat}} |Y_e|}{\sum_{e=1}^{n^e} |Y_e|} \\
& 1_{\Omega^{mat}} = \begin{cases} 1, & E_e > E_\varnothing \\ 0, & E_e = E_\varnothing \end{cases}
\end{aligned}
\tag{5.8}
$$

5.3.2 Shape Parametrization

As the name suggests, the design variables of a shape optimization problem control the shape of the material boundaries in the plate. In the employed methodology, the shape of the boundaries is defined by analytical expressions, and thus the design variables correspond to the parameters of such equations.

In the present subsection, three different shape parametrizations will be featured, being the superellipse, supershape and k-type Gielis Formula. Their mathematical equations will be presented, and their potential will be unravelled by exploring the influence of each of its parameters.

5.3.2.1 Superellipse

The simplest parametrization used was the superellipse, also known as the Lamé Curve [24]. Its shape is defined by every point that respects the relation expressed in 5.9a. While it is possible to write an explicit function for the curve in a cartesian coordinate system, a polar one is preferred, and the superellipse can be defined as in equation 5.9b.

$$\left|\frac{y_1}{a}\right|^{\eta} + \left|\frac{y_2}{b}\right|^{\eta} = 1 \tag{5.9a}$$

$$r(\theta) = \frac{ab}{\left[\left|a\cos\theta\right|^{\eta} + \left|b\sin\theta\right|^{\eta}\right]^{\frac{1}{\eta}}} \tag{5.9b}$$

The superellipse's curve is defined by three parameters, a, b and η. The constants a and b are positive real numbers, and are related to the length of the major and minor axis of the curve. By analysing equation 5.9b, it is clear to see that a and b correspond to the intersection of the curve with the x and y axis respectively. The parameter η controls the curvature of the function, as represented in figure 5.2. It should be noted that the superellipse is only a smooth curve for $\eta \geq 2$.

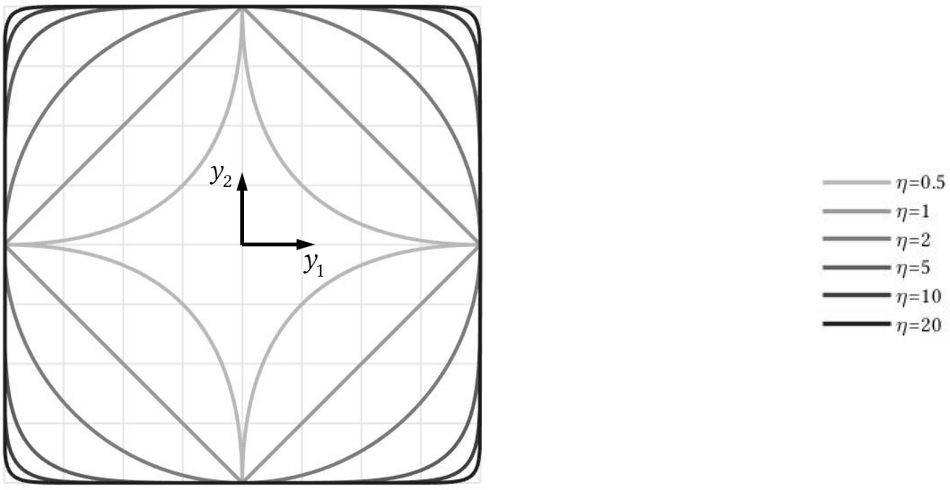

Figure 5.2: Influence of η parameter in the superellipse

5.3.2.2 Supershape

The supershape (equation 5.10) was introduced by J. Gielis [23], and corresponds to an generalization of the regular superellipse. By introducing two additional exponents and a term that allows for more symmetries, the resulting expression can describe a wide array of abstract and naturally occurring shapes.

$$r(\theta) = \left[\left| \frac{1}{a} \cos \frac{m\theta}{4} \right|^{\eta_2} + \left| \frac{1}{b} \sin \frac{m\theta}{4} \right|^{\eta_3} \right]^{-\frac{1}{\eta_1}} \tag{5.10}$$

The m parameter has the effect of changing the number of rotational symmetries. When $\eta_2 = \eta_3$ and $a = b$, the shape has m symmetries, as shown in figure 5.3. When any of those conditions fail, the shape has $m/2$ symmetries instead, which is easy to see, considering a regular ellipse with different axis only has two rotational symmetries.

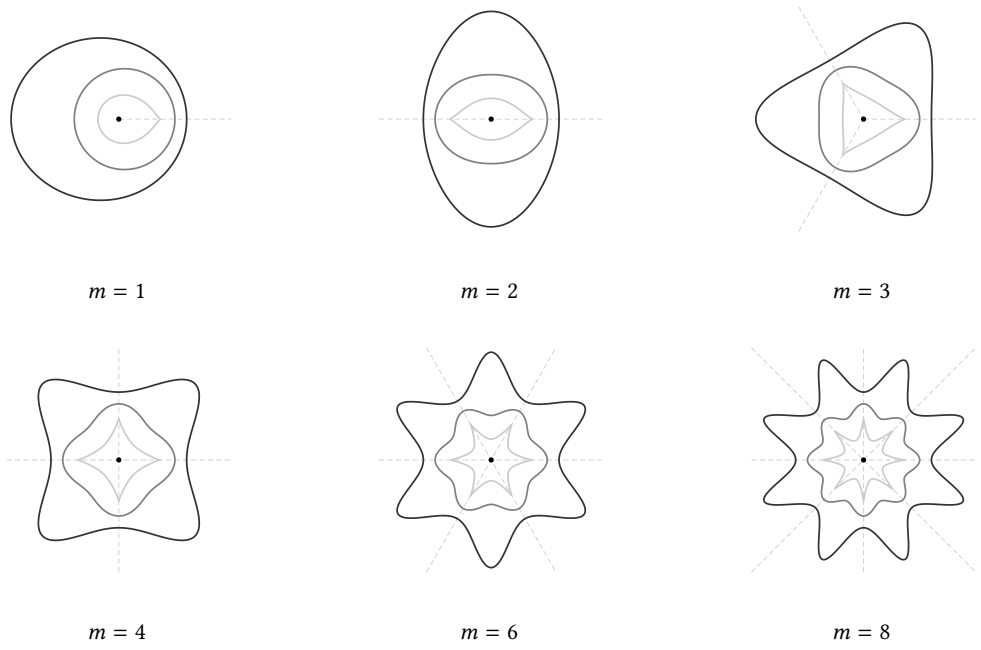

Figure 5.3: Influence of the m parameter of superformula

The influence of the various exponents cannot be easily shown, as is the case of the parameter m. One noteworthy point is that when $\eta_1 = \eta_2 = \eta_3$ and $m = 4$, the obtained shape is a superellipse.

In the context of this dissertation, the purpose of the supershape is to describe the shape of boundaries between different material phases. Even though very complex curves can be obtained by this analytical expression, most make no sense for this specific application. Thus, when the flexibility of one supershape is deemed not enough, the k-type Gielis Formula [23] may be employed. Its expression results of the sum of k supershapes, as presented in equation 5.11, and should result in an increasingly higher flexibility for higher values of k.

$$r(\theta) = \sum_{i=1}^{k} \left[\left| \frac{1}{a_i} \cos \frac{m_i \theta}{4} \right|^{\eta_{2_i}} + \left| \frac{1}{b_i} \sin \frac{m_i \theta}{4} \right|^{\eta_{3_i}} \right]^{-\frac{1}{\eta_{1_i}}} \tag{5.11}$$

5.3.3 Mesh Generation

Along with the problems revolving around the shape parametrization discussed in subsection 5.3.2, one of the main negative aspects of shape optimization is the difficulty associated with the mesh generation. It is desirable that the objective function and constraints depend solely on the design variables, regardless of the finite element mesh. Ideally, the solution of a

finite element method analysis should be insensitive to the discretization of the domain, though in practice this is not the case, as such would require a very fine discretization.

It should be noted that the optimization algorithm treats the homogenization process as a regular function. Should the mesh generation process not be sturdy enough, the optimization algorithm will lead to a situation where the minimization of the function is achieved at the expense of exploiting numerical errors associated with the finite element method, most notably the distortion of the finite element mesh. Considering the large number of function evaluations expected to be made in a single optimization, it is a necessity for the mesh to be as coarse as possible, in order to accelerate the homogenization process. These two conditions are antagonistic, so a suitable compromise must be reached.

5.3.3.1 Hydrostatic and Biaxial Loads

When the macroscopic load is hydrostatic or biaxial, the boundaries are defined by a curve, whether by a superellipse, a supershape, or the sum of multiple supershapes. As represented in figure 5.4, one quarter of the unit cell is modelled by generating the boundary's shape from 0 to 90°, and then mirroring the resulting geometry about the y_1 and y_2 axes.

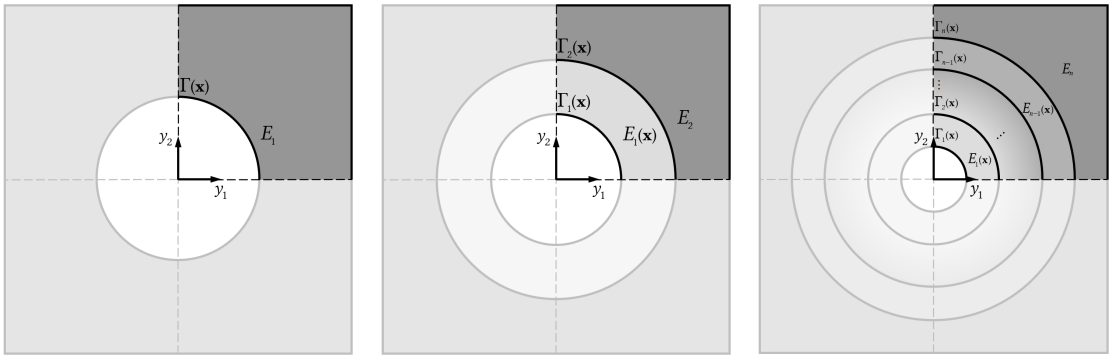

a. One material phase b. Two material phases c. n material phases

Figure 5.4: Unit cell geometry for the hydrostatic and biaxial loads

The design variables of the optimal design problem are responsible for defining the shape of the n boundaries, as well as the $n-1$ Young's moduli of the materials surrounding each boundary. The value of E_n is fixed, and equal to $1GPa$. The Poisson's ratio is a constant for every material phase, of value $\nu = 0.3$.

In the particular case of the hydrostatic load, there is a simplification to be made. The $_{11}$ and $_{22}$ directions of the macroscopic load are interchangeable, since they have the same value, thus the y_1 and y_2 axes of the unit cell referential too must be interchangeable for the optimal

solution, i.e. it must have cubic symmetry. In practice, this means the number of design variables that define each boundary may be reduced, in order to guarantee said cubic symmetry. In the superellipse there is one redundant variable, as $a = b$. Additionally, with the same reasoning, $\eta_2 = \eta_3$ in the supershape parametrization, meaning the number of design variables is reduced by two in the latter case.

5.3.3.2 Shear Load

As for the macroscopic shear load, only a single material phase variant is considered. Since the known theoretical results point in the direction of a square with slightly rounded edges, the proposed geometry tries to mimic just that. By generating an eighth of a unit cell (as represented in figure 5.5 and mirroring it about $y_1 = y_2$, a sharp corner can be obtained[1].

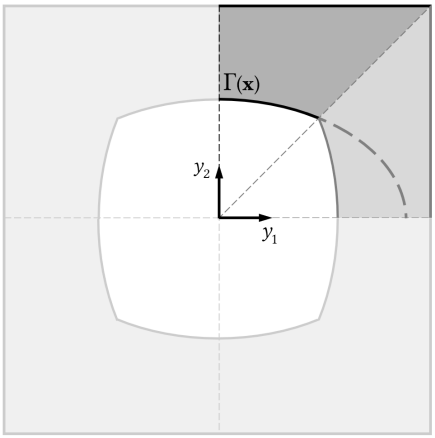

Figure 5.5: Unit cell geometry for the shear load

5.3.3.3 Practical Aspects

To assure the mesh is not overly distorted, a minimum distance δ must be guaranteed between every material boundary (including the last boundary and the edges of the unit cell). In polar coordinates, the aforementioned condition can be stated as in equation 5.12, where n^p is the number of different solid material phases.

$$\begin{aligned} r_{i+1}(\theta) - r_i(\theta) &\geq \delta, \qquad \forall\theta \in [0, \pi/2], \qquad i = 1, \ldots, n^p - 1 \\ r_{cell}(\theta) - r_{n^p}(\theta) &\geq \delta, \qquad \forall\theta \in [0, \pi/2] \end{aligned} \tag{5.12}$$

[1]Should the curve that defines the boundary already be symmetric about $y_1 = y_2$, no sharp corner will be generated

In practice, this condition is verified a finite number of times, as represented in figure 5.6. For this particular application, the function values were evaluated in 91 points, which is more than enough to guarantee the desired condition. The chosen value of δ was always 0.5% of the edge of the unit cell.

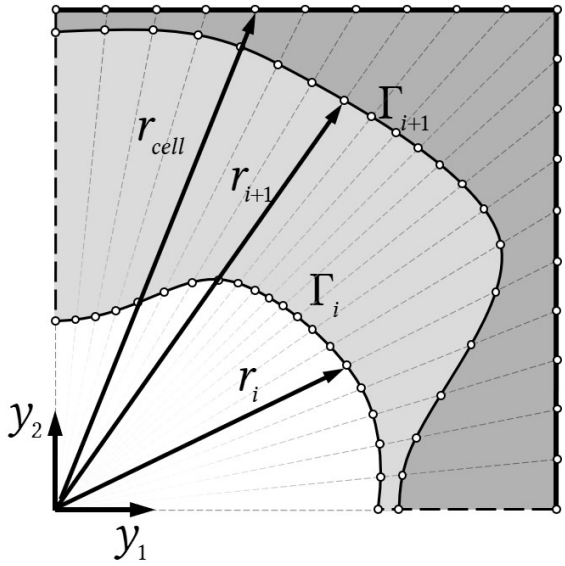

Figure 5.6: Condition of minimum distance between consecutive boundaries

The minimum distance between curves was not implemented as an explicit constraint. Above all, the main advantage is the guarantee that problems when generating the mesh do not occur. When there is an attempt to generate a mesh with two intersecting boundaries, the optimization is interrupted, as the programmed discretization only works fine for the specific topology shown in figure 5.4.

The implemented methodology is represented in the flowchart on figure 5.7. When the input design variables lead to an admissible geometry (meaning they respect the conditions stated in equation 5.12), the mesh is generated, and the homogenization problem is solved. The value of the area is an output of the mesh generation process, and the equivalent stress of the elements is obtained in the postprocessing stage of homogenization. When any of those conditions fail, the mesh generation would fail. Instead, an artificially high value of equivalent stress is attributed to every element, and the maximum possible for the area is assigned. Thus, even when not evaluating the function the typical way, the algorithm associates that point in the design space to an infeasible one. It seems this strategy would cause convergence issues, as a finite difference using such a function evaluation results in a completely wrong derivative value. In practice however, this showed not to be a concern, since the material interfaces alter their shape slowly

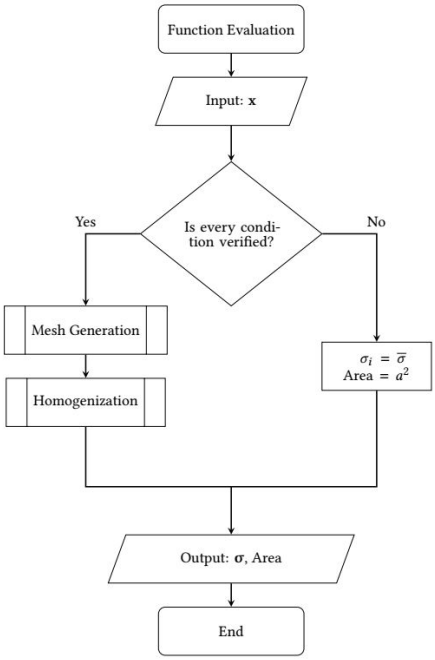

Figure 5.7: Function evaluation with mesh generation conditions

enough through the optimization process, implying that if the shapes are almost touching, it is because the optimization algorithm gradually decided that is the way to go. Thus, this strategy does not have any significance in the optimal design, other that allowing the algorithm not to fail.

Given the high number of function evaluations in an optimization, it is desirable for them to be as expeditious as possible. However, for the solution of a function evaluation to be of any significance, it must have as many elements as possible. Before a compromise is reached, it is ideal to generate a mesh in which its elements are distributed in the most efficient manner possible, in order not to waste computational power.

To allow for a mapped mesh with quadrilateral elements, the domain was divided into quadrilateral areas, as displayed in figure 5.8. The lines in the θ direction have a fixed number of element divisions along its length (as highlighted in figure 5.9a), which is necessary for the mesh to be composed by quadrilateral elements only. The number of divisions of each of these lines is one of the parameters of the mesh generation, which will be henceforth referred to as $n_{div\,\theta}$.

It is to be expected that the interfaces between two different material phases are the zones of the domain with higher stress gradients, thus it would be ideal to have a finer mesh near them. Furthermore, there is a stress discontinuity in the interface between two material phases,

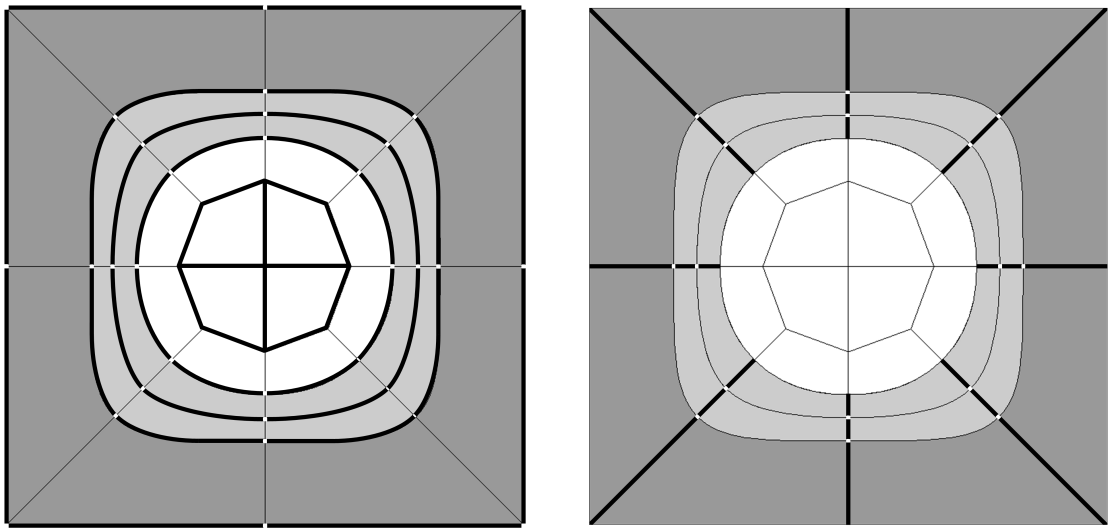

a. Highlighted lines have no spacing ratio and a constant number of element divisions

b. Highlighted lines have spacing ratio and an adaptive number of element divisions

Figure 5.8: Unmeshed unit cell divided into quadrilateral areas

and the peak stress in the microstructure is expected to be there, reinforcing the importance of refining the mesh in these zones. As seen in figure 5.9b, the softer material ring (light grey zone) around the hole is divided in two, an inner and an outer one. This way, the radial lines in the inner ring are given a spacing ratio (ratio between the first and last elements on a line), making possible to have an increasingly finer mesh the closer to the hole. In the outer ring, the same spacing ratio[2] is used, imposing a finer mesh in the vicinity of the material-material interface (see figure 5.9). The outer zone, comprised of the hardest material (dark grey), is given the same spacing ratio, guaranteeing a smooth transition between material phases. The spacing ratio is a parameter of the mesh generation, and affects every radial line in the domain, except the ones in the void phase areas, which will be discussed later on. This procedure is generalized to n soft material phase layers, with each of their domains being divided into two rings, and given spacing ratios, ensuring the refinement of the mesh in the neighbourhood of the interface between different phases.

The number of elements of the radial lines in each ring is proportional to the maximum length of the set of radial lines that exist in a ring, l_{max}:

$$n_{div\,r} = l_{max} \frac{n_{div\,\theta}}{2a} k_{mesh} \tag{5.13}$$

[2]The actual value is the inverse, since the first element of the line is always the one closer to the hole.

The proportionality constant is defined as the product of two terms. The first one is a reasonable value for the number of element divisions per unit of length, defined in terms of $n_{div\,\theta}$ and the length of the edge of the unit cell. The second term is a tuning factor for the number of elements in the mesh, k_{mesh}. Bigger values of k_{mesh} result in a finer mesh in the areas corresponding to a non-void phase.

A generic mesh can be seen in figure 5.9, displaying the importance of the spacing ratio and the control of the number of elements. To prevent the distortion of the mesh, there was a need for an additional parameter, $n_{div\,r_{min}}$. The considered $n_{div\,r}$ is the maximum between the one calculated in 5.13 and the minimum admissible one, as expressed in equation

$$n_{div\,r} = \max\left\{n_{div\,r}, n_{div\,r_{min}}\right\} \tag{5.14}$$

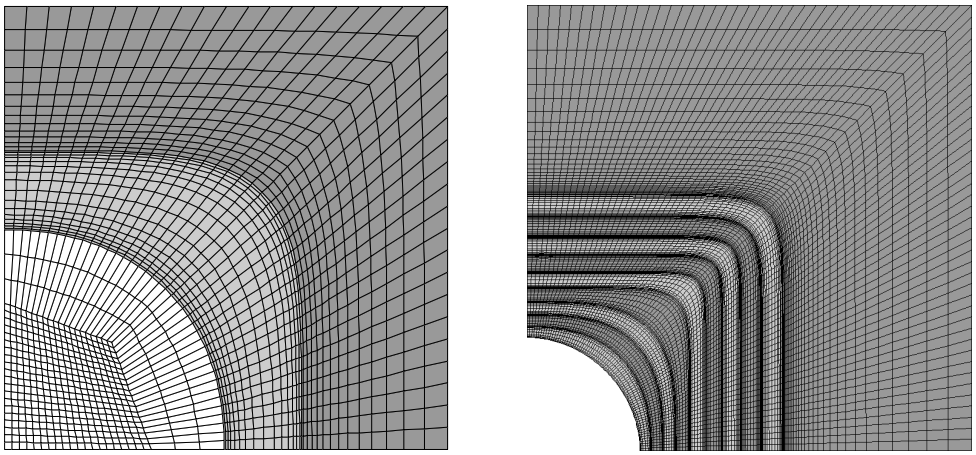

a. $n^p = 2$ b. $n^p = 10$

Figure 5.9: Example of the finite element mesh of a quarter of the unit cell

The Sequential Quadratic Programming function in MATLAB's Optimization Toolbox does not allow for a variable number of constraints. In the case of the single material optimization when subject to a hydrostatic or biaxial macroscopic load this comes as no problem, as one knows from theoretical work that the maximum stress in the material domain is located in the direct neighbourhood of the hole. This means only the stress in the elements adjacent to the hole must be controlled, and that number remains constant. When progressing into the multi-material approaches, or even the single material under a shear load, the location of the peak stress is not straightforward any more, implying that the stress value should be controlled throughout the material domain. Since the mesh is dynamically generated, the number of

elements may change from one function evaluation to the next, resulting in failure of the algorithm due to a change of the number of constraints.

One possible solution would be to use an algorithm that can cope with a variable number of constraints, as the Method of Moving Asymptotes. However this algorithm showed not to be appropriate to use in combination with the supershape parametrization. Variations in the supershape's parameters can have rather unexpected effects on the shape it describes, which are not predicted by the finite differentiation method when computing the sensitivities, leading to the intersecting boundaries problem. When using MMA, this problem can somewhat be controlled by adjusting the algorithm's parameters, drastically reducing the initial distance between asymptotes. While the algorithm is now able do complete an optimization, the obtained solution is severely influenced by the initial design variables chosen, and the method is deemed not capable of dealing with the problem at hand.

The implemented methodology to prevent the failure of the algorithm is to ensure the number of elements remains a constant throughout iterations, in spite of the dynamical generation of the mesh. After the number of element divisions is determined for every set of radial lines but the void phase one, $n_{div\,r_{2np}}$ is calculated, so that the number of total elements matches the desired one, $n_{e\,total}$. The process is summed up in figure 5.10.

This manages the number of void phase elements in order to keep the total number of elements constant. If $n_{e\,total}$ is high enough, every mesh will have the same number of elements, and the optimization runs smoothly. If the design variables result in a mesh with a number of elements equal or greater than $n_{e\,total}$ before considering the void phase ring elements, the final mesh will have an incorrect amount of elements, and the algorithm will fail. Thus, the value of k_{mesh} should be as high as possible, while not violating this conditionç. In figure 5.11 two meshes are presented, each having a different value of k_{mesh}, displaying the ability of the employed methodology to keep the total number of elements unaltered.

It should be noted that not every element must have its equivalent stress value constrained, since the problem has a few symmetries. It is preferable to constrain only a fraction of the elements of the mesh, as long as they are representative of the whole plate, and their number remains unchanged. Taking advantage of the symmetries of the problems, the set of constrained elements for each problem is represented in figure 5.12.

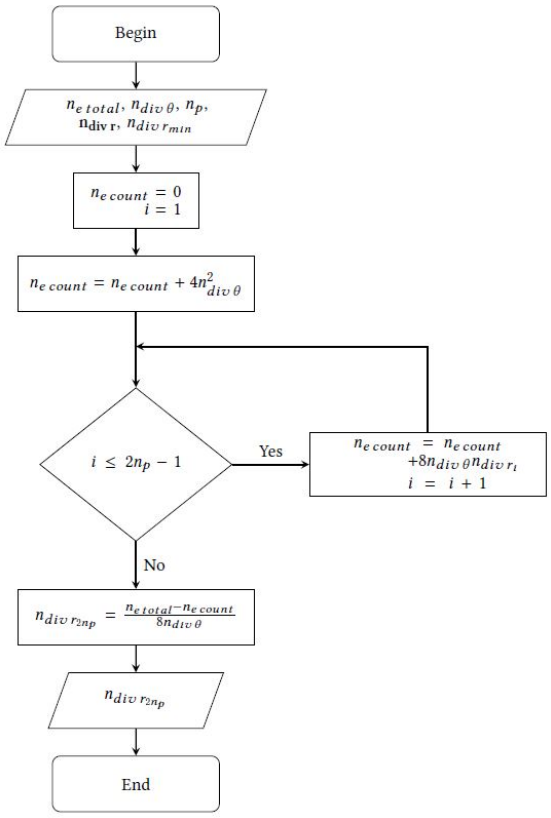

Figure 5.10: Calculation of the number of element divisions of the radial lines of the void phase ring

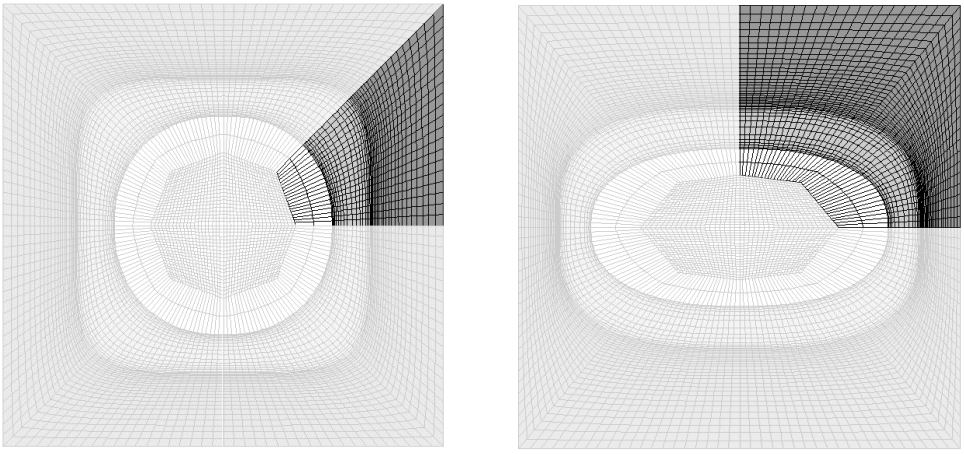

a. Hydrostatic or shear load

b. Biaxial load

Figure 5.12: Elements whose equivalent stress value is constrained

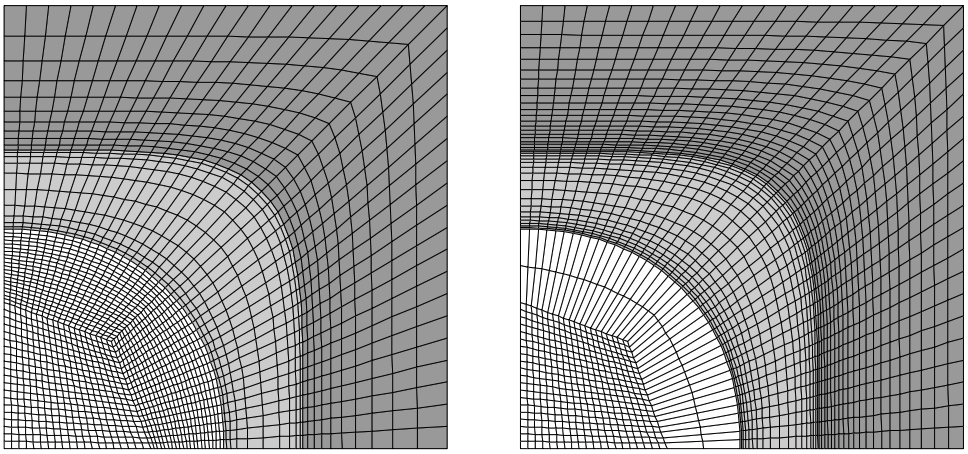

a. $k_{mesh} = 6$ b. $k_{mesh} = 12$

Figure 5.11: Constant element number in the finite element mesh - $n_{e\,total} = 8000$, $n_{div\,\theta} = 20$, $n_{div\,r_{min}} = 5$

5.3.4 Summary

The problems solved through a shape optimization approach are summed up in table 5.1, specifying the combinations of shape parametrizations and macroscopic loads to which they were employed.

Table 5.1: Shape optimization problems summary

Optimization		**Parametrization**		**Macroscopic Load**		
				$\langle\sigma_1\rangle = \langle\sigma_2\rangle$	$\langle\sigma_1\rangle = 2\langle\sigma_2\rangle$	$\langle\sigma_1\rangle = -\langle\sigma_2\rangle$
$\min_{\mathbf{x}}$	$\frac{1}{2}\langle\boldsymbol{\sigma}_{ij}\rangle\langle C_{ijkl}\rangle\langle\boldsymbol{\sigma}_{kl}\rangle$					
$s.t.$	$\mathbf{K}\boldsymbol{\chi}_k = \mathbf{f}_k^0$ $V \leq V^*$ $\underline{x_l} \leq x_l \leq \overline{x_l}$	Single Material	Supershape	———	———	$\mathbf{x} = \{\eta_1, \eta_2, a\}$
$\min_{\mathbf{x},z}$	z	Single Material	Supershape	$\mathbf{x} = \{\eta_1, \eta_2, a\}$	———	$\mathbf{x} = \{\eta_1, \eta_2, a\}$
			k-type Gielis Formula	———	$\mathbf{x} = \{\eta_{1k}, \eta_{2k}, \eta_{3k}, a_k, b_k, E_1\}$	———
$s.t.$	$\mathbf{K}\boldsymbol{\chi}_k = \mathbf{f}_k^0$ $\boldsymbol{\sigma}_e^{VM}(\mathbf{x}) \leq z$ $V \leq V^*$ $\underline{x_l} \leq x_l \leq \overline{x_l}$	Two Material Phases	Superellipse	$\mathbf{x} = \{\eta_i, a_i, E_1\}$	$\mathbf{x} = \{\eta_i, a_i, b_i, E_1\}$	———
			Supershape	$\mathbf{x} = \{\eta_{1i}, \eta_{2i}, a_i, E_1\}$	$\mathbf{x} = \{\eta_{1i}, \eta_{2i}, \eta_{3i}, a_i, b_i, E_1\}$	———
		n Material Phases	Superellipse	$\mathbf{x} = \{\eta_i, E_j\}$	———	———

5.4 Topology Optimization

5.4.1 Variable Thickness Plate Interpretation

With shape optimization, the problem of minimizing the peak equivalent stress in a periodic plate was approached, using increasingly more flexible parametrizations. At first, the single material parametrization is used, attempting to replicate theoretical results. Then, an additional soft material phase layer is added, in an attempt to further reduce the peak stress below the known theoretical value. Lastly, n soft material layers are used, which approaches the behaviour of a functionally graded material. However, using shape optimization, the final solution has necessarily the same topology as the initial design, which limits its potential.

When compared to shape optimization, topology has the potential to find better solutions, given its increased flexibility. The idea is to let every element of the finite element mesh have its own value of Young's modulus, with the optimal design corresponding to the distribution of Young's modulus in the plate that minimizes the peak stress in the plate.

Since the approached problem is two-dimensional, it also has the interpretation of a variable thickness plate composed by an homogeneous material. Recalling equation 5.1, which is used for computing the characteristic displacement fields of the unit cell, it can be said that the stiffness tensor of a point in space can be written as the product of the stiffness tensor in the plate's thickest zone and its relative thickness in the current point.

$$E_{ijkl}(\mathbf{y}) = \frac{h(\mathbf{y})}{h_{max}} E^0_{ijkl} = \rho(\mathbf{y}) E^0_{ijkl} \tag{5.15}$$

In the context of a topology optimization, the term $\frac{h(\mathbf{y})}{h_{max}}$ is substituted by the the density field in the plate, $\rho(\mathbf{y})$, when considering the problem in its continuous form. When it is discretized in a finite element mesh, the Young's modulus in every point is defined as in equation 5.16.

$$E_{ijkl_e} = \frac{h_e}{h_{max}} E^0_{ijkl} = \rho_e E^0_{ijkl} \tag{5.16}$$

This means the optimal solution of the optimization problem may be viewed as either a constant thickness plate with a varying Young's modulus, or a variable thickness plate composed of a single, homogeneous material.

5.4.2 Problem Formulation

The pursued goal is to find the optimal Young's modulus field in the plate (FGM, or variable thickness) for a given macroscopic load that minimizes the peak equivalent stress in the unit cell. Being a functionally graded material, every point in the unit cell that has a non-null

Young's modulus (or thickness) shall be fully considered for the volume calculation. However, experience showed that, in some cases, the simple minimization of the peak stress leads to a disconnex solution, with no actual physical interpretation. This was solved by adding a term dependant of the strain energy density of the plate, weighted by a constant, Ψ. The optimization problem is defined in its continuous form in equation 5.17.

$$
\begin{aligned}
&\min_{E(\mathbf{y})} \quad \max_{\mathbf{y}} \quad \boldsymbol{\sigma}^{VM}\big(\mathbf{y}, E(\mathbf{y})\big) + \Psi C \\
&s.t. \quad \int_Y E_{ijkl} \frac{\partial \chi_k^{mn}(\mathbf{y})}{\partial y_l} \frac{\partial w_i^1(\mathbf{y})}{\partial y_j}\, dY = -\int_Y E_{ijmn} \frac{\partial w_i^1(\mathbf{y})}{\partial y_j}\, dY \qquad V \leq V^* \\
&\quad 0 \leq E(\mathbf{y}) \leq E_{max} \\
&\text{with} \quad C = \frac{1}{2}\langle \sigma_{ij} \rangle \Big\langle C_{ijmn}\big(E(\mathbf{y})\big) \Big\rangle \langle \sigma_{mn} \rangle \\
&\quad V = \frac{\int_\Omega 1_{\Omega^{mat}}\, d\Omega}{\int_\Omega d\Omega} \\
&\quad 1_{\Omega^{mat}} = \begin{cases} 1, & E(\mathbf{y}) > 0 \\ 0, & E(\mathbf{y}) = 0 \end{cases}
\end{aligned}
\tag{5.17}
$$

When considering the passage to the discretized formulation, the plate can no longer have a material with a null Young's modulus (or zero thickness), else the stiffness matrix of the system would be singular, so a minimum value for the Young's modulus must exist. Since the intermediate densities are not penalized through an implicit method (like a SIMP law, for example), a lower bound for the density variable is imposed, with value $\underline{\rho} = 10^{-9}$. Additionally, in order for the optimization to run smoothly, the volume calculation expression must be differentiable, which the $1_{\Omega^{mat}}$ function is not. Then, the volume of every element is weighted by a function of its filtered density value $f(\widetilde{\rho}_e)$. The filtering technique used was a density filter, as thoroughly explained in [7, 47]. The volume calculation function approaches the behaviour of the Heaviside function, while being differentiable, and will be discussed in depth in subsection 5.4.3. Finally, when considering the discretized version of the problem, the maximum von-Mises equivalent stress present in a set of elements itself is a non-differentiable function. Just like in the shape optimization problem, an equivalent problem is formulated by minimizing the artificial variable z instead of σ_e^{VM}, with z constraining the equivalent stress value in every element of the mesh.

$$
\begin{aligned}
\min_{\boldsymbol{\rho},z} \quad & z + \Psi C \\
s.t. \quad & \mathbf{K}\boldsymbol{\chi}_k = \mathbf{f}_k^0, && k = 1,2,3 \\
& \boldsymbol{\sigma}_e^{VM}(\widetilde{\boldsymbol{\rho}}) \leq z, && e = 1,\dots,n^e \\
& V \leq V^* \\
& 0 < \underline{\rho} \leq \rho_e \leq 1 && e = 1,\dots,n^e \\
\text{with} \quad & C = \frac{1}{2}\langle\sigma_{ij}\rangle\langle C_{ijmn}(\widetilde{\boldsymbol{\rho}})\rangle\langle\sigma_{mn}\rangle \\
& V = \frac{\sum_{e=1}^{n^e} f(\widetilde{\rho}_e)|Y_e|}{\sum_{e=1}^{n^e}|Y_e|} \\
& E_e = \widetilde{\rho}_e E_{max}
\end{aligned}
\tag{5.18}
$$

5.4.3 Volume Calculation

In topology optimization, the volume fraction of material is traditionally computed as the average of the density variable in each element weighted by its area throughout the whole domain. In a way, the contribution of density variable in an element to the volume calculation can be thought of as an arbitrary function of the density, and it just so happens to be a linear one, as displayed in figure 5.13.

$$
V(\boldsymbol{\rho}) = \frac{\int_\Omega f(\rho)d\Omega}{\int_\Omega d\Omega} = \frac{\int_\Omega \rho d\Omega}{\int_\Omega d\Omega} \equiv \frac{\sum_{i=1}^{n^e}\rho_i A_i}{\sum_{i=1}^{n^e} A_i} \tag{5.19}
$$

When aiming for a functionally graded cellular material, the objective is to impose a certain fraction of void phase, meaning the remainder corresponds to solid phase, whichever is density value associated, as long as it isn't the lower bound. In other words, the elements with lower bound density values should not be counted as material (as usual), whereas intermediate density values should fully contribute to the volume of the plate, as conceptualized in figure 5.14. Of course such function is not suitable for a gradient-based algorithm since it is discontinuous, thus it serves only to understand the core idea.

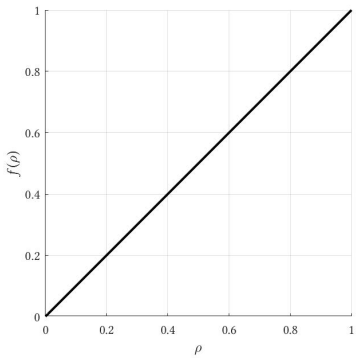

Figure 5.13: Regular volume function

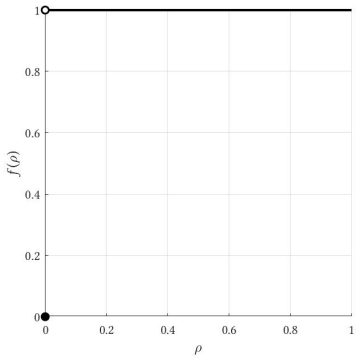

Figure 5.14: Utopic volume function

Then, in order to solve the proposed problem, it is a necessity to find a function with a few desirable properties. Its value at the lower bound of the density variable must be equal to zero, granting it the meaning of a void phase, and the function should have a value of one for density values larger than the lower bound, meaning every density fully contributes to the volume fraction calculation. Additionally, since a gradient-based algorithm is employed to solve the problem, the derivative of the function with regards to the density variable should preferably not be too extreme, as it may lead to numerical issues. The two aforementioned conditions directly conflict with each other, as in order for the function value to go from zero to one as fast as possible, a large gradient value is required. Therefore, a compromise between the two must be reached.

5.4.3.1 Volume Function

In the context of structural optimization, a few penalization functions are already commonly employed, and there has been made attempt to repurpose them. Firstly, the SIMP law is presented. Its mathematical expression and gradient are displayed in equations 5.20a and 5.20b respecively.

$$f(\rho) = (\rho - \underline{\rho})^p \tag{5.20a}$$

$$\frac{\partial f(\rho)}{\partial \rho} = p(\rho - \underline{\rho})^{p-1} \tag{5.20b}$$

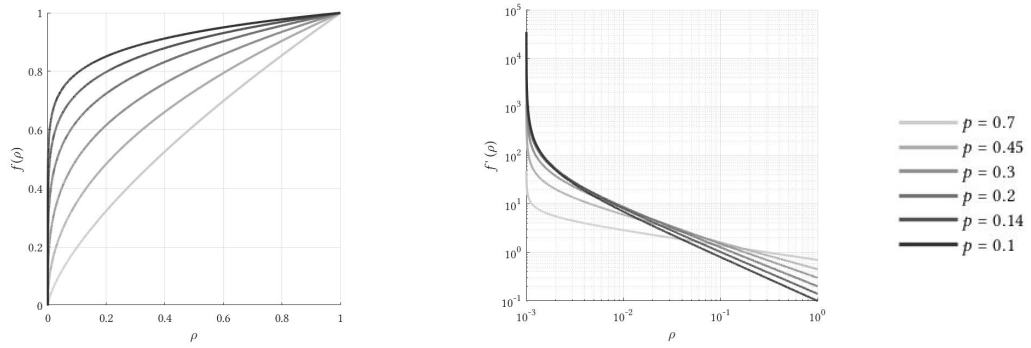

a. SIMP volume function

b. derivative of SIMP volume function (log-log)

Figure 5.15: Volume calculation using the SIMP law

With a penalization exponent approaching zero from the positive side, the function somewhat has the desired curvature, as seen in figure 5.15a. However, the derivative of the SIMP law with regards to the density taken at $\rho = \underline{\rho}$ diverges, making it improper to use. The density variable only goes as low as 10^{-3} in the derivative plot, in order to make it easier to interpret.

Another known interpolation law in the context of structural optimization is the RAMP law, which is enunciated in equation 5.21a. With q approaching -1 from the positive side, a proper curvature is achieved, as seen in figure 5.16a. At first glance, it may seem appropriate, but when plotting the derivative in a log-log scale, it can be seen that the derivative never approaches zero, which means the function is not 1 until $\rho = 1$.

$$f(\rho) = \frac{\rho - \underline{\rho}}{1 + q\big[1 - (\rho - \underline{\rho})\big]} \tag{5.21a}$$

$$\frac{\partial f(\rho)}{\partial \rho} = \frac{q + 1}{\big[q(\rho - \underline{\rho}) - q - 1\big]^2} \tag{5.21b}$$

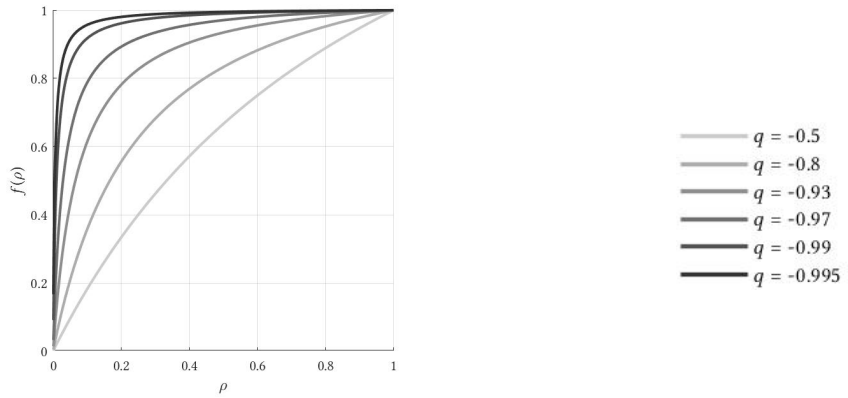

a. RAMP volume function

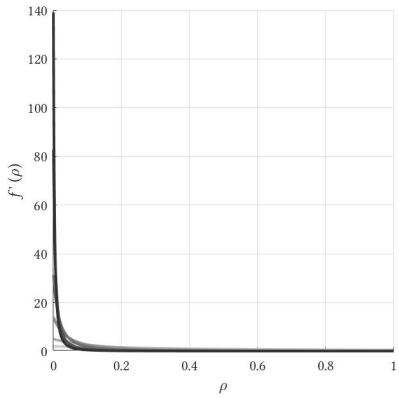

b. derivative of RAMP volume function

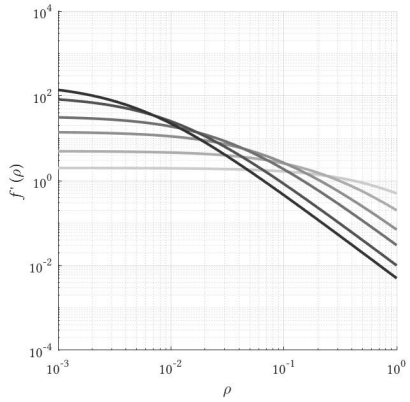

c. derivative of RAMP volume function (log-log)

Figure 5.16: Volume calculation using the RAMP law

Inspired by the differentiability properties of an exponential function, a new penalization law is proposed. Its analytical expression along with the respective derivative are displayed in equations 5.22a and 5.22b.

$$f(\rho) = 1 - \frac{e^{[1-(\rho-\underline{\rho})]^{\beta}} - 1}{e - 1} \tag{5.22a}$$

$$\frac{\partial f(\rho)}{\partial \rho} = \frac{\beta}{e-1}\left[1 - (\rho - \underline{\rho})\right]^{\beta} e^{[1-(\rho-\underline{\rho})]^{\beta}} \tag{5.22b}$$

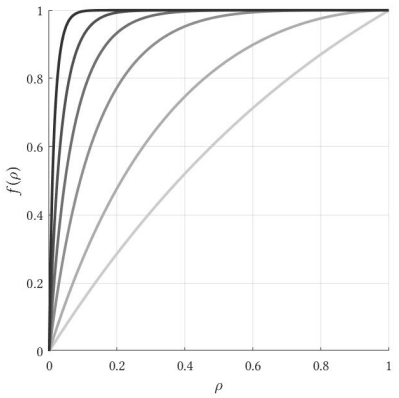

a. EXP volume function

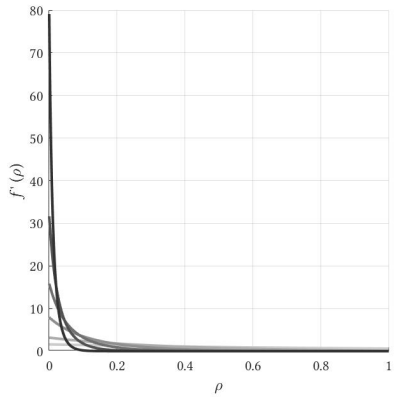

b. derivative of EXP volume function

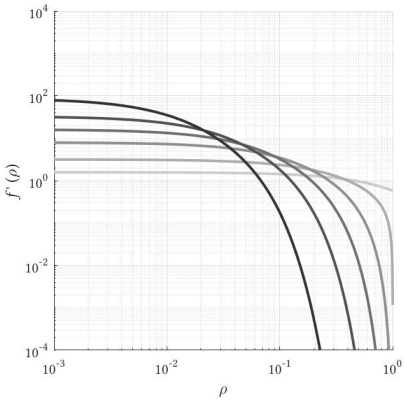

c. derivative of EXP volume function (log-log)

Figure 5.17: Volume calculation using the EXP law

When comparing the RAMP and EXP penalization functions (figures 5.16a and 5.17a) it can be seen that the exponential law has a tendency to converge faster to 1. This idea is further reinforced when comparing the log-log plots of the derivatives, as the EXP law's derivative converges to zero much faster when approaching $\rho = 1$. This law reaches the desired value sooner, with the peak derivative value being significantly lower than the RAMP law, meaning the proposed exponential law is better than RAMP in every way.

5.4.3.2 Additional Considerations

The main downside associated with the introduction of an alternative volume calculation scheme was the lack of ability for the algorithm to transition solid phase zones into void ones, when it so desires.

Due to the derivative of the exponential law with regards to the density variable being almost zero for the intermediate density values, the volume constraint is never violated when the densities vary within this range. However, the gradient of the volume function is extreme when the density value approaches zero. This means that, in order to make the transition from solid to void phase, an abrupt constraint violation would have to occur.

To circumvent this issue, a continuation approach is employed for the volume calculation function. In the first iterations, the β value is low, and increases throughout the optimization, until a maximum value is reached. It was found that a variation given by the function in 5.18a leads to a good end result. Its impact on the volume calculation function can be seen in figure 5.18b. Should the value of β increase faster, the potential of the continuation approach would not be fully exploited. Conversely, if β increased slower, the optimization would allow an artificially high amount of material for too long of a time frame, which heavily favoured disconnex solutions.

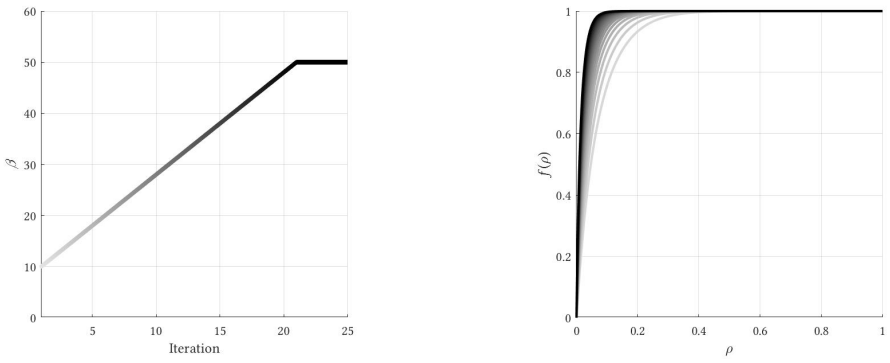

a. Value of β throughout the optimization

b. Variation of the exponential law

Figure 5.18: Continuation approach for the β parameter of the EXP law

5.4.4 Initial Design

5.4.4.1 Introduction

Ideally, the starting point of a topology optimization problem should not favour a certain solution from the outset. However, through solving each optimization several times (varying the initial designs and optimization parameters) for a range of volume fractions, a deeper understanding of the problem at hand is achieved. For each distinct problem, the optimal design is conjectured to have a set of characteristics necessary for its optimality. In order to escape local minima, the initial microstructure design contemplates some of these identified features, resulting in a better final design than using a typical 'fair' starting point in the design

space. This set of characteristics will be discussed ahead, for every problem approached through the variable thickness plate framework.

5.4.4.2 Hydrostatic Load

One feature of any microstructure that is optimal for the hydrostatic load is immediately identified: it must have cubic symmetry (square symmetry in two dimensions). It comes as a consequence that if the macroscopic loads are interchangeable, since they are the same, the axes of the microstructure's referential must too be interchangeable.

Considering a square unit cell is being used, the most immediate choice for an initial design is a solid plate with a circular hole in its center (see figure 5.19), as it resembles the known optimal orthotropic microstructures predicted by Vigdergauz. This was the first topology employed for the unit cell, and led to an improvement over the single material optimal design for every volume fraction.

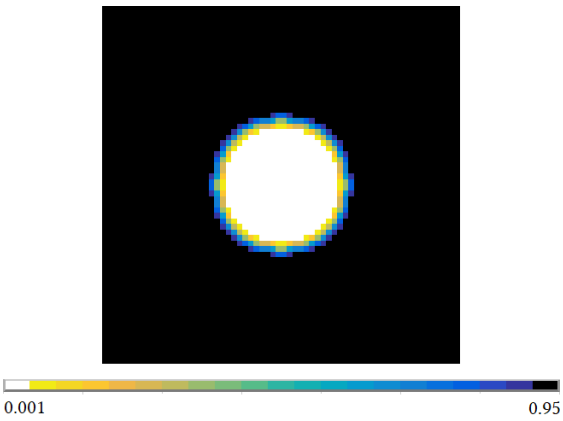

Figure 5.19: Initial density field for the hydrostatic load with 95% volume fraction

However, the introduction of the volume function results in a tremendous lack of ability for the optimization algorithm to open new holes in the plate, since the increase in value of the exponent β is too fast[3]. For volume fractions of 90% and lower this was problematic, as very low density areas were identifiable in the corners of the unit cell, which the algorithm could not fully transition into void. As such, a second type of initial design was used, with a central hole, and quarter circle holes in the corners of the unit cell. Additionally, since intermediate densities always occur in the bisector of the y_1 and y_2 axes, this new initial topology also included this feature, which can be observed in figure 5.20. It is to be noted that the optimization algorithm does not have trouble transitioning a zone from void to solid phase, since that doesn't contribute

[3]Though it is as slow as possible, while not resulting in disconnex final solutions most of the time.

in the way of violating the volume fraction constraint. The reasoning behind this initial design leading to better solutions from a maximum equivalent stress viewpoint will be expanded upon in the results chapter.

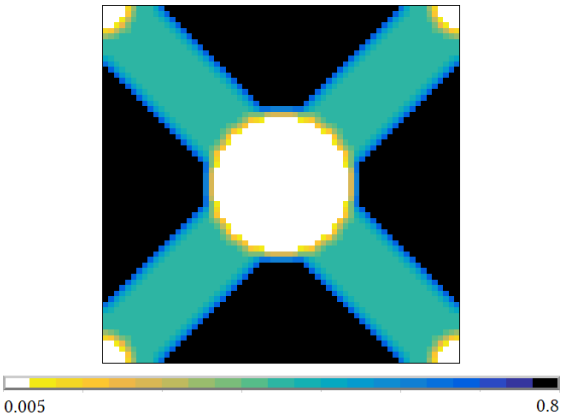

Figure 5.20: Initial density field for the hydrostatic load with 90% volume fraction

5.4.4.3 Biaxial Load

As for the biaxial load, the optimal unit cell is now orthotropic. Considering the known theoretical results, a good starting point for the optimization would be an elliptic hole in the center of a solid plate, analogously to the hydrostatic case. One representative example is presented in figure 5.21.

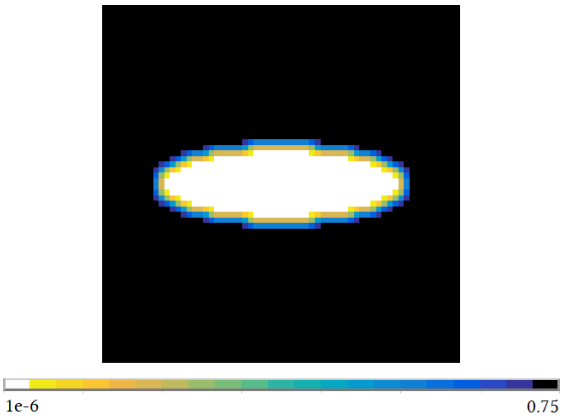

Figure 5.21: Initial density field for the biaxial load with 90% volume fraction

Numerous attempts were made with an initial design with an elliptic hole in the center, and quarter holes in each corner of the plate, as displayed in figure 5.22. However, for every volume fraction, the optimization algorithm tended to get rid of the corner holes, leading to optimal

designs that are either equal to the ones obtained with a simpler starting point, or strictly worse. As such, no solutions are presented for this initial layout in the results chapter.

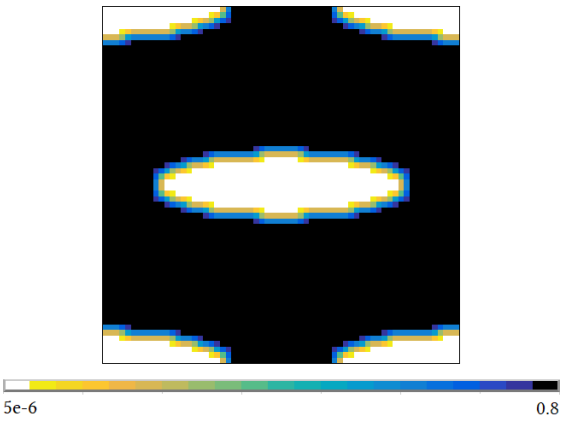

Figure 5.22: Alternative initial density field for the biaxial load with 90% volume fraction

5.4.4.4 Shear Load

When approaching the shear load problem, the initial idea was for the unit cell to be solid with a square hole in the center. It is known that a rounded square hole is the optimal topology for the strain energy minimization, hence it was deemed appropriate as a first guess. As an example, a starting point for the 90% volume fraction is presented in figure 5.23a. Like in the previously discussed case of the hydrostatic load, the optimization algorithm seemed to want to remove one strip of material for every edge of the hole, located at the limits of the unit cell. An attempt to facilitate the optimization process consisted in introducing intermediate densities from the start, as shown in figure 5.23b, with no success.

To address the issue, an initial design that includes slots is used, as represented in figure 5.24a. This improved the final design, leading to a lower peak stress value. However, the same problem occurred, as very low density areas appeared in the zones between the slots and the square hole, for which the initial design displayed in 5.24b was created as a solution. Once again, the final design is more efficient than with the previous initial design, though there is still room for improvement. In the fifth initial design (figure 5.24c), another slot is added, and once again, the design is improved.

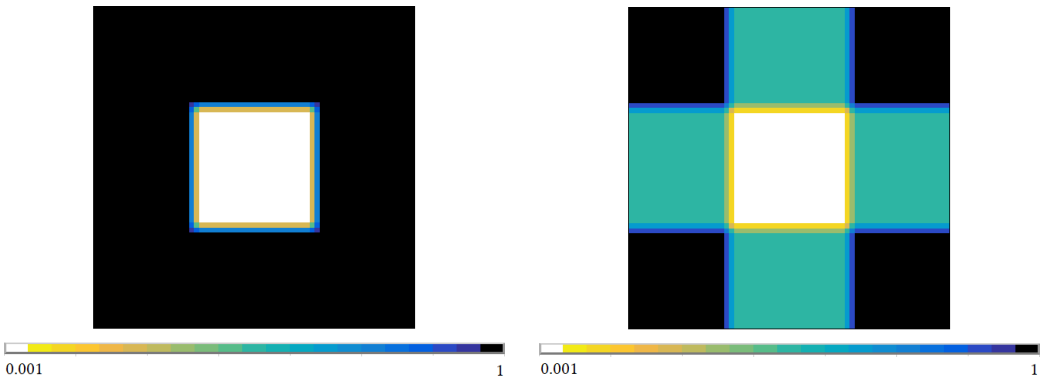

a. Initial design 1

b. Initial design 2

Figure 5.23: Single hole initial designs for the shear load with 90% volume fraction

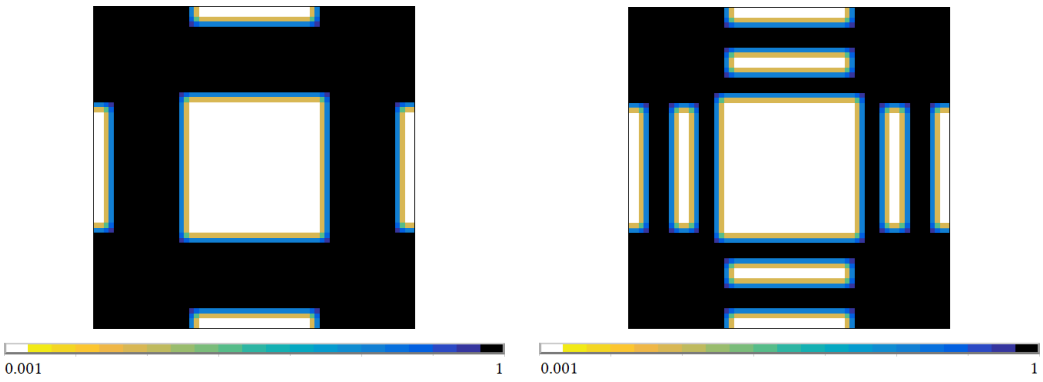

a. Initial design 3

b. Initial design 4

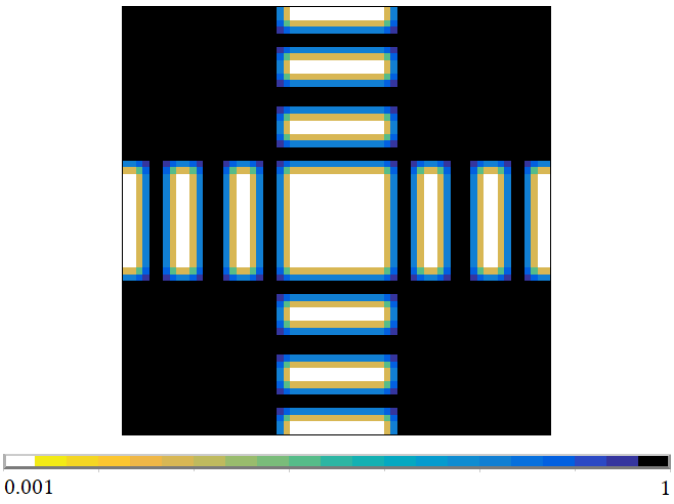

c. Initial design 5

Figure 5.24: Multiple hole initial designs for the shear load with 90% volume fraction

For every volume fraction, the initial designs that originate the best final solutions are square holes with as many slots as possible, without compromising the discretized finite element mesh of the plate.

Chapter 6

Results

6.1 Introduction

In this chapter, the optimal designs obtained through the use of optimization methods will be presented. The results are divided into three sections, each one concerning a different macroscopic applied load. For every particular load, the different problems are ordered by increasingly higher design freedom, meaning lower peak stress values are to be expected. In the end of every section, the various approaches to the same problem are critically discussed, and conclusions will be drawn.

The tables displayed in the present chapter contemplate only the most important informations for the analysis and discussion of the optimal designs obtained. Further pertinent information is present in the Appendixes chapter, following a similar organization.

For the loads where the product of the macroscopic eigenstresses is positive, the theoretical value of the minimum peak stress value is given by equation 6.1 [54], where V^* is the volume fraction of the unit cell, ranging from 0 to 1.

$$\sigma_{Max}^{Theo.} = \frac{\mathrm{Tr}(\langle \sigma_{ij} \rangle)}{V^*} \tag{6.1}$$

For problems where theoretical results exist, two error measures are used to evaluate the optimality of the obtained solution. The first one, presented in equation 6.2, corresponds to the relative error of the obtained peak stress, σ_{Max}^{VM}, relative to the known theoretical value. However, this value alone may be misleading, as the obtained peak stress value is obtained through a numerical procedure, and as so, is subject to discretization and numerical errors, resulting in an underestimate of the real peak stress value.

$$\delta = \left| \frac{\sigma_{Max}^{VM} - \sigma_{Max}^{Theo.}}{\sigma_{Max}^{Theo.}} \right| \tag{6.2}$$

Then, in order to assess the optimality of the final design, a second error measure is introduced, defined as in equation 6.3. The value of Δ indicates how uneven the stress distribution around the edge of the hole, which should theoretically be uniform. Through using error evaluation techniques based equations 6.3 and 6.2, it is possible to correctly assess the optimality of the obtained solution.

$$\Delta = \left. \frac{\sigma_{Max}^{VM} - \sigma_{Min}^{VM}}{\sigma_{Max}^{VM} + \sigma_{Min}^{VM}} \right|_{\Gamma} \tag{6.3}$$

The microstructures are modelled with materials with Young's moduli ranging from 1Pa to 1GPa. For the single material unit cells, the solid phase has a Young's modulus of 1GPa, and the void has 1Pa. When soft material rings are introduced, a design variable is responsible for varying its Young's modulus, although it is always contained in the interval between 1Pa and 1GPa. In topology optimization, the Young's moduli of the elements also range from 1Pa to 1GPa. The Poisson's ratio is kept constant, and equal to 0.3, for every Young's modulus value.

Both the hydrostatic and shear loads have macroscopic stress components of norm 1MPa. For the biaxial load case, whichever is the ratio of the stresses in both directions, their value is always chosen so that $\langle \sigma_{11} \rangle + \langle \sigma_{22} \rangle = 2\text{MPa}$.

6.2 Hydrostatic Load ($\langle \sigma_{11} \rangle = \langle \sigma_{22} \rangle$)

6.2.1 Single Material Parametrization

The reader is referred to appendix A.1, where a detailed description of the optimal results is made. Concerning the single material results, it can be seen in table A.1 that the peak stress in the plate is very close to the theoretical one for every volume fraction, with relative errors well below 0.5%. Furthermore, the stress is nearly uniform along the boundary of the hole, with every value of Δ being below 1%. The maximum stress verified in the plate is along the free boundary, like predicted by the theory, and its distribution along the edge of the hole for every volume fraction is summed up in figure 6.1, along with the optimal shapes.

Additionally, the problem of the minimization of the peak stress is equivalent to the maximization of the bulk modulus. In figure 6.2, the macroscopic bulk and shear moduli of the optimized microstructures is plotted for every volume fraction, with the respective Hashin-Shtrikman bound for reference. While it easily allows for a qualitative evaluation of the results,

its numerical values are quantitatively presented in table 6.1 in order to facilitate an accurate interpretation of the obtained results.

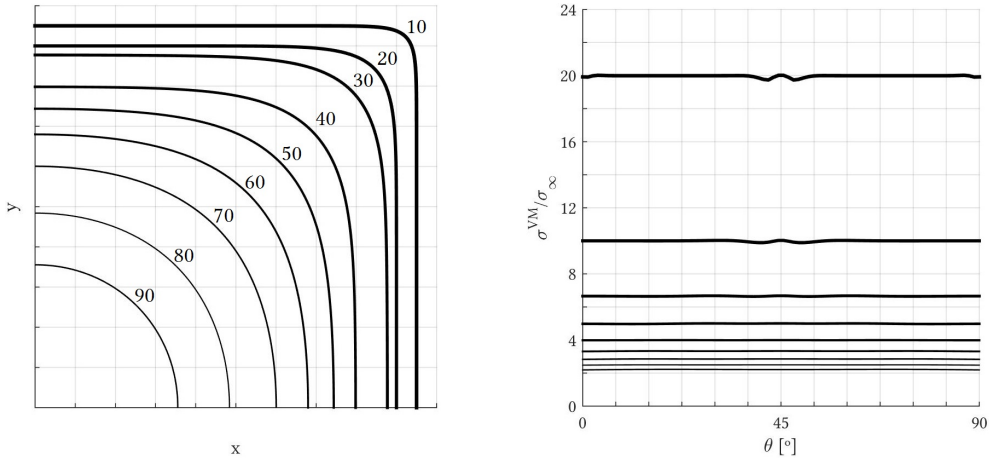

a. Shape of the boundaries

b. Stress value along the boundaries

Figure 6.1: Shape optimization solutions for the minimum peak equivalent stress designs for the hydrostatic load

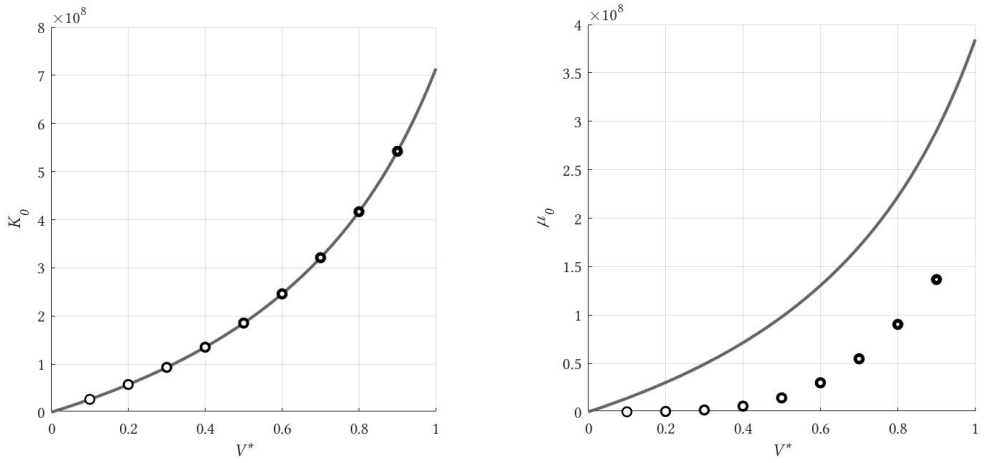

a. Bulk Modulus

b. Shear Modulus

Figure 6.2: Macroscopic elastic properties of the optimal single material designs for the hydrostatic load

As would be to expect, the optimal designs for the hydrostatic load have a bulk modulus nearing its bound, reassuring that the obtained microstructures are, in fact, optimal. However, the designs are quite poor from a shear moduli point of view. With the theoretical results being

successfully replicated, the peak stress value will be lowered by introducing another material phase.

Table 6.1: Peak equivalent stress and elastic constants of the optimal single material designs, and comparison with the theoretical ones

		Volume fraction V [%]								
		90	80	70	60	50	40	30	20	10
σ_{max}^{VM}	Theoretical	2.2222	2.5000	2.8571	3.3333	4.0000	5.0000	6.6667	10.000	20.000
	Numerical	2.2248	2.4973	2.8550	3.3339	3.9937	5.0050	6.6776	10.023	20.017
δ [%]		0.1141	0.1088	0.0738	0.0176	0.1565	0.1005	0.1641	0.2686	0.0870
Δ [%]		0.7779	0.3210	0.4323	0.3589	0.1055	0.3665	0.3381	0.6923	0.7098
$10^8 * \kappa$	Theoretical	5.4217	4.1667	3.2110	2.4590	1.8519	1.3514	0.9317	0.5747	0.2674
	Numerical	5.4220	4.1672	3.2114	2.4592	1.8520	1.3514	0.9318	0.5748	0.2676
δ [%]		0.0061	0.0140	0.0116	0.0088	0.0066	0.0064	0.0098	0.0141	0.0802
$10^8 * \mu$	Theoretical	2.9032	2.2222	1.7073	1.3043	0.9804	0.7143	0.4918	0.3030	0.1408
	Numerical	1.3670	0.9034	0.5480	0.2999	0.1444	0.0590	0.0194	0.0044	0.0004
δ [%]		52.916	59.349	67.904	77.002	85.267	91.738	96.056	98.535	99.612

6.2.2 Two Material Phases Parametrization

While with the single material microstructure the peak stress value is located on the boundary of the hole, that is no longer necessarily the case with a multi-material one. The maximum equivalent stress may or may not be located on the boundary of the hole, depending on the volume fraction and parametrization used. The addition of a softer homogeneous material ring lowers the peak stress along the cavity on the plate. As a consequence, a discontinuity on the stress distribution on the plate is generated in the boundary between the two distinct material phases, as can be seen in the figures on tables A.3 through A.6. That can be explained by the smoothness of the displacement function, which in turn guarantees continuity of the strain function, leading to similar values of strain on the elements neighbouring the material discontinuity. As so, recalling Hooke's Law, similar strain values with drastically different Young moduli result in different stress values.

The existence on more than one 'hotspot' for stress peaks means that, in order to minimize the peak equivalent stress on the whole plate, the optimal solution is going to be equally solicited in both zones where the maximum stress values exist. For instance, in the case of very high

volume fractions (90 through 99%), the most effective idea is to have a superelliptic hole with a soft homogeneous ring around it. The optimal boundary separating the different material phases is also roughly superelliptic. In tables A.3 and A.5, the optimal shapes can be seen, along the value of the Young's modulus, in both written and graphical form. The application of optimization tools leads to two equally stressed boundaries, each with an almost constant stress distribution around them. In the initial design, the two boundaries have different peak stress values. As the optimization goes on, the algorithm lowers the peak stress in one boundary at the expense of increasing the one in the other boundary. With the maximum equivalent stress in each boundary being equal, the algorithm can no longer benefit one boundary in detriment of the other, and optimization comes to an end. This condition can be seen in figure 6.3, where the von-Mises stress in the section $y_2 = 0$ is plotted. The black line is the stress that a single-material design would be subject to, as opposed to the optimal design with two material phases, represented by the coloured line.

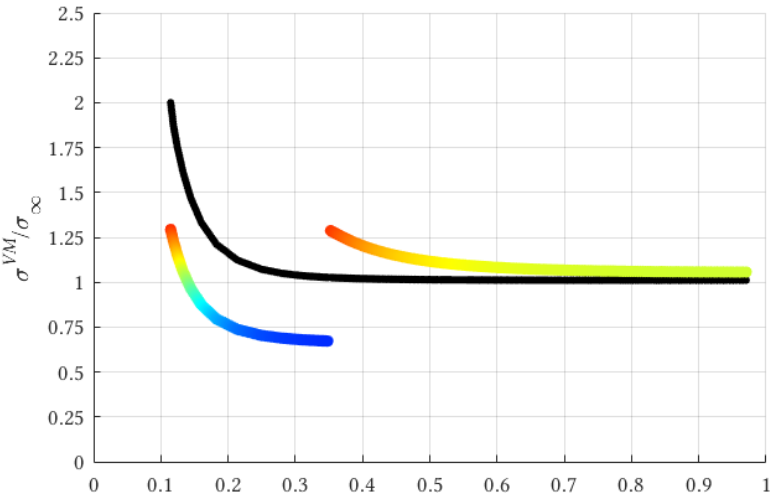

Figure 6.3: von-Mises stress distribution along the $y_2 = 0$ section (critical section) of the optimal design for the hydrostatic load case with 99% volume fraction using the supershape parametrization (Table A.5), with the single material stress distribution as a reference from Table A.1

For intermediate volume fractions of (80 through 60%), a simple superellipse no longer guarantees the best results (compare tables A.3 and A.5). As the volume fraction decreases, the narrowest section of the unit cell (the one intersected by the y_1 or y_2 axes) gets thinner, leading to the stress distribution in that zone being more uniform when compared to the highest volume fractions, which can be noticed in table A.1. This effect has implications on the optimal design with two material phases. In practice, for very high volume fractions, the addition of a softer material relaxes the zone nearby the hole by increasing the solicitation on the area

with the original hard material phase. Now, with the narrowest section being more and more evenly stressed from the outset, this strategy is no longer viable. The addition of a thick ring of a very soft material around the hole would overload the outside zone, leading to a bigger stress concentration than the original, single material design. While the superellipse only has flexibility to apply this progressively less effective strategy (see table A.3), the supershape has the ability to follow another approach. The shape of the material-material boundary is such that a thin soft material layer is around the hole in the most critical zone on the unit cell, at the 0° and 90° directions. By having a very thick layer of soft material in the 45° direction, the stress field is disturbed in such a way that the stress distribution in the most critical zone is almost evened out. This is easily identifiable in the 80 and 70% designs in table A.5, resulting in significantly more efficient designs from a peak stress value perspective. This can be seen in figure 6.4, where the von-Mises stress distribution in the critical section is plotted, for the optimal designs with two material phases for the 80% volume fraction, with the stress distribution of the optimal single material design as reference. It is showcased that the increased flexibility of the supershape parametrization translates in a superior design when compared to the simpler parametrization.

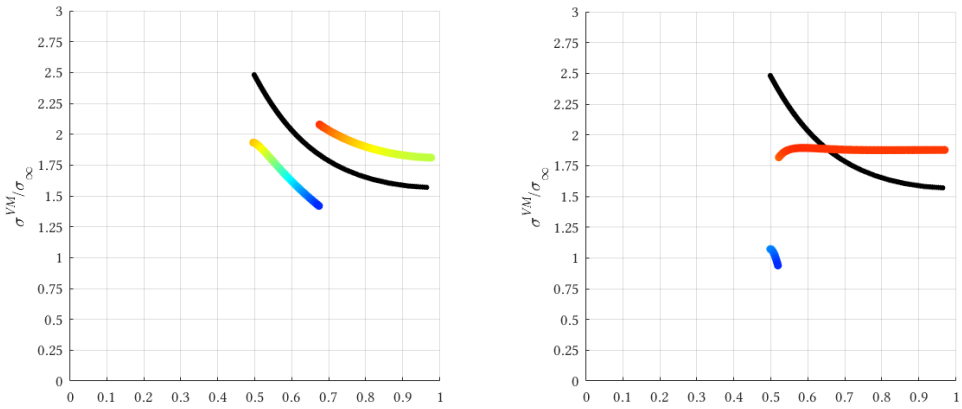

a. Superellipse parametrization (table A.3)

b. Supershape parametrization (table A.5)

Figure 6.4: von-Mises stress distribution along the $y_2 = 0$ section (critical section) of the optimal design for the hydrostatic load case with 80% volume fraction, with the single material stress distribution as a reference (table A.1)

For volume fractions below 50%, the strategy of introducing a soft material around the hole is no longer very effective. As can be seen in table A.1, with one material phase only, the stress distribution along the critical section of the unit cell is naturally very uniform. Recalling that the purpose of the soft material is to redistribute the stress in this section in a more even manner, it is to expect that the reduction in the peak stress values are not so good. Still, this technique was used for the lower volume fraction with the simpler parametrization, to check until how

low of a volume fraction it is possible to still have a gain, which can be seen in table A.3. Every reduction is now below 5%, and for the lower volume fraction, the single material theoretical minimum couldn't even be achieved. The evenness of the stress distribution along the critical section for the single material microstructure can be seen in figure 6.5. It can also be observed that the hole of the multi-material design has a lower diameter in the $y_2 = 0$ section for the same volume fraction, since the hole is more square-like than its single material counterpart.

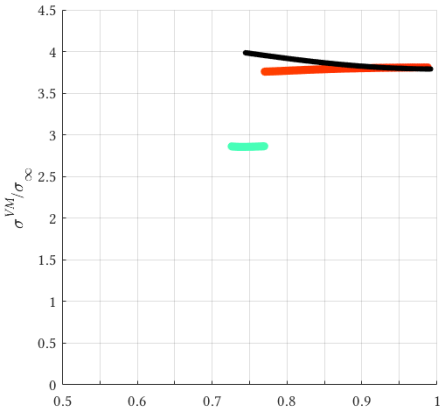

Figure 6.5: von-Mises stress distribution along the $y_2 = 0$ section (critical section) of the optimal design for the hydrostatic load case with 50% volume fraction using the superellipse parametrization, with the single material stress distribution as a reference

The maximum equivalent stresses for the optimal designs with two material phases for the hydrostatic load are summed up in table 6.2. Since the superellipse is a particular case of the supershape, the latter parametrization always leads to a design with increased performance (lower peak equivalent stress).

6.2.3 *n* Material Phases Formulation

When introducing additional material phases, the resulting Young's modulus field in the plate resembles a discretized version of a functionally graded material, with the material interfaces being lines of constant Young's modulus. This method was only employed for the hydrostatic version of the problem of minimization of the peak equivalent stress, since the solution is guaranteed to have cubic symmetry, which allows for a reduction of the number of design variables. Furthermore, only the 99 and 95% volume fractions were explored in order to prove the viability of the methodology. The optimal Young's modulus and resulting equivalent stress distributions are represented in figures 6.6 and 6.7 for the volume fractions of 99 and 95% respectively.

Table 6.2: Summary of the optimal results for the minimization of the peak von-Mises stress for microstructures with two material phases

V[%]	Theoretical	Superellipse Parametrization		Supershape Parametrization	
	σ_{max}^{VM}	σ_{max}^{VM}	Reduction [%]	σ_{max}^{VM}	Reduction [%]
99	2.0202	1.2995	35.67	1.2945	35.92
95	2.1053	1.4689	30.23	1.4654	30.39
90	2.2222	1.6314	26.59	1.6260	26.82
80	2.5000	2.0787	16.85	1.9023	23.91
70	2.8571	2.5462	10.88	2.4322	14.87
60	3.3333	3.0814	7.56	3.0529	8.41
50	4.0000	3.8284	4.29	_____	_____
40	5.0000	4.8224	3.55	_____	_____
30	6.6667	6.6234	0.65	_____	_____
20	10.000	10.045	-0.45	_____	_____

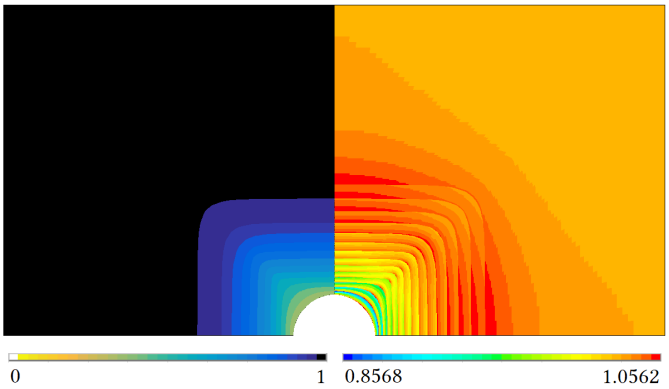

Figure 6.6: Optimal design with 99% volume fraction for the hydrostatic load with 15 material phases

The obtained peak stress values for each optimal design are displayed in table 6.3. Through the introduction of more than two soft material phases surrounding the hole, the maximum equivalent stress in the plate can be reduced far beyond the theoretical single material value, almost attaining a uniform stress state throughout the whole unit cell.

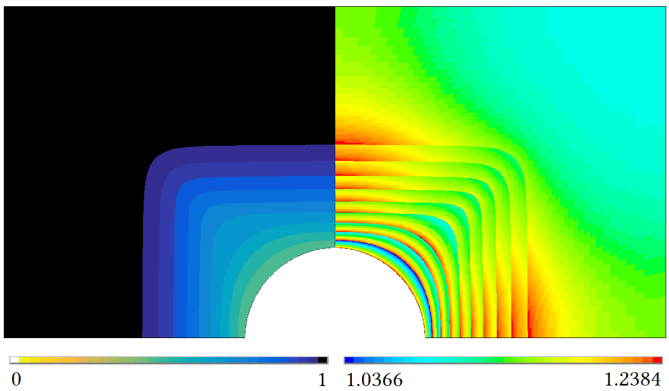

Figure 6.7: Optimal design with 95% volume fraction for the hydrostatic load with 10 material phases

Table 6.3: Summary of the optimal results for the minimization of the peak von-Mises stress for microstructures with two material phases

$V[\%]$	Theoretical	n Material Phases	
	σ^{VM}_{max}	σ^{VM}_{max}	Reduction [%]
99	2.0202	1.0562	47.72
95	2.1053	1.2384	41.18

6.2.4 Variable Thickness Plate

The most design flexibility is achieved with the variable thickness plate approach. Instead of being limited by the number of material phases present in the microstructure, every element of the finite element mesh has a design variable corresponding to the Young modulus of the plate in that point, E/E_{max}, with the freedom to have any value. The formulation with n-material phases can be thought of as a particular case of this approach, since the number of different phases is limited by n, and the shape of the interfaces is implicitly constrained by the flexibility of the superellipse equation. Furthermore, this method allows for a change in the topology of the plate, with the ability to add[1] and remove void phase areas.

The optimal designs using this method can observed in table A.7. The Penalization Weight quantifies the contribution of the compliance term to the objective function, as seen in equation 6.4. It is desirable for it to be as low as possible, if not zero, so that the optimization problem is

[1]Given the limitations associated with the modified volume calculation function, the ability to create holes is significantly reduced. That being said, it is easily seen when the algorithm tries to open a new hole but can't, and adjustments can be made to the initial design, leading improved final designs.

as similar to the minimization of the peak stress as possible.

$$\mathrm{PW} = \frac{\Psi C}{\Psi C + z} \tag{6.4}$$

For the highest volume fraction, the optimal density field (stiffness distribution) leads to a fully stressed design. This condition is also almost achieved by the volume fraction of 95%. These designs have a similar density distribution on the plate, and the same topology (one hole in the middle of the plate). As the volume fraction decreases, this is no longer the case. Starting at 90%, the optimal topology includes another hole, namely in the corners of the unit cell. When concerning the optimal design using shape optimization with two material phases, the importance of the most critical section was discussed. If no holes were present in the corners of the unit cell, there would be a considerable area of not very stressed material in that zone. So, by putting void phase in an area where the equivalent stress values were originally relatively low, the central hole can now be smaller while still granting the volume fraction constraint is respected. This creates a second critical zone in the unit cell. Now, the algorithm finds rearranges the size of the holes and the density field a around them in order to have two equally stressed sections, at 0° and 45° respectively. This is the recurring idea behind all the designs of volume fractions of 90% and below. As the volume fraction decreases, the benefits of having a variable thickness decrease, at it is seen by the peak stress values presented in table 6.4.

Table 6.4: Summary of the optimal results for the minimization of the peak von-Mises stress for variable thickness microstructures subject to a hydrostatic load

V[%]	Theoretical	FGM		
	σ_{max}^{VM}	σ_{max}^{VM}	Reduction [%]	Penalization Weight [%]
99	2.0202	1.0569	47.64	0
95	2.1053	1.2255	41.79	0
90	2.2222	1.4050	36.78	0
80	2.5000	1.8104	27.58	0
70	2.8571	2.2750	20.38	0
60	3.3333	2.9387	11.84	0.81

6.2.5 Optimal Second Rank Laminate

A microstrucure as represented in figure 6.8 is able to attain a state of uniform equivalent stress in the material, when subject to a macroscopic load where $\sigma_1\sigma_2 > 0$ (equation 6.5). The

constant m is the ratio between the two macroscopic eigenstresses, and is greater than the unity, meaning the biggest stress is aligned with the direction y_1.

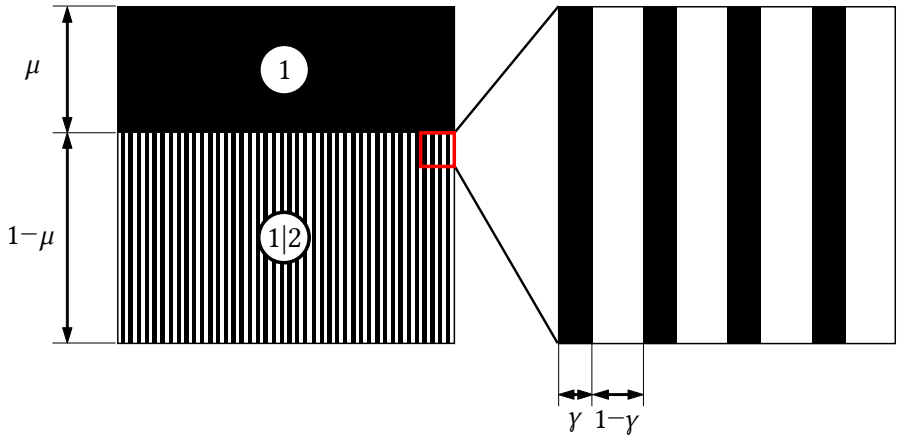

Figure 6.8: Optimal rank-2 composite material for the minimum peak equivalent when subject to a macroscopic load where $\sigma_1\sigma_2 > 0$

$$\langle\sigma_{ij}\rangle = \begin{bmatrix} m\sigma_\infty & 0 \\ 0 & \sigma_\infty \end{bmatrix}, \qquad m \geq 1 \tag{6.5}$$

Considering the (1|2) region is a ranked laminate comprised of unidirectional fibres, the stress components in each region may be calculated, and are summed up in equation 6.6.

$$\begin{aligned} \sigma_{11_{(1)}} &= \frac{m\sigma_\infty}{\mu} & \sigma_{22_{(1)}} &= \sigma_\infty \\ \sigma_{11_{(1|2)}} &= \frac{\sigma_\infty}{\gamma} & \sigma_{22_{(1|2)}} &= \frac{\sigma_\infty}{\gamma} \end{aligned} \tag{6.6}$$

For the two-dimensional stress state in the principal referential, the von-Mises equivalent stress simplifies to $\sigma^{VM} = \sqrt{\sigma_1^2 + \sigma_2^2 - \sigma_1\sigma_2}$. Once knowing every stress component in regions (1) and (1|2), the von-Mises equivalent stress in each region may be calculated, and it is imposed that they must be equal, as displayed in equation 6.7.

$$\sqrt{\left(\frac{m\sigma_\infty}{\mu}\right)^2 + \sigma_\infty^2 - \frac{m\sigma_\infty^2}{\mu}} = \frac{\sigma_\infty}{\gamma} \tag{6.7}$$

By manipulating equation 6.7, a quadratic expression relating the lengths μ and γ can be obtained, as a function of the ratio between the macroscopic eigenstresses, m. Through a geometrical interpretation of μ and γ presented in [21], it can be observed that they evolve

monotonically with one another. Furthermore, every combination of μ and γ corresponds to a certain volume fraction of material which also evolves monotonically, given by 6.8.

$$V = \mu + \gamma(1 - \mu) \tag{6.8}$$

Combining equations 6.7, 6.8 and 6.6, the uniform equivalent stress in the microstructure can be plotted as a function of m, as is done in 6.9.

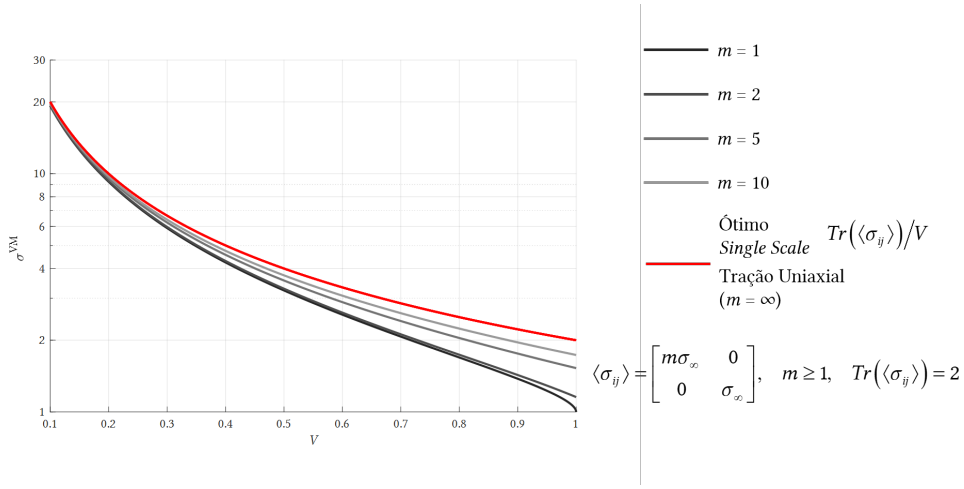

Figure 6.9: Uniform equivalent stress in a second rank laminate subject to a macroscopic load where $\langle\sigma_1\rangle\langle\sigma_2\rangle \geq 0$ as a function of m

As can be seen directly from 6.9, as the macroscopic load approaches the uniaxial case, the material is subject to a harsher stress state. In the limit situation, $m = \infty$, the microstructure is made up only of unidirectional fibres, hence the equivalent stress is the same as in the theoretical result for single scale microstructures. Additionally, as the volume fraction decreases, the equivalent stress converges to the trace of the macroscopic load.

6.2.6 Summary

The peak stresses regarding every optimal design for the hydrostatic load are presented in table 6.5. As would be to expect, it can be observed that, for every particular volume fraction, the optimal design obtained through a formulation with increased flexibility always has a better performance than its less flexible counterparts. The compliance term in the objective function was almost not necessary for this load, with Ψ only differing from zero in the lowest volume fraction.

Table 6.5: Peak stress values obtained by optimal designs for the hydrostatic load

V [%]	$\sigma^{VM}_{Max}/\sigma_\infty$					
	Theoretical	SMSO	MMSO[2]	MMSO[3]	MMSO[4]	FGM
99	2.0202	———	1.2995	1.2945	1.0562	1.0569
95	2.1053	———	1.4689	1.4654	1.2384	1.2255
90	2.2222	2.2248	1.6314	1.6260	———	1.4050
80	2.5000	2.4973	2.0787	1.9023	———	1.8104
70	2.8571	2.8550	2.5462	2.4322	———	2.2750
60	3.3333	3.3339	3.0814	3.0529	———	2.9387
50	4.0000	3.9937	3.8284	———	———	———
40	5.0000	5.0050	4.8224	———	———	———
30	6.6666	6.6776	6.6234	———	———	———
20	10.000	10.027	10.0447	———	———	———
10	20.000	20.017	———	———	———	———

A graphical representation of table 6.5 is presented on figure 6.10. The grey curve represents the theoretical peak von-Mises stress on a single material microstructure, while the black function represents the stress in a uniform plate. The red dots correspond to the optimal designs with two material phases, with the best parametrization available for every volume fraction. The blue dots are the optimal functionally graded designs.

[2]Multi-material Shape Optimization - Two Material Phases - Superellipse Parametrization
[3]Multi-material Shape Optimization - Two Material Phases - Supershape Parametrization
[4]Multi-material Shape Optimization - n Material Phases - Superellipse Parametrization

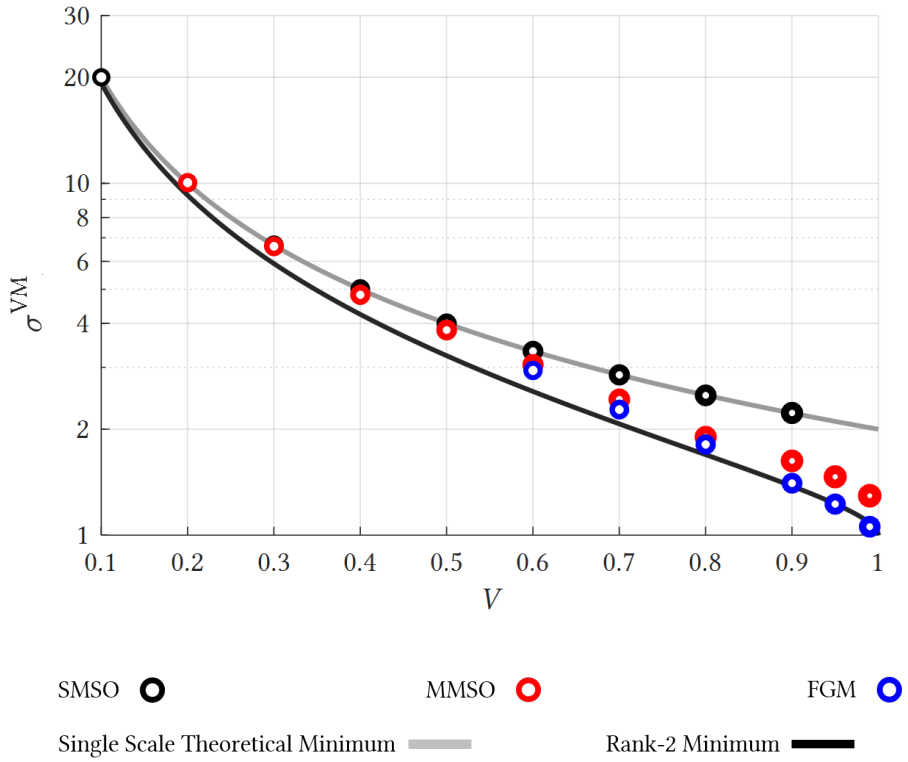

Figure 6.10: Comparison between the optimal designs and the proposed minimum peak equivalent stress attainable for the hydrostatic load

6.3 Biaxial Load ($\langle\sigma_{11}\rangle = 2\langle\sigma_{22}\rangle$)

6.3.1 Single Material Formulation

Much like the hydrostatic load, the obtained optimal designs (see figure 6.11a) are in conformity with the known theoretical results. As seen in table 6.6, the peak stress values correctly adjust the theoretical ones, and the stress is almost uniform along the free boundary of the plate as shown in figure 6.11. Most of the error measures associated with the optimality conditions (δ and Δ) are well below 1%, meaning the optimality conditions of the problem are almost attained, and the optimization process was successful. An in-depth description of the optimal designs can be found in tables B.1 and B.2.

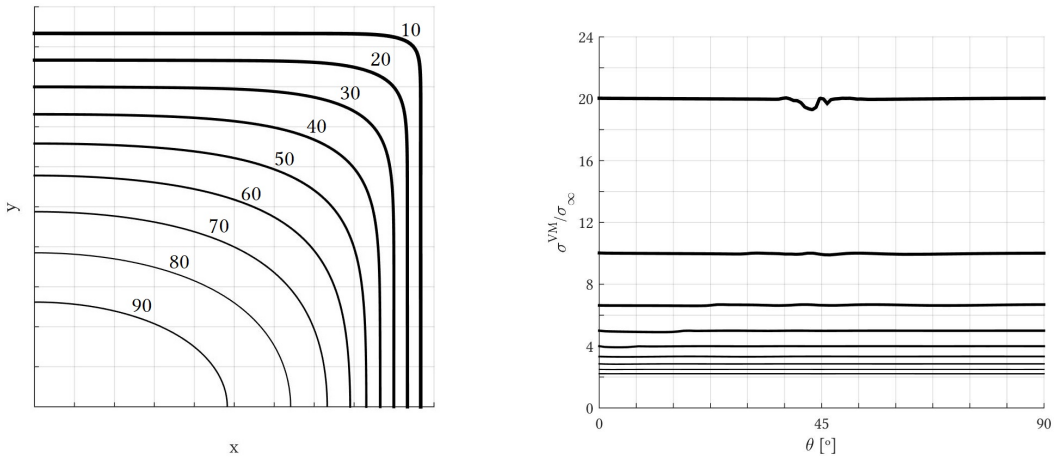

a. Shape of the boundaries

b. Stress value along the boundaries

Figure 6.11: Shape optimization solutions for the minimum peak equivalent stress designs for the biaxial load

Table 6.6: Peak equivalent stress values of the optimal single material designs for the biaxial load

		Volume fraction V [%]								
		90	80	70	60	50	40	30	20	10
σ^{VM}_{max}	Theoretical	2.2222	2.5000	2.8571	3.3333	4.0000	5.0000	6.6667	10.000	20.000
	Numerical	2.2130	2.4930	2.8521	3.3331	3.9947	4.9970	6.6849	10.023	20.055
δ [%]		0.4170	0.2794	0.1781	0.0064	0.1315	0.0608	0.2742	0.2252	0.2728
Δ [%]		0.0543	0.1374	0.3616	0.4529	0.9288	0.9409	0.6061	0.6270	1.9399

6.3.2 Two Material Phases Formulation

Just like in the hydrostatic load case, a softer material region around the hole was introduced, with two different parametrizations used, which differ by their design freedom. As in the hydrostatic load case, the algorithm explores the existence of two boundaries, this time by having three stress peaks in the plate, one in the void-material boundary, and two additional ones in the material-material boundary. Unlike the superellipse parametrization, boundaries defined by the supershape have enough flexibility to create stress peaks outside the interfaces between different material phases. The optimal designs with these parametrizations for the biaxial load are displayed in tables B.3 through B.6. Although the supershape parametrization leads to designs with increased performance when compared to the superellipse ones, the difference is not as significant as in the hydrostatic load case. The peak stress values may be seen in table 6.7, as well as the corresponding reduction when compared to the single material theoretical minimum.

Table 6.7: Summary of the optimal results for the minimization of the peak von-Mises stress for microstructures with two material phases

V[%]	Theoretical	Superellipse Parametrization		Supershape Parametrization	
	σ_{max}^{VM}	σ_{max}^{VM}	Reduction [%]	σ_{max}^{VM}	Reduction [%]
99	2.0202	1.4367	28.88	1.4293	29.25
95	2.1053	1.6414	22.03	1.6010	23.95
90	2.2222	1.8436	17.03	1.8222	18.00
80	2.5000	2.2135	11.46	2.1356	14.58
70	2.8571	2.6472	7.34	2.5915	9.30
60	3.3333	3.1514	5.46	3.1346	5.96

6.3.3 Variable Thickness Plate

The optimal functionally graded material designs are compiled in tables B.7 and B.8. Only the designs for volume fractions of 90% and under are subject to a macroscopic load where $\langle\sigma_1\rangle = 2\langle\sigma_2\rangle$, and its reasoning will be explained ahead.

The freedom that the algorithm has to give every material point its own Young's modulus allows him to even out the equivalent stress on the critical sections of the microstructure, being $y_2 = 0$ and $y_1 = 0$. In order to have static equilibrium, if the unit cell is cut in one of these sections, the stress must be such that the sum of the forces is zero. Since the stress components (i.e. σ_{11} at $y_1 = 0$, and σ_{22} at $y_2 = 0$) are almost uniform in these sections, this results in ratio of

the critical sections of the unit cell being equal to the ratio of macroscopic stresses applied in the unit cell. This explains why the volume fractions of 99 and 95% could not be solved for a load with a ratio of 2. With the mesh used (64x64), the optimal distribution of the void phase in these plates would be a very narrow ellipsoid, with the ratio of critical sections being 2. The sole existence of the density filter on the topology optimizations means the filtered density field no longer has a hole, since the hole would have two or four elements across the small radius of the ellipse. As such, the ratio of macroscopic stresses is 1.5 for the 95% volume fraction and 1.25 for the 99% one. For every load, the value of the stresses is such that $\langle\sigma_1\rangle + \langle\sigma_2\rangle = 2$. The obtained peak stresses for the optimal designs are presented in table 6.8. In that same table, it can be seen that there was only need for a strain energy term in the objective function for the lowest volume fractions, in order to maintain connectivity. Even then, the contribution of the penalization term to the objective function isn't of much significance, meaning the modified objective function is almost equivalent to the minimization of the peak stress, which is the originally indented optimization problem.

Table 6.8: Summary of the optimal results for the minimization of the peak von-Mises stress for variable thickness microstructures subject to a biaxial load

V[%]	Theoretical	FGM		
	σ_{max}^{VM}	σ_{max}^{VM}	Reduction [%]	Penalization Weight [%]
99	2.0202	1.0569	47.64	0
95	2.1053	1.2255	41.79	0
90	2.2222	1.4050	36.78	0
80	2.5000	1.8104	27.58	0.55
70	2.8571	2.2750	20.38	0.61
60	3.3333	2.9387	11.84	1.27

6.3.4 Summary

The peak stress values regarding every volume fraction are displayed in table 6.9, with every strategy employed for the biaxial load case. Unlike the optimal microstructures for the hydrostatic load, the functionally graded microstructures are not strictly better than the ones obtained with shape optimization. If the mesh of the topology optimization was finer, the results could probably be improved. Still, in general, more flexible parametrizations lead to designs with better performance.

Figure 6.12 is a graphical representation of table 6.9. The black line represents the stress a

plate would be subject to if it was to be an homogeneous one, calculated through the von-Mises equivalent stress equation. The grey line represents the minimal possible peak stress in the plate, which the obtained single material designs manage to replicate. As the volume fractions get lower, the used strategies to lower the peak stress in the plate become less and less impactful, since the multi-material designs converge to the theoretical single material curve.

Table 6.9: Peak stress values obtained by optimal designs for the hydrostatic load

V [%]	$\sigma_{Max}^{VM}/\sigma_\infty$				
	Theoretical	SMSO	MMSO[5]	MMSO[6]	FGM
99	2.0202	———	1.4367	1.4293	1.1169[7]
95	2.1053	———	1.6414	1.6010	1.3739[8]
90	2.2222	2.2130	1.8436	1.8222	1.6725
80	2.5000	2.4930	2.2135	2.1356	2.0742
70	2.8571	2.8521	2.6472	2.5915	2.5396
60	3.3333	3.3331	3.1514	3.1346	3.2057
50	4.0000	3.9947	———	———	———
40	5.0000	4.9970	———	———	———
30	6.6666	6.6849	———	———	———
20	10.000	10.023	———	———	———
10	20.000	20.055	———	———	———

[5]Multi-material Shape Optimization - Two Material Phases - Superellipse Parametrization
[6]Multi-material Shape Optimization - Two Material Phases - Supershape Parametrization
[7]$\langle\sigma_1\rangle = 1.25\langle\sigma_2\rangle$
[8]$\langle\sigma_1\rangle = 1.5\langle\sigma_2\rangle$

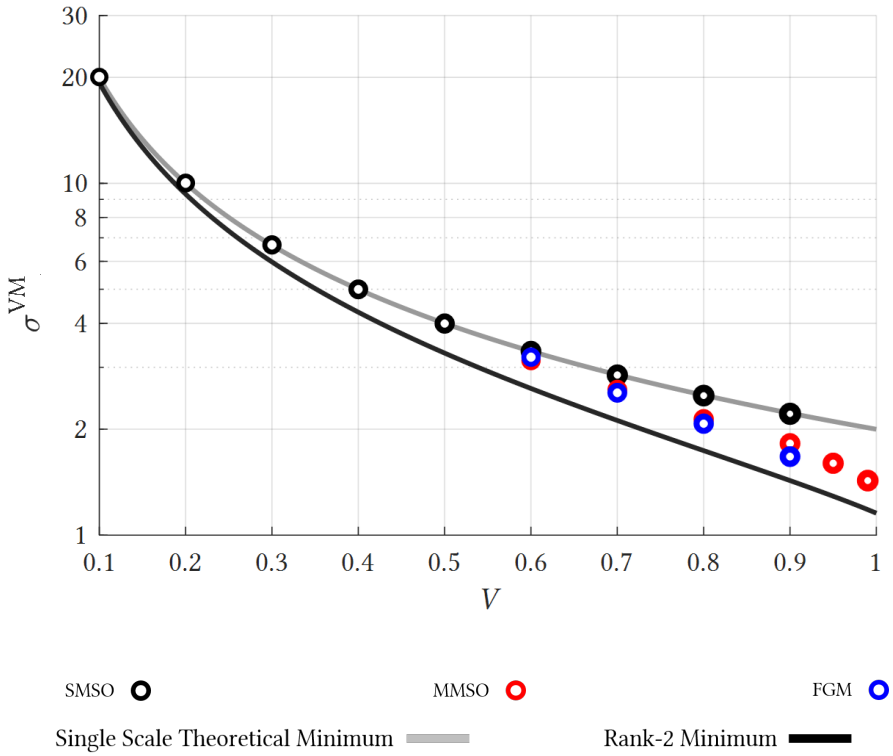

Figure 6.12: Comparison between the optimal designs and the proposed minimum peak equivalent stress attainable for the biaxial load

6.4 Shear Load ($\langle\sigma_{11}\rangle = -\langle\sigma_{22}\rangle$)

6.4.1 Single Material Formulation

Concerning the two single material problems, it is clear that, despite using the same formulation, the resulting optimal designs are clearly different (see tables C.1 through C.4. The optimal designs for the minimum strain energy are similar to the numerical simulations exposed in chapter 4, resembling square holes with rounded edges. For every volume fraction, the stress field is characterized by having only one relevant peak stress in the material domain[9] which is not on the free boundary of the plate.

Table 6.10: Summary of the optimal miscrostructures obtained for the shear load

V [%]	$\sigma^{VM}/\sigma_\infty$	
	SMSO Minimum strain energy	SMSO Minimum peak stress
90	2.7520	2.8813
80	3.2824	3.2775
70	3.9954	3.9474
60	4.7781	4.6101
50	5.7776	5.3726
40	7.2660	6.4245
30	9.9320	8.1779
20	14.2854	11.595
10	31.8132	21.618

The optimal designs regarding the peak stress value are somewhat identical to the aforementioned problem for high volume fractions (figures 6.13a and 6.13b). However, as the volume fraction decreases, the optimal designs are totally distinct. It is no longer in the best interest to have one big stress peak in the material domain. Instead, the hole has an increased radius in the x and y directions, which allows for the radius at the 45° direction to be reduced when compared to the minimum compliance design, while maintaining a constant volume fraction. This is easily identifiable in figures 6.13c through 6.13f. This results in the creation of a second relevant peak stress in the middle of every edge of the hole, as well as maintaining the one in the corners of the unit cell, which can be observed when comparing tables C.1 and C.3. The

[9] It has four or eight equal peak stresses, only due to the square symmetry of the unit cell

final design parameter values give birth to a design that has two equally stressed regions in the material domain, with its equivalent stress value being lower than the one in the minimal compliance design. The stress peaks for every volume fraction are displayed in table 6.10. The stress distribution along the optimal holes is displayed in figure ??.

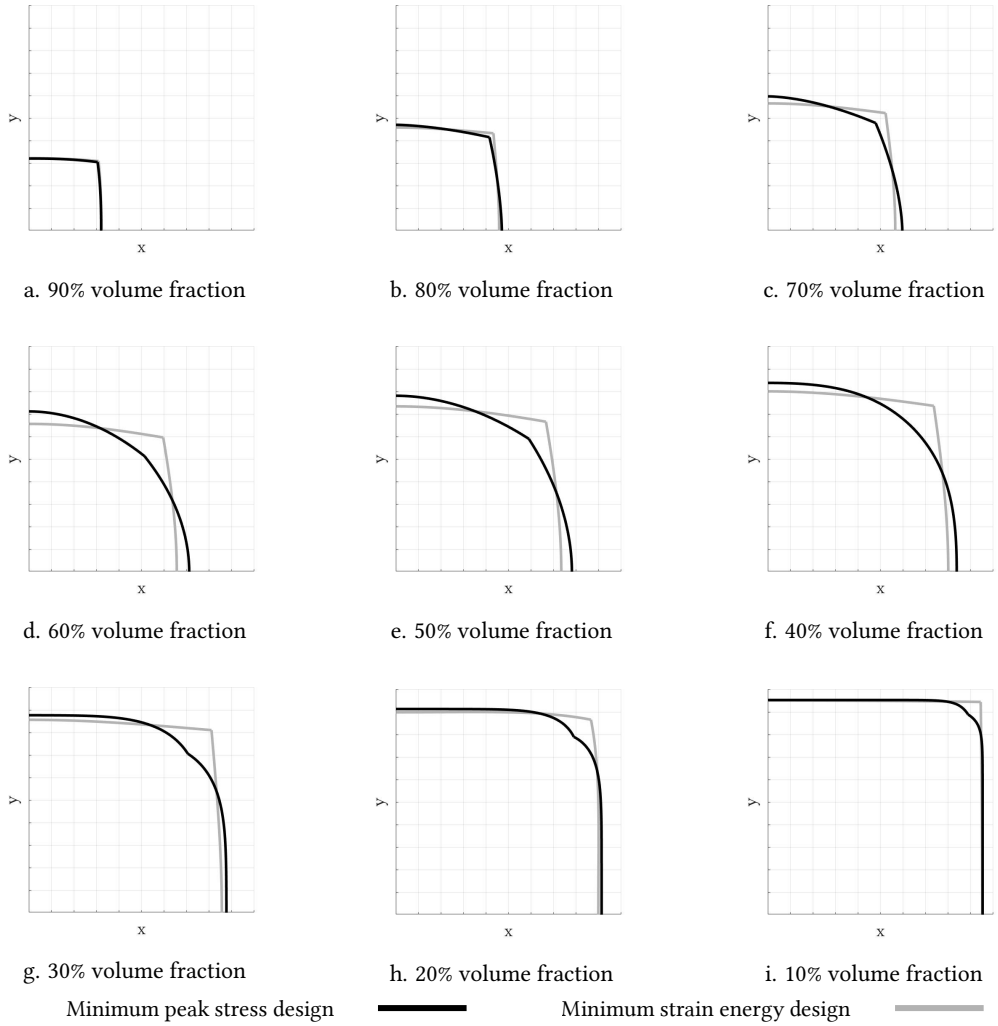

Figure 6.13: Comparison of the geometry of the holes of the optimal designs for the problems of the minimum strain energy and the minimum peak stress when subject to a shear load

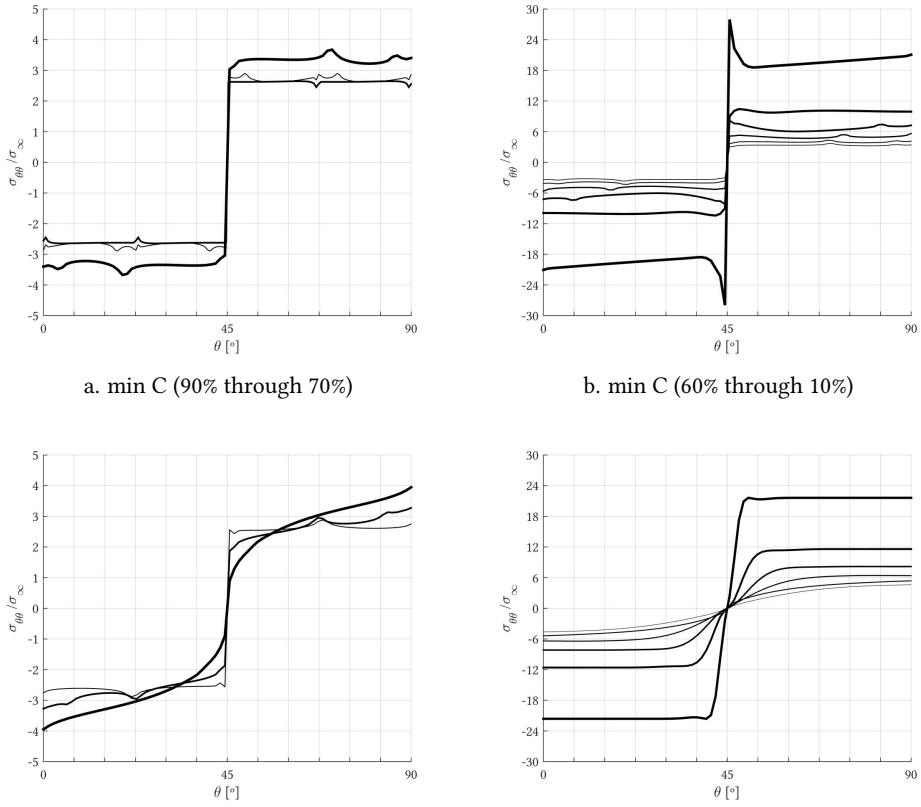

a. min C (90% through 70%)

b. min C (60% through 10%)

c. min max σ^{VM} (90% through 70%)

d. min max σ^{VM} (60% through 10%)

Figure 6.14: Stress distribution along the holes of the optimum designs for the pure shear stress load

6.4.2 Variable Thickness Plate

With the use of the variable thickness approach, the optimal designs are significantly improved, when compared to the shape optimization methodologies, and are presented in table C.5. As was discussed in the Implementation chapter, for every volume fraction, the final solution depends heavily on the initial design for the optimization. While the inability to generate new void regions on the plate is a concern for the every macroscopic load, it is most prevalent in the shear one. The holes seen in every optimal design have to be included in the initial design. If they are not, low density regions are generated in the plate where in fact, a hole should be. However, there is such thing as too many slots. If too many slots are introduced, which was attempted in the designs where the finite element mesh allows it, the optimization algorithm removes some slots and rearranges the remainder.

The optimal topology for this problem is a square-like hole in the center, with many slots parallel to the edges of the hole. Up to a certain amount of holes, this contributes to the reduction of the stress peak in the plate. There seems to be a certain amount of void area in the critical section for which the introduction of more slots is no longer beneficial, which originated the idea explained in the following subsection.

Unlike the hydrostatic and biaxial load, the compliance term in the objective function was heavily used for the shear load, as explicit in table 6.11. However, this may attributed to the fact that lower volume fractions were explored in the shear load case than in the other two, thus it would be unfair to take any conclusions. Still, this term may now have enough weight to alter significantly the optimal design other than guaranteeing connectivity, which is not desirable.

Table 6.11: Summary of the optimal results for the minimization of the peak von-Mises stress for variable thickness microstructures subject to a shear load

V[%]	FGM	
	σ_{max}^{VM}	Penalization Weight [%]
95	2.0541	0
90	2.2355	0
80	2.5913	0.78
70	3.1488	1.55
60	3.7708	1.79
50	4.5300	1.86
40	5.9400	7.12
30	8.2998	6.14

6.4.3 Optimal Second Rank Laminate

It is conjectured that a rank-2 composite like the one represented in figure 6.15 would be able to attain a fully stressed design when subject to a pure shear load, meaning traction along the y_1 direction and compression along y_2 (equation 6.9), or vice versa. This microstructure was originally proposed in [46], as one that has extreme mechanical properties.

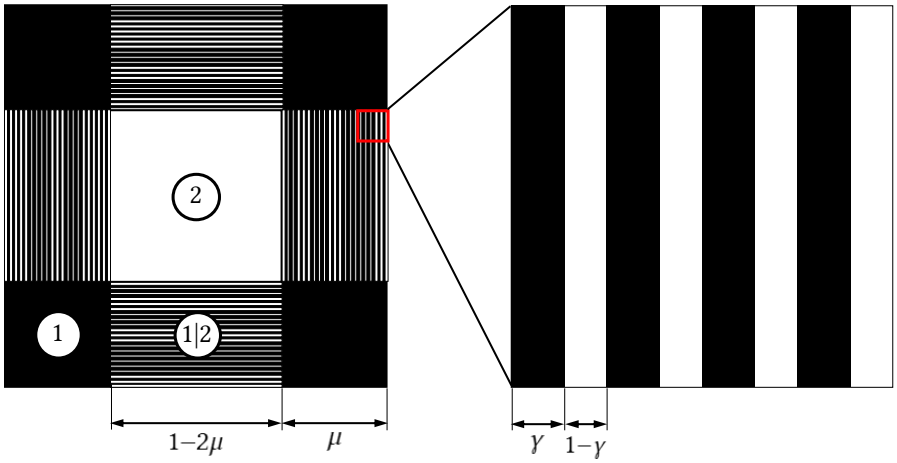

Figure 6.15: Optimal rank-2 composite material for the minimum peak equivalent when subject to a macroscopic pure shear load

$$\langle \sigma_{ij} \rangle = \begin{bmatrix} \sigma_\infty & 0 \\ 0 & -\sigma_\infty \end{bmatrix} \tag{6.9}$$

The zone (1) of the microstructure is comprised of a solid phase material with the characteristic dimension μ, and the zone (2) is void phase. Zone (1|2) is a laminate material with layers of solid and void phase. It is characterized by the lamination factor, γ. The second rank laminate has no stiffness in the direction perpendicular to the fibres. Thus, considering the edges of the cell have unit length, the stress components in each of the solid squares of edge μ are amplified by $1/2\mu$, in order to satisfy the static equilibrium condition. These zones are not subject to any tangential stress. The stress on the second rank laminate is uniaxial, since it only supports axial loads along the direction of the fibres[10]. Its value is the one felt in zone (1), amplified by a factor of $1/\gamma$. The stress components of these zones are presented in equation 6.10. The void phase is not solicited, as its stiffness is null.

$$\begin{aligned} \sigma_{11_{(1)}} &= \frac{\sigma_\infty}{2\mu} & \sigma_{22_{(1)}} &= -\frac{\sigma_\infty}{2\mu} \\ \sigma_{11_{(1|2)}} &= \frac{\sigma_{11_{(1)}}}{\gamma} = \frac{\sigma_\infty}{2\gamma\mu} & \sigma_{22_{(1|2)}} &= -\frac{\sigma_{22_{(1)}}}{\gamma} = -\frac{\sigma_\infty}{2\gamma\mu} \end{aligned} \tag{6.10}$$

The volumetric average of every component of stress in the microstructure must add up to the applied macroscopic load. This verification is made for the σ_{11} component in equation 6.11, confirming the obtained values. The procedure is exactly the same for σ_{22}, therefore it is not shown, and every component of σ_{12} is zero, which corresponds to the macroscopic load.

[10]Every entry of C_{ijkl} is zero except for C_{1111}, with the 1 direction corresponding to the direction of the fibers

$$\begin{aligned}\langle\sigma_{11}\rangle &= 4\sigma_{11_{(1)}}A_{(1)} + 2\sigma_{11_{(1|2)}}A_{(1|2)} = \\ &= 4\frac{\sigma_\infty}{2\mu}\mu^2 + 2\frac{\sigma_\infty}{2\gamma\mu}\mu(1-2\mu)\gamma = \sigma_\infty\end{aligned} \tag{6.11}$$

The von-Mises equivalent stress value can be computed for every zone of the microstructure, as shown in equation 6.12.

$$\begin{aligned}\sigma^{VM}\Big|_{(1)} &= \sqrt{\frac{1}{2}\left[\sigma^2_{11_{(1)}} + \sigma^2_{22_{(1)}} + (\sigma_{11_{(1)}} - \sigma_{22_{(1)}})^2\right]} = \sqrt{3}\frac{\sigma_\infty}{2\mu} \\ \sigma^{VM}\Big|_{(1|2)} &= \frac{\sigma_{11_{(1)}}}{\gamma} = \frac{\sigma_{22_{(1)}}}{\gamma} = \frac{\sigma_\infty}{2\gamma\mu} \\ \sigma^{VM}\Big|_{(2)} &= 0\end{aligned} \tag{6.12}$$

If the value of γ is $1/\sqrt{3}$, the von-Mises stress value is constant in every material point in the microstructure, attaining a fully stressed design. This condition leads to the lowest possible peak equivalent stress, for any given volume fraction. The volume fraction of the microstructure can be calculated through equation 6.13.

$$V = 4\mu^2 + 4\gamma\mu(1-2\mu), \qquad \mu \in]0, 0.5[, \quad \gamma \in]0, 1[\tag{6.13}$$

Considering a fixed value of γ, the value of V is only a function of μ. Equation 6.13 may be solved for μ, as an explicit function of the desired volume fraction of the microstructure, V. For every value of $\gamma \in]0, 1[$ there is one root where $\mu \in]0, 0.5[$, with the other root having no physical meaning.

$$\mu^* = \frac{-\gamma + \sqrt{\gamma^2 + V(1-2\gamma)}}{2(1-2\gamma)} \tag{6.14}$$

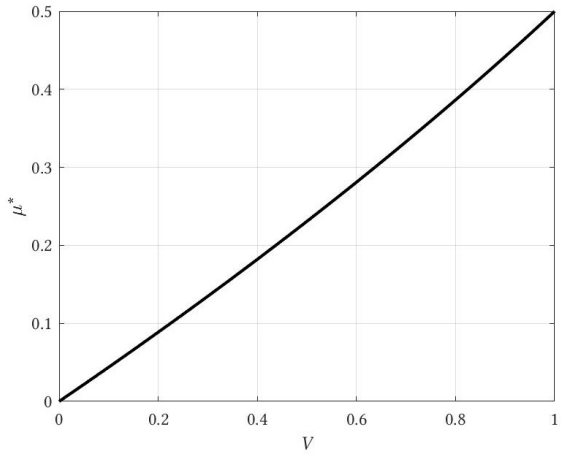

Figure 6.16: Optimal μ parameter as a function of the volume fraction ($\gamma = 1/\sqrt{3}$)

For the particular case of $\gamma = 1/\sqrt{3}$, the plot of μ as a function of the volume fraction of the microstructure is presented in figure 6.16. Since the uniform von-Mises stress value is a function of μ, and μ can be explicitly defined as a function of the volume fraction, a relation between the minimum possible equivalent stress in a plate with the volume fraction is obtained, given by equation 6.15, which is plotted in figure 6.17.

$$\sigma^{VM} = \sqrt{3}\frac{\sigma_\infty}{2\mu^*} = \frac{\sqrt{3}(1-2\gamma)\sigma_\infty}{-\gamma + \sqrt{\gamma^2 + V(1-2\gamma)}}, \qquad \gamma = \frac{1}{\sqrt{3}} \tag{6.15}$$

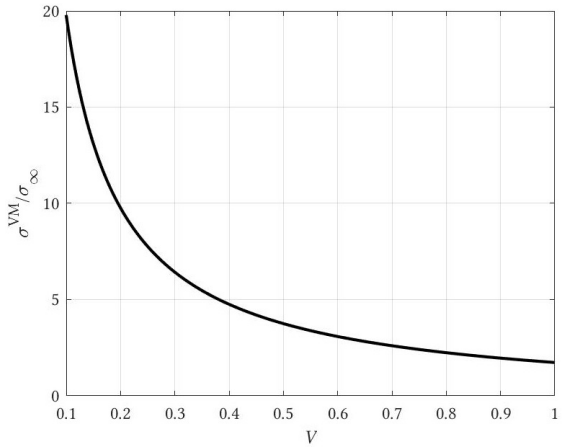

Figure 6.17: Minimum possible equivalent stress for a pure shear load as a function of the volume fraction

This result can somewhat be extended to every load where the product of the two macroscopic eigenstresses is negative. Instead of the zone (1) being a square of edge μ, it is now a rectangle of edges μ_1 and μ_2, as seen in figure 6.18.

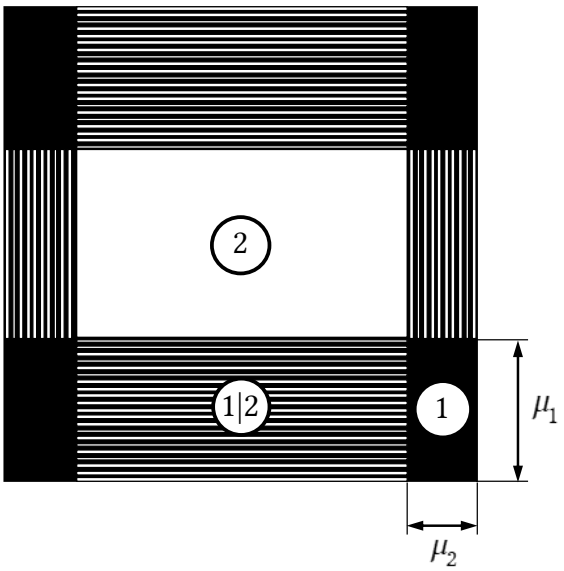

Figure 6.18: Optimal rank-2 composite material for the minimum peak equivalent when subject to a macroscopic load where $\sigma_1\sigma_2 < 0$

The ratio of the lengths μ_1 and μ_2 is equal to the ratio of the macroscopic stresses, in such a way that a pure shear stress state is attained in zone (1), as expressed in equation 6.16. By choosing $\gamma = 1/\sqrt{3}$, the stress distribution in the microstructure is the same as the one described in equation 6.10, and consequently, the equivalent stress in equation 6.12 is obtained.

$$\mu_1 = -\frac{\sigma_1}{\sigma_2}\mu_2 = m\mu_2, \qquad \mu_1, \mu_2 \in]0, 0.5[\tag{6.16}$$

Since zone (1) has edges with different lengths if $m \neq 1$, this microstructure may not be used for arbitrary values of m and V. The condition of both μ_1 and μ_2 having to be lower than 0.5 will be violated before the volume fraction reaches the unity. This can clearly be seen in figure 6.19b.

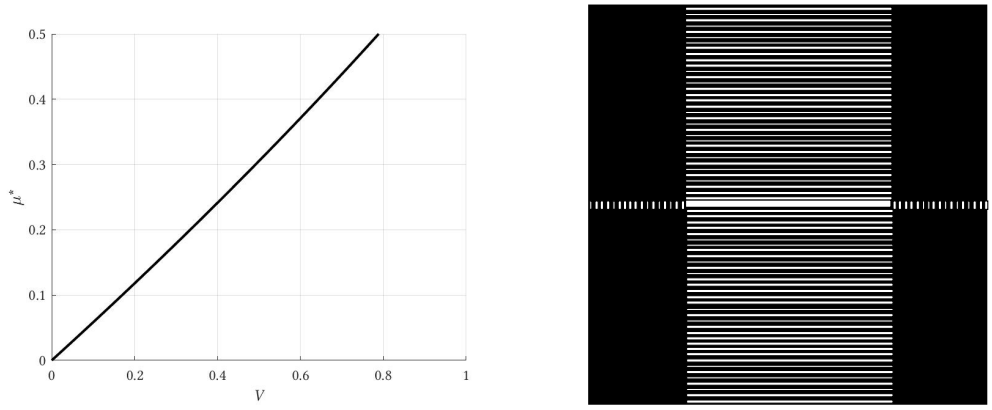

a. Parameter μ_1 as a function of V

b. Unit cell as μ_1 approaches 0.5

Figure 6.19: Optimal microstructure with the largest possible volume fraction for $m = 2$

Without loss of generality, it is assumed that $m \geq 1$ ($|\sigma_1| \geq |\sigma_2|$). The volume fraction can be defined as a function of μ_2, as shown in equation 6.17, assuming $\mu_1 = m\mu_2 < 0.5$.

$$\begin{aligned} V =& 4\mu_1\mu_2 + 2\mu_1(1-2\mu_2)\gamma + 2\mu_2(1-2\mu_1)\gamma = \\ =& 4m\mu_2^2 + 2m\mu_2(1-2\mu_2)\gamma + 2\mu_2(1-2m\mu_2)\gamma = \\ =& (4m - 8m\gamma)\mu_2^2 + \gamma(2m+2)\mu_2 \end{aligned} \tag{6.17}$$

As it is possible to see in figure 6.19a, there is a range of unattainable volume fractions when m differs from the unity. The highest obtainable volume fractions is plotted in figure 6.20, as a function of m. The curve is symmetric about $m = 1$, which was to be expected. Furthermore, the volume fraction converges to γ as the value of m goes to extreme values, since the resulting material would be composed primarily of the laminate material.

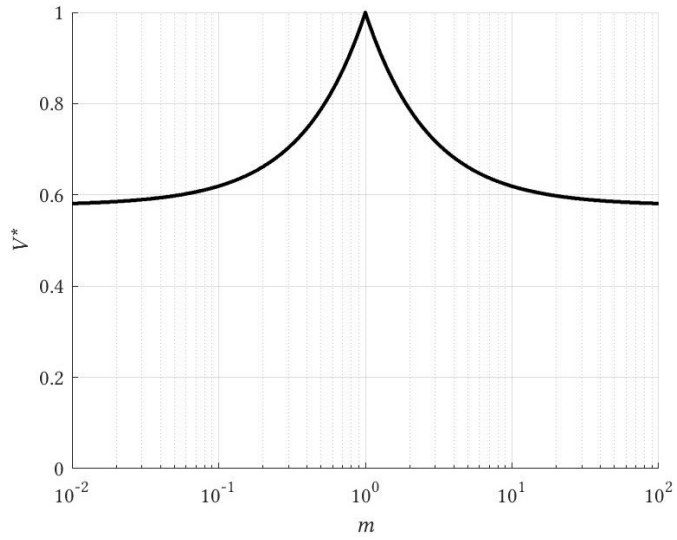

Figure 6.20: Highest possible volume fraction for the proposed optimal microstructure as a function of m

6.4.4 Summary

The results for every optimization concerning the shear load problem are displayed on figure 6.21. As would be to expect, no design is better from a peak equivalent stress viewpoint than the proposed theoretical limit using a rank-2 composite material. The variable thickness plate produced the best results, given its increased flexibility when compared to the other approaches. As for low volume fractions the shape optimization methodology managed to reduce the stress even further, only due to the fact that the mesh used in the topology problem was too coarse. If a more refined mesh was employed, the peak equivalent stress would certainly be lower.

Table 6.12: Summary of the optimal miscrostructures obtained for the shear load

V [%]	$\sigma^{VM}/\sigma_\infty$			
	Theoretical	SMSO Minimum strain energy	SMSO Minimum peak stress	Variable thickness plate Minimum peak stress
95	1.8397	_____	_____	2.0541
90	1.9590	2.7520	2.8813	2.2355
80	2.2411	3.2824	3.2775	2.5913
70	2.6024	3.9954	3.9474	3.1488
60	3.0824	4.7781	4.6101	3.7708
50	3.7527	5.7776	5.3726	4.5300
40	4.7560	7.2660	6.4245	5.9405
30	6.4259	9.9320	8.1779	8.2998
20	9.7623	14.2854	11.5946	_____
10	19.7652	31.8132	21.6176	_____

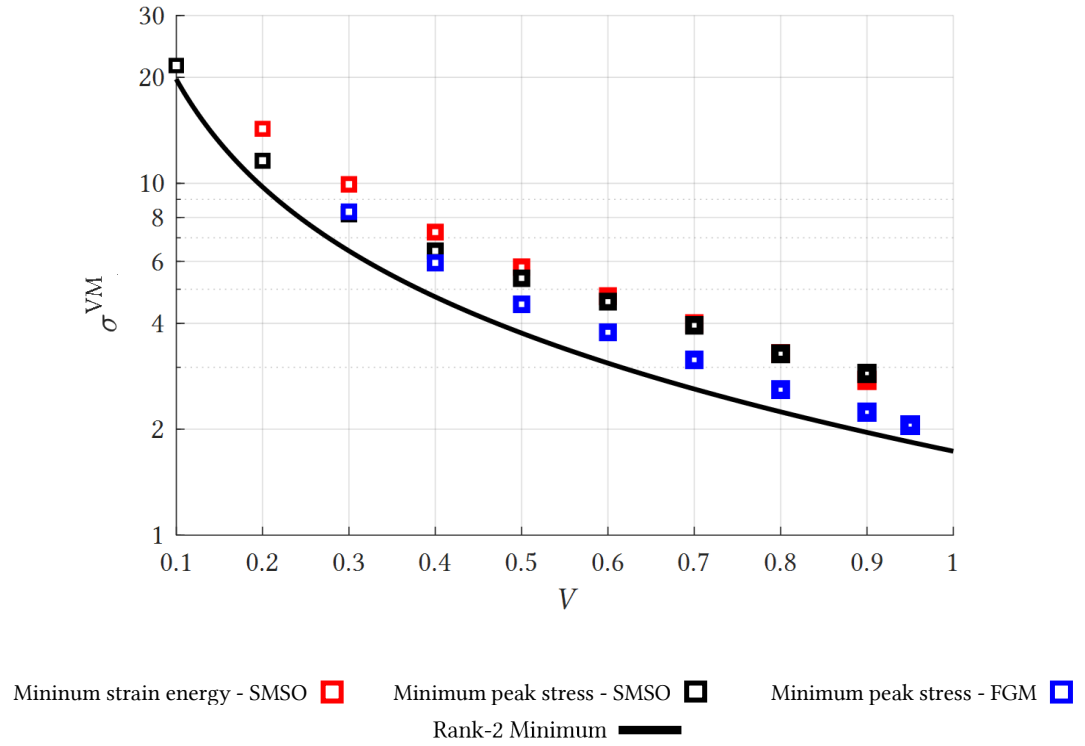

Figure 6.21: Comparison between the optimal designs and the proposed minimum peak equivalent stress attainable for the pure shear stress load

Chapter 7

Conclusions and Future Developments

In essence, the main goal of this dissertation was to find the optimal unit cell of a doubly periodic microstructure that minimizes the peak equivalent stress, for a given macroscopic load. As this is a periodic problem by nature, the asymptotic homogenization technique was employed. This both ensures accurate results and reduces the computational cost associated with the numerical model, since periodicity boundary conditions are imposed, instead of a modelling a finite number of repetitions. Throughout the dissertation, only stress macroscopic boundary conditions were considered. It is known that strain boundary conditions lead to different microstructures for the minimum peak equivalent stress problem, favouring the use of less material. Furthermore, the known theoretical results are related to the stress boundary conditions.

At first, shape optimization was used to reproduce the Vigdergauz microstructures, in their orthotropic form. The solved problem was the minimization of the maximum equivalent stress on the microsctucture, though it is equivalent to the minimization of the strain energy, or the maximization of the bulk modulus. Although this problem has a known parametric equation that defines the optimal shape of the hole, its expression makes it not easy to use in practice. Through the use of the supershape parametrization for the hydrostatic load case, and the k-tyke Gielis Formula for the biaxial one, the theoretical lowest possible stress values were replicated with success for volume fractions ranging from 10 to 90%, with the maximum stress deviation being less than 1%.

In an attempt to further reduce the stress peak in the microstructure beyond the known

theoretical bounds, an homogeneous layer of a different material is placed around the hole of the unit cell. Through having a lower Young's modulus than the regular material of the plate, the free boundary of the hole (usually with the harshest stress state on the whole unit cell) is less solicited, at the cost of the appearance of another stress peak, in the boundary between the distinct material phases.

Employing the same strategy of the single material parametrization, the shape of the soft ring of material was optimized, as well as its Young's modulus, leading to the lowest possible equivalent stress in any region of the plate. Even though the final designs are limited by the flexibility of the equations used to describe the shapes of hole and the material-material interface, great stress reductions were achieved. For the highest volume fractions (90 through 99%), the superellipse and supershape parametrizations led to the same layout, being simply a thick layer of a softer material around the hole. As the volume fraction decreases, this strategy becomes less effective. For volume fractions of 60 to 80%, she supershape parametrization is notoriously superior to its counterpart at lowering the stress peak. For volume fractions of 50% and below, the introduction of the homogeneous ring is not very effective, with only the simpler parametrization being used to prove its inefficiency.

The potential for stress reduction when subject to a biaxial load by introducing a soft layer of material around the hole is in line with the hydrostatic load case. For high volume fractions, peak equivalent stress reduction is immense when compared to the optimal single material designs. As the volume fraction decreases, so does the ability to reduce the peak stress.

Then, the behaviour of a functionally graded material in the radial direction was approximated by a finite number of soft layers around the hole. The material of each ring was optimized, as well as the shape of the interfaces between different phases. This was only employed for the 95 and 99% volume fractions, with great stress reductions being achieved, almost attaining an evenly stressed state throughout the unit cell.

However, the aforementioned method was dropped in favour of a topology optimization approach. For this particular application, it is mandatory that every non-void element fully contributes to the calculation of the volume fraction. Thus, a new volume calculation function was introduced that, while being differentiable, has a behaviour similar to a step function.

Now, instead of being limited by the number of material phases and the parametrization of their boundaries, the Young's modulus of every element of the finite element mesh itself is a design variable. This allowed for the discovery of the optimal Young's modulus field of the plate that leads to the minimization of the stress peak. The stress reductions were greater than with any other method, with the highest volume fractions almost corresponding to an equally stressed state. This approach was used for volume fractions from 99 down to 60%, where the stress reductions were no longer substantial, and the connectivity of the unit cell was becoming

hard to maintain.

As for the biaxial load case, this also resulted in a big improvement when compared to the parametrizations with one or two material phases. However, a uniform stress field could not be achieved, as was attained for the hydrostatic load. Another problematic feature of this load case is that its optimal topology cannot be correctly modelled unless a finer finite element mesh is used. by a typical topology optimization mesh, as was discussed in the main body of this document.

The pure shear load case was also approached with the use of the single material shape optimization technique, for the particular case of a unit cell with a single hole. When the sign of the two macroscopic eigenstresses differ, the optimal microstructure for the minimization of the peak equivalent stress is no longer the same as the one for the minimization of the strain energy. Both problems were solved for volume fractions of 10 through 90%, and their differences were discussed. Although the optimal microstructures are similar for the two highest volume fractions, the differences become evident as the volume fraction lowers.

The same topology optimization method was used for the shear load case. For every volume fraction, the equivalent stress distribution in the unit cell is almost uniform except for the elements nearing a hole, which is provoked by the density filtering technique. The optimal topology is a square hole in the center of the unit cell, with slots parallel to the edges of the square. This method was applied for volume fractions ranging from 30 to 95%. As the finite element mesh is quite coarse, the volume fractions of 20 and 99% could not be modelled correctly, as discretization error would be too significant.

At last, a theoretical rank-2 material was proposed as the optimal microstructure to minimize the peak stress value, by leading to an equally stressed state throughout the microstructure, under a macroscopic shear load case. This result was then extended to every load characterised by two eigenstresses whose product is negative, although not for every volume fraction. This explains the obtained results through topology optimization, as they try to approach a second rank material in a single scale discretization.

In every optimization scheme in this dissertation, the sensitivity of the objective and constraint functions was computed through the finite differentiation method. It is easy to implement, hence it allowed to explore a variety of approaches to the same problem without complications. However, progressing forward, it would be advantageous to implement an analytical method to evaluate the sensitivities.

In shape optimization, the direct differentiation method is preferred, since the number of design variables is vastly inferior to the number of constraints, as the control of the equivalent stress values is made locally, at every element. Consequently, a more flexible parametrization or finer mesh could be used, while not making the computational time of the optimization

prohibitive.

Furthermore, the computational implementation of the homogenization method could be improved. It works by applying three unit strain tests, independent of one another. If those three finite element analysis could be made simultaneously through parallel computing, the optimization process could surely be faster.

In topology optimization, the ideal would be the adjoint differentiation method. In a single material problem formulation, the number of constraints is roughly equal to the number of constraints. However, an active set constraint methodology is used, reducing the number of constraints significantly, making this one the method of choice. Furthermore, it allows for the eventual introduction of a multi-material topology optimization approach to the problem, which would at least double the number of design variables, but keep the number of constraints the same.

There are two interesting ways to go about the introduction of an additional design variable per element. One could argue that the current approach is prone to getting stuck in local minima, as one single design variable is responsible for both the topology of the element (the existence, or not, of material in that element) and its Young's modulus value. Then, one density variable would control the topology, with its value being preferentially discrete ($\rho_{0,e}$), and one density being responsible for determining the Young's modulus of the point of the domain ($\rho_{1,e}$), with values ranging from 0 to 1. This approach was recently used for the problem of a macrostructure [19]. In the particular case of the lowest possible Young's modulus corresponding to void phase, the employed interpolation law is in the form of equation 7.1, where p is the exponent the SIMP approach.

$$E_e(\mathbf{x}) = \rho_{0,e}^{p} \rho_{1,e} E^{(\max)} \tag{7.1}$$

Alternatively, a discrete material interpolation scheme could be employed, ultimately resulting in microstructure with an imposed minimum amount of void, and a distribution of two different material phases in the remainder domain. The results obtained through multi-material shape optimization in the present dissertation serve as a benchmark for the results obtained through topology optimization. In a contemporary master thesis [42], a multi-material topology optimization scheme was successfully implemented in the two-dimensional truss problem, with an interpolation law in the form of equation 7.2. The methodology can be scaled to the planar elasticity problem, unlocking the potential to obtain even better designs.

$$E_e(\mathbf{x}) = E^{(0)} + \sum_{m=1}^{n^p} \rho_{e,m}^{p} \left(E^{(m)} - E^{(0)} \right) \tag{7.2}$$

It would be interesting to explore the Vidgergauz microstructures in their isotropic form, with an hexagonal unit cell. Although this problem can be tackled with shape optimization, topology optimization is probably best suited for this application. The single material solution can be obtained, replicating the theoretical results, and a functionally graded version could be explored, in an attempt to lower the peak stress in the unit cell, as was done in this dissertation with the square-symmetric unit cell.

With having a functional multi-material topology optimization at the micro-scale, it is possible to use it in a multi-scale topology problem. By optimizing both the macro-scale of the structure and its microstructure, better structures can be achieved than in a typical macro-scale topology problem. This would be the ultimate goal of developing a method of optimizing the microstructure for a given load.

The results obtained in this dissertation have its foundations in a hypothesis that may not be verified. It is assumed that the distinct material phases are rigidly bounded, meaning the material-material interface is perfect. In practice, the material attaining its yield stress is only one of the ways a composite material can fail, with delamination being one of the most notorious failure modes. In order for the obtained microstructures to be considered as viable, this phenomenon must be studied. That being said, this fact does not interfere with the insight obtained in the results that were presented, as they clearly show the potential of the introduction of softer material phases to lower the stress peak. The same could be said about fatigue, when considering cyclic loading. High stress peaks are known to occur in the interface between two distinct material phases, which must be taken into account.

Bibliography

[1] J. Arora. *Introduction to Optimum Design*. Elsevier Science, 2004.

[2] N. Banichuk. "Optimality conditions in the problem of seeking the hole shapes in elastic bodies." In: *Journal of Applied Mathematics and Mechanics* 41.5 (1977), pp. 946–951. DOI: 10.1016/0021-8928(77)90179-4.

[3] O. Bauchau and J. Craig. *Structural Analysis: With Applications to Aerospace Structures*. Solid Mechanics and Its Applications. Springer Netherlands, 2009.

[4] M. P. Bendsøe and O. Sigmund. "Material interpolation schemes in topology optimization." In: *Archive of Applied Mechanics* 69.9 (1999), pp. 635–654. DOI: 10.1007/s004190050248.

[5] M. P. Bendsoe and O. Sigmund. *Topology Optimization: Theory, Methods and Applications*. en. Springer, Feb. 2004.

[6] V. Braibant and C. Fleury. "Shape optimal design using B-splines." In: *Computer Methods in Applied Mechanics and Engineering* 44.3 (1984), pp. 247 –267. DOI: https://doi.org/10.1016/0045-7825(84)90132-4.

[7] T. Bruns and D. Tortorelli. "Topology optimization of non-linear elastic structures and compliant mechanisms." English (US). In: *Computer Methods in Applied Mechanics and Engineering* 190.26-27 (Mar. 2001), pp. 3443–3459. DOI: 10.1016/S0045-7825(00)00278-4.

[8] J. Cadman, S. Zhou, Y. Chen, and Q. Li. "On design of multi-functional microstructural materials." In: *Journal of Materials Science* 48 (July 2013), pp. 51–66. DOI: 10.1007/s10853-012-6643-4.

[9] C. Charalambous and J. W. Bandler. "Non-linear minimax optimization as a sequence of least pth optimization with finite values of p." In: *International Journal of Systems Science* 7.4 (1976), pp. 377–391. DOI: 10.1080/00207727608941924.

[10] R. Chen. "Solution of minimax problems using equivalent differentiable functions." In: *Computers and Mathematics with Applications* 11.12 (1985), pp. 1165 –1169. DOI: https://doi.org/10.1016/0898-1221(85)90104-X.

[11] G. Cherepanov. "Inverse problems of the plane theory of elasticity." In: *Journal of Applied Mathematics and Mechanics* 38.6 (1974), pp. 915–931. DOI: 10.1016/0021-8928(75)90085-4.

[12] A. Cherkaev, K. Lurie, and G. Milton. "Invariant Properties of the Stress in Plane Elasticity and Equivalence Classes of Composites." In: *Proceedings of The Royal Society A: Mathematical, Physical and Engineering Sciences* 438 (Sept. 1992), pp. 519–529. DOI: 10.1098/rspa.1992.0123.

[13] A. Cherkaev and L. Gibiansky. "Coupled estimates for the bulk and shear moduli of a two-dimensional isotropic elastic composite." In: *Journal of the Mechanics and Physics of Solids* 41.5 (1993), pp. 937 –980. DOI: https://doi.org/10.1016/0022-5096(93)90006-2.

[14] A. Cherkaev, Y. Grabovsky, A. Movchan, and S. Serkov. "The cavity of the optimal shape under the shear stresses." In: *International Journal of Solids and Structures* 35.33 (1998), pp. 4391 –4410. DOI: https://doi.org/10.1016/S0020-7683(97)00214-X.

[15] K. K. Choi and N.-H. Kim. *Structural sensitivity analysis and optimization 1: linear systems.* Springer Science & Business Media, 2006.

[16] P. Coelho. "Tópicos avançados em mecânica estrutural." In: (2018).

[17] P. G. Coelho, J. M. Guedes, and J. B. Cardoso. "Topology optimization of cellular materials with periodic microstructure under stress constraints." In: *Structural and Multidisciplinary Optimization* 59 (Sept. 2018), pp. 1–13. DOI: 10.1007/s00158-018-2089-x.

[18] M. Collet, L. Noël, M. Bruggi, and P. Duysinx. "Topology optimization for microstructural design under stress constraints." In: *Structural and Multidisciplinary Optimization* 58.6 (2018), pp. 2677–2695. DOI: 10.1007/s00158-018-2045-9.

[19] C. Conlan-Smith and K. James. "A stress-based topology optimization method for heterogeneous structures." English. In: *Structural and Multidisciplinary Optimization* 60.1 (2019), pp. 167–183. DOI: 10.1007/s00158-019-02207-9.

[20] Y. Ding. "Shape optimization of structures: a literature survey." In: *Computers & Structures* 24.6 (1986), pp. 985 –1004. DOI: https://doi.org/10.1016/0045-7949(86)90307-X.

[21] P. Duysinx and M. P. Bendsøe. "Topology optimization of continuum structures with local stress constraints." In: *International Journal for Numerical Methods in Engineering* 43.8 (1998), pp. 1453–1478. DOI: 10.1002/(SICI)1097-0207(19981230)43:8<1453::AID-NME480>3.0.CO;2-2.

[22] G. A. Francfort and F. Murat. "Homogenization and optimal bounds in linear elasticity." In: *Archive for Rational Mechanics and Analysis* 94.4 (1986), pp. 307–334. DOI: 10.1007/BF00280908.

[23] J. Gielis. "A generic geometric transformation that unifies a wide range of natural and abstract shapes." In: *American Journal of Botany* 90.3 (2003), pp. 333–338. DOI: 10.3732/ajb.90.3.333.

[24] J. Gielis. *The Geometrical Beauty of Plants*. 2017. DOI: 10.2991/978-94-6239-151-2.

[25] Y. Grabovsky and R. V. Kohn. "Microstructures minimizing the energy of a two phase elastic composite in two space dimensions. II: The vigdergauz microstructure." In: *Journal of the Mechanics and Physics of Solids* 43.6 (1995), pp. 949 –972. DOI: https://doi.org/10.1016/0022-5096(95)00017-D.

[26] J. Guedes and N. Kikuchi. "Preprocessing and postprocessing for materials based on the homogenization method with adaptive finite element methods." In: *Computer Methods in Applied Mechanics and Engineering* 83.2 (1990), pp. 143 –198. DOI: https://doi.org/10.1016/0045-7825(90)90148-F.

[27] R. T. Haftka and Z. Gürdal. *Elements of Structural Optimization*. 1992. DOI: 10.1007/978-94-011-2550-5.

[28] Z. Hashin and S. Shtrikman. "A variational approach to the theory of the elastic behaviour of multiphase materials." In: *Journal of the Mechanics and Physics of Solids* 11.2 (1963), pp. 127–140. DOI: 10.1016/0022-5096(63)90060-7.

[29] Z. Hashin and S. Shtrikman. "A variational approach to the theory of the elastic behaviour of multiphase materials." In: *Journal of the Mechanics and Physics of Solids* 11.2 (1963), pp. 127 –140. DOI: https://doi.org/10.1016/0022-5096(63)90060-7.

[30] R. Hill. "Theory of mechanical properties of fibre-strengthened materials: I. Elastic behaviour." In: *Journal of the Mechanics and Physics of Solids* 12.4 (1964), pp. 199 –212. DOI: https://doi.org/10.1016/0022-5096(64)90019-5.

[31] E. G. Kirsch. "Die Theorie der Elastizität und die Bedürfnisse der Festigkeitslehre." In: (1898).

[32] R. V. Kohn and G. Strang. "Optimal design and relaxation of variational problems, II." In: *Communications on Pure and Applied Mathematics* 39.2 (1986), pp. 139–182. DOI: 10.1002/cpa.3160390202. eprint: https://onlinelibrary.wiley.com/doi/pdf/10.1002/cpa.3160390202.

[33] G. Kreisselmeier and R. Steinhauser. "Systematic Control Design by Optimizing a Vector Performance Index." In: *IFAC Proceedings Volumes* 12.7 (1979). IFAC Symposium on computer Aided Design of Control Systems, Zurich, Switzerland, 29-31 August, pp. 113 –117. DOI: https://doi.org/10.1016/S1474-6670(17)65584-8.

[34] R. Lipton. "Design of functionally graded composite structures in the presence of stress constraints." In: 2002.

[35] K. A. Lurie and A. V. Cherkaev. "Exact estimates of the conductivity of a binary mixture of isotropic materials." In: *Proceedings of the Royal Society of Edinburgh: Section A Mathematics* 104.1-2 (1986), 21–38. DOI: 10.1017/S0308210500019041.

[36] G. Milton and A. Cherkaev. "Which Elasticity Tensors are Realizable?" In: *Journal of Engineering Materials and Technology-transactions of The Asme - J ENG MATER TECHNOL* 117 (Oct. 1995). DOI: 10.1115/1.2804743.

[37] M. Mohammadi, J. R. Dryden, and L. Jiang. "Stress concentration around a hole in a radially inhomogeneous plate." In: *International Journal of Solids and Structures* 48.3 (2011), pp. 483 –491. DOI: https://doi.org/10.1016/j.ijsolstr.2010.10.013.

[38] L. Noël and P. Duysinx. "Shape optimization of microstructural designs subject to local stress constraints within an XFEM-level set framework." In: *Structural and Multidisciplinary Optimization* 55.6 (2017), pp. 2323–2338. DOI: 10.1007/s00158-016-1642-8.

[39] M. M. J. Opgenoord and K. E. Willcox. "Design for additive manufacturing: cellular structures in early-stage aerospace design." In: *Structural and Multidisciplinary Optimization* 60.2 (2019), pp. 411–428. DOI: 10.1007/s00158-019-02305-8.

[40] P. Pedersen. "On optimal shapes in materials and structures." In: *Structural and Multidisciplinary Optimization* 19.3 (2000), pp. 169–182. DOI: 10.1007/s001580050100.

[41] W. Prager. "Optimality criteria in structural design." In: *Proceedings of the National Academy of Sciences* 61.3 (1968). DOI: 10.1073/PNAS.61.3.794.

[42] T. Pratas. "Optimização topológica multimaterial de estruturas reticuladas com constrangimentos de tensão." In: (2019).

[43] E. Sánchez-Palencia. *Non-homogeneous media and vibration theory.* Lecture notes in physics. Springer-Verlag, 1980.

[44] R. Sburlati, S. Atashipour, and S. Atashipour. "Reduction of the stress concentration factor in a homogeneous panel with hole by using a functionally graded layer." In: *Composites Part B: Engineering* 61 (2014), pp. 99 –109. DOI: https://doi.org/10.1016/j.compositesb.2014.01.036.

[45] R. Sburlati. "Stress concentration factor due to a functionally graded ring around a hole in an isotropic plate." In: *International Journal of Solids and Structures* 50.22 (2013), pp. 3649 –3658. DOI: https://doi.org/10.1016/j.ijsolstr.2013.07.007.

[46] O. Sigmund. "A new class of extremal composites." In: *Journal of the Mechanics and Physics of Solids* 48.2 (2000), pp. 397 –428. DOI: https://doi.org/10.1016/S0022-5096(99)00034-4.

[47] O. Sigmund. "Morphology-based black and white filters for topology optimization." In: *Structural and Multidisciplinary Optimization* 33.4 (2007), pp. 401–424. DOI: 10.1007/s00158-006-0087-x.

[48] K. Svanberg. "The method of moving asymptotes—a new method for structural optimization." In: *International Journal for Numerical Methods in Engineering* 24.2 (1987), pp. 359–373. DOI: 10.1002/nme.1620240207. eprint: https://onlinelibrary.wiley.com/doi/pdf/10.1002/nme.1620240207.

[49] *Theory of elasticity*. Engineering societies monographs. McGraw-Hill, 1987.

[50] S. Timoshenko and J. N. Goodier. *Theory of Liear Elasticity*. McGraw-Hill, 1970.

[51] S. Vigdergauz. "Two-Dimensional Grained Composites of Extreme Rigidity." In: *Journal of Applied Mechanics* 61.2 (June 1994), pp. 390–394. DOI: 10.1115/1.2901456. eprint: https://asmedigitalcollection.asme.org/appliedmechanics/article-pdf/61/2/390/4755152/390_1.pdf.

[52] S. Vigdergauz. "Energy-minimizing inclusions in a planar elastic structure with macroisotropy." In: *Structural optimization* 17.2 (1999), pp. 104–112. DOI: 10.1007/BF01195935.

[53] S. Vigdergauz and A. Cherkayev. "A hole in a plate, optimal for its biaxial extension - compression." In: *Journal of Applied Mathematics and Mechanics* 50.3 (1986), pp. 401–404. DOI: 10.1016/0021-8928(86)90141-3.

[54] S. Vigdergauz. "The effective properties of a perforated elastic plate Numerical optimization by genetic algorithm." In: *International Journal of Solids and Structures* 38 (Nov. 2001), pp. 8593–8616. DOI: 10.1016/S0020-7683(01)00189-5.

[55] S. Vigdergauz and A. Cherkaev. "A hole in a plate, optimal for its biaxial extension - compression." In: *Journal of Applied Mathematics and Mechanics* 50 (Dec. 1986), pp. 401–404. DOI: 10.1016/0021-8928(86)90141-3.

[56] Q. Yang and C.-F. Gao. "Reduction of the stress concentration around an elliptic hole by using a functionally graded layer." In: *Acta Mechanica* 227 (May 2016). DOI: 10.1007/s00707-016-1620-7.

[57] Q. Yang, C. Gao, and W. Chen. "Stress concentration in a finite functionally graded material plate." In: *Science China Physics, Mechanics and Astronomy* 55.7 (2012), pp. 1263–1271. DOI: 10.1007/s11433-012-4774-x.

[58] C. Zheng, X. Li, and C. Mi. "Reducing stress concentrations in unidirectionally tensioned thick-walled spheres through embedding a functionally graded reinforcement." In: *International Journal of Mechanical Sciences* 152 (Mar. 2019). DOI: 10.1016/j.ijmecsci.2018.12.055.

Appendix A

Optimal Designs - Hydrostatic Load

A.1 SMSO - Supershape Parametrization

Table A.1: Optimal designs for the minimization of the maximum stress for the $\langle\sigma_1\rangle = \langle\sigma_2\rangle$ macroscopic load – Single Material Shape Optimization using the supershape parametrization – Part 1

V [%]	$\sigma^{Theo.}_{Max}$	E/E_{Max}	$\sigma^{VM}/\sigma_\infty$	w [J/m^3]	$\sigma^{VM}_{Max}/\sigma_\infty$	δ [%]	Δ [%]
90	2.2222	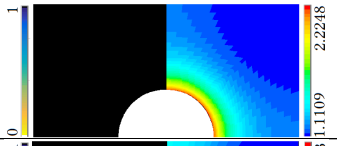		922.1664	2.2248	0.1141	0.7779
80	2.5000	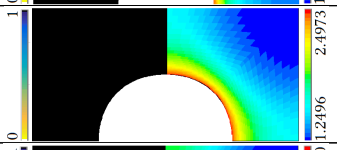		1199.833	2.4973	0.1088	0.3210
70	2.8571	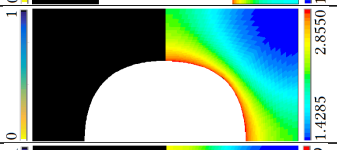		1556.963	2.8550	0.0738	0.4323
60	3.3333	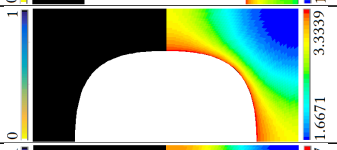		2033.154	3.3339	0.0176	0.3589
50	4.0000	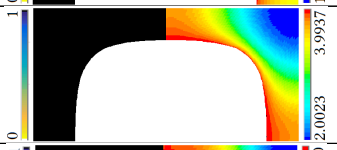		2699.821	3.9937	0.1565	0.1055
40	5.0000	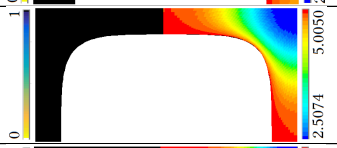		3699.764	5.0050	0.1005	0.3665
30	6.6666			5366.143	6.6776	0.1641	0.3381
20	10.000			8698.774	10.023	0.2686	0.6923
10	20.000	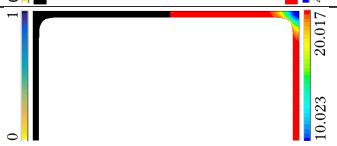		18685.01	20.017	0.0870	0.7098

Table A.2: Optimal designs for the minimization of the maximum stress for the $\langle\sigma_1\rangle = \langle\sigma_2\rangle$ macroscopic load – Single Material Shape Optimization using the supershape parametrization – Part 2

V [%]	Design Variables	$\sigma^{VM}(\theta)\Big\|_\Gamma/\sigma_\infty$	$10^9 * C^H$	$E^H_{11}(\theta)$
90	N_1=4.67075 N_2=2.10110 b_1=0.6e-3	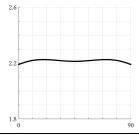	$\begin{bmatrix} 1.303 & -0.383 & 0 \\ -0.383 & 1.303 & 0 \\ 0 & 0 & 0.914 \end{bmatrix}$	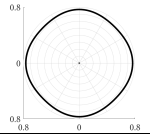
80	N_1=12.5429 N_2=2.98670 b_1=0.3e-5	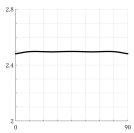	$\begin{bmatrix} 1.629 & -0.429 & 0 \\ -0.429 & 1.629 & 0 \\ 0 & 0 & 1.384 \end{bmatrix}$	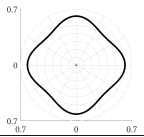
70	N_1=7.03905 N_2=3.18566 b_1=0.2e-2	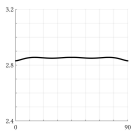	$\begin{bmatrix} 2.011 & -0.454 & 0 \\ -0.454 & 2.011 & 0 \\ 0 & 0 & 2.281 \end{bmatrix}$	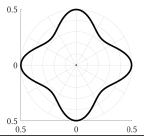
60	N_1=5.29320 N_2=3.52741 b_1=0.177e-1	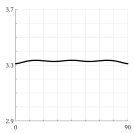	$\begin{bmatrix} 2.496 & -0.463 & 0 \\ -0.463 & 2.496 & 0 \\ 0 & 0 & 4.167 \end{bmatrix}$	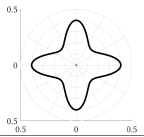
50	N_1=4.89035 N_2=4.09792 b_1=0.45e-1	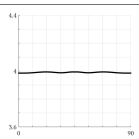	$\begin{bmatrix} 3.165 & -0.465 & 0 \\ -0.465 & 3.165 & 0 \\ 0 & 0 & 8.654 \end{bmatrix}$	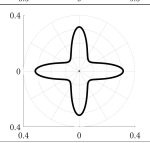
40	N_1=5.31776 N_2=5.05509 b_1=0.7e-1	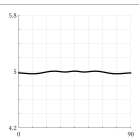	$\begin{bmatrix} 4.165 & -0.465 & 0 \\ -0.465 & 4.165 & 0 \\ 0 & 0 & 21.18 \end{bmatrix}$	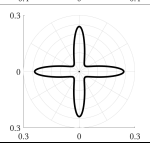
30	N_1=6.96440 N_2=6.89895 b_1=0.83e-1	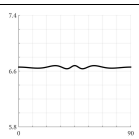	$\begin{bmatrix} 5.831 & -0.465 & 0 \\ -0.465 & 5.831 & 0 \\ 0 & 0 & 64.44 \end{bmatrix}$	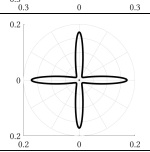
20	N_1=10.8382 N_2=10.8381 b_1=0.9e-1	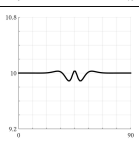	$\begin{bmatrix} 9.162 & -0.464 & 0 \\ -0.464 & 9.162 & 0 \\ 0 & 0 & 281.6 \end{bmatrix}$	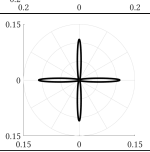
10	N_1=23.9711 N_2=23.9710 b_1=0.5e-01	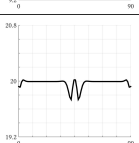	$\begin{bmatrix} 19.15 & -0.461 & 0 \\ -0.461 & 19.15 & 0 \\ 0 & 0 & 2289 \end{bmatrix}$	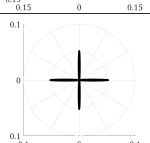

A.2 MMSO - Two Material Phases - Superellipse Parametrization

Table A.3: Optimal designs for the minimization of the maximum stress for the $\langle\sigma_1\rangle = \langle\sigma_2\rangle$ macroscopic load – Multi-material Shape Optimization using the superellipse parametrization – Part 1

V [%]	$\sigma_{Max}^{Theo.}$	E/E_{Max}	$\sigma^{VM}/\sigma_\infty$	w $[J/m^3]$	$\sigma_{Max}^{VM}/\sigma_\infty$	Reduction [%]
99	2.0202	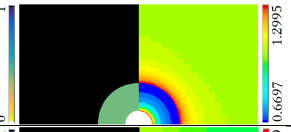		785.3271	1.2995	35.67
95	2.1053	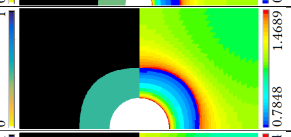		934.7283	1.4689	30.23
90	2.2222	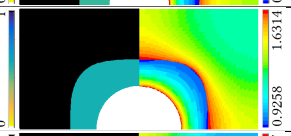		1093.5040	1.6314	26.59
80	2.5000	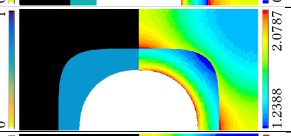		1375.4919	2.0787	16.85
70	2.8571	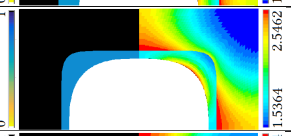		1687.5494	2.5462	10.88
60	3.3333	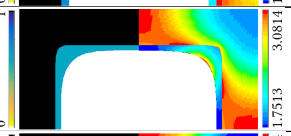		2244.9102	3.0814	7.56
50	4.0000	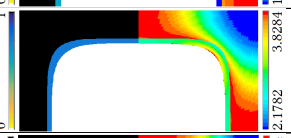		2840.2338	3.8284	4.29
40	5.0000			3867.6853	4.8224	3.55
30	6.6666			5406.0656	6.6234	0.65
20	10.000			8812.7163	10.045	-0.45

Table A.4: Optimal designs for the minimization of the maximum stress for the $\langle\sigma_1\rangle = \langle\sigma_2\rangle$ macroscopic load – Multi-material Shape Optimization using the superellipse parametrization – Part 2

V [%]	Design Variables	$\sigma^{VM}(\theta)\Big\|_{\Gamma_1,\Gamma_2}/\sigma_\infty$	$10^9 * C^H$	$E^H_{11}(\theta)$
99	$N_1 = 2.00052$ $N_2 = 2.05673$ $b_1 = 0.86797*$ $b_2 = 1.14935*$ $1.3e-02$ $3.0e-02$ $E_1 = 0.41964E_2$	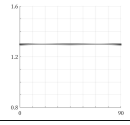	$\begin{bmatrix} 1.120 & -0.334 & 0 \\ -0.334 & 1.120 & 0 \\ 0 & 0 & 0.737 \end{bmatrix}$	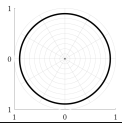
95	$N_1 = 2.01137$ $N_2 = 2.43212$ $b_1 = 0.96946*$ $b_2 = 1.11974*$ $2.6e-02$ $4.5e-02$ $E_1 = 0.76362E_2$	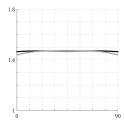	$\begin{bmatrix} 1.312 & -0.377 & 0 \\ -0.377 & 1.312 & 0 \\ 0 & 0 & 0.910 \end{bmatrix}$	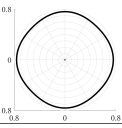
90	$N_1 = 2.04324$ $N_2 = 3.42768$ $b_1 = 0.88847*$ $b_2 = 0.96429*$ $4.0e-02$ $6.0e-02$ $E_1 = 0.54827E_2$	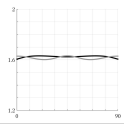	$\begin{bmatrix} 1.502 & -0.408 & 0 \\ -0.408 & 1.502 & 0 \\ 0 & 0 & 1.128 \end{bmatrix}$	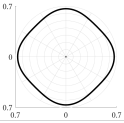
80	$N_1 = 2.21519$ $N_2 = 4.59164$ $b_1 = 0.99091*$ $b_2 = 0.96315*$ $5.0e-02$ $7.0e-02$ $E_1 = 0.68315E_2$	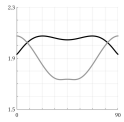	$\begin{bmatrix} 1.817 & -0.442 & 0 \\ -0.442 & 1.817 & 0 \\ 0 & 0 & 1.656 \end{bmatrix}$	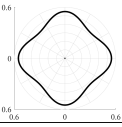
70	$N_1 = 2.90673$ $N_2 = 6.35563$ $b_1 = 0.94319*$ $b_2 = 0.86854*$ $5.0e-02$ $7.0e-02$ $E_1 = 0.71540E_2$	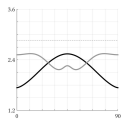	$\begin{bmatrix} 2.130 & -0.442 & 0 \\ -0.442 & 2.130 & 0 \\ 0 & 0 & 2.730 \end{bmatrix}$	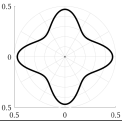
60	$N_1 = 4.56454$ $N_2 = 16.3396$ $b_1 = 0.93114*$ $b_2 = 0.89752*$ $7.0e-02$ $7.8e-02$ $E_1 = 0.60761E_2$	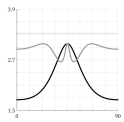	$\begin{bmatrix} 2.681 & -0.435 & 0 \\ -0.435 & 2.681 & 0 \\ 0 & 0 & 5.762 \end{bmatrix}$	
50	$N_1 = 4.94789$ $N_2 = 5.82346$ $b_1 = 0.96778*$ $b_2 = 0.90565*$ $7.5e-02$ $8.5e-02$ $E_1 = 0.76190E_2$	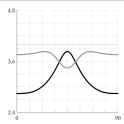	$\begin{bmatrix} 3.288 & -0.447 & 0 \\ -0.447 & 3.288 & 0 \\ 0 & 0 & 10.70 \end{bmatrix}$	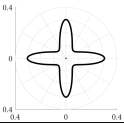
40	$N_1 = 7.09504$ $N_2 = 33.2324$ $b_1 = 0.95764*$ $b_2 = 0.88715*$ $8.2e-02$ $9.0e-02$ $E_1 = 0.68406E_2$	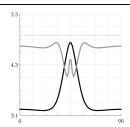	$\begin{bmatrix} 4.309 & -0.441 & 0 \\ -0.441 & 4.309 & 0 \\ 0 & 0 & 27.02 \end{bmatrix}$	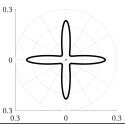
30	$N_1 = 7.35897$ $N_2 = 10.02563$ $b_1 = 0.98537*$ $b_2 = 0.93296*$ $8.6e-02$ $9.2e-02$ $E_1 = 0.92798E_2$	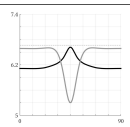	$\begin{bmatrix} 5.869 & -0.460 & 0 \\ -0.460 & 5.869 & 0 \\ 0 & 0 & 67.64 \end{bmatrix}$	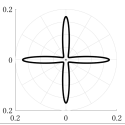
20	$N_1 = 11.6417$ $N_2 = 25.0129$ $b_1 = 0.97797*$ $b_2 = 0.94764*$ $9.2e-02$ $9.6e-02$ $E_1 = 0.93165E_2$	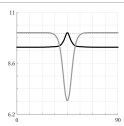	$\begin{bmatrix} 9.277 & -0.459 & 0 \\ -0.459 & 9.277 & 0 \\ 0 & 0 & 296.0 \end{bmatrix}$	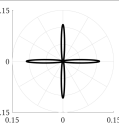

A.3 MMSO - Two Material Phases - Supershape Parametrization

Table A.5: Optimal designs for the minimization of the maximum stress for the $\langle\sigma_1\rangle = \langle\sigma_2\rangle$ macroscopic load – Multi-material Shape Optimization using the supershape parametrization – Part 1

V [%]	$\sigma_{Max}^{Theo.}$	E/E_{Max}	$\sigma^{VM}/\sigma_\infty$	w $[J/m^3]$	$\sigma_{Max}^{VM}/\sigma_\infty$	Reduction [%]
99	2.0202	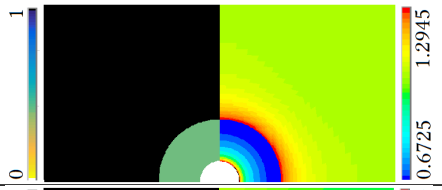		787.2281	1.2945	35.92
95	2.1053	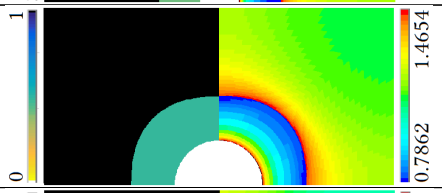		934.1646	1.4654	30.39
90	2.2222	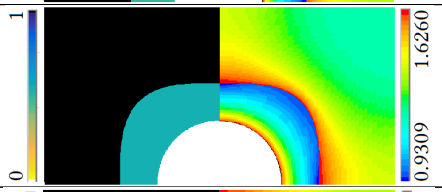		1085.2200	1.6260	26.82
80	2.5000	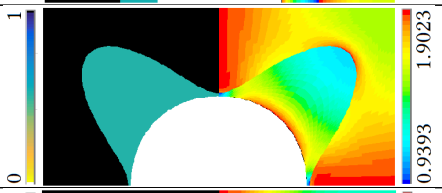		1544.4247	1.9023	23.91
70	2.8571	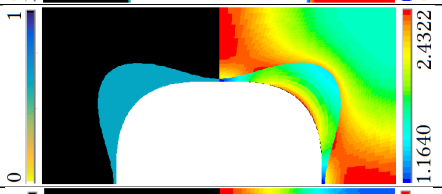		1749.9238	2.4322	14.87
60	3.3333	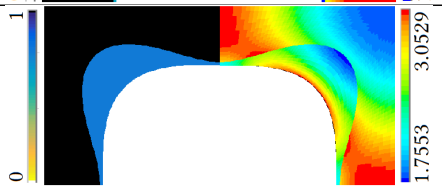		2205.4739	3.0529	8.41

Table A.6: Optimal designs for the minimization of the maximum stress for the $\langle\sigma_1\rangle = \langle\sigma_2\rangle$ macroscopic load – Multi-material Shape Optimization using the supershape parametrization – Part 2

V [%]	Design Variables	$\sigma^{VM}(\theta)\Big\|_{\Gamma_1,\Gamma_2}/\sigma_\infty$	$10^9 * C^H$	$E^H_{11}(\theta)$
99	$N_{11} = 3.50293$ $N_{12} = 5.07551$ $N_{21} = 2.00100$ $N_{22} = 2.15735$ $b_1 = 0.35674*$ $b_2 = 0.24930*$ $1.04509e-03$ $1.41945e-03$ $E_1 = 0.42115E_2$	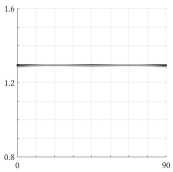	$\begin{bmatrix} 1.122 & -0.335 & 0 \\ -0.335 & 1.122 & 0 \\ 0 & 0 & 0.739 \end{bmatrix}$	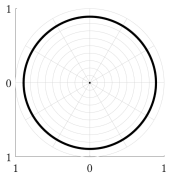
95	$N_{11} = 2.00872$ $N_{12} = 2.42953$ $N_{21} = 2.03745$ $N_{22} = 2.43984$ $b_1 = 0.93926*$ $b_2 = 1.01937*$ $3.0e-02$ $5.0e-02$ $E_1 = 0.49712E_2$	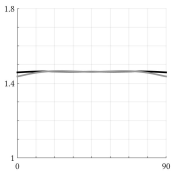	$\begin{bmatrix} 1.311 & -0.377 & 0 \\ -0.377 & 1.311 & 0 \\ 0 & 0 & 0.909 \end{bmatrix}$	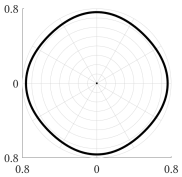
90	$N_{11} = 2.00872$ $N_{12} = 3.08629$ $N_{21} = 2.03745$ $N_{22} = 3.26085$ $b_1 = 0.92942*$ $b_2 = 1.11337*$ $4.0e-02$ $6.0e-02$ $E_1 = 0.55280E_2$	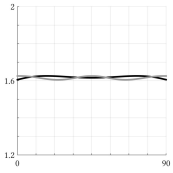	$\begin{bmatrix} 1.492 & -0.407 & 0 \\ -0.407 & 1.492 & 0 \\ 0 & 0 & 1.116 \end{bmatrix}$	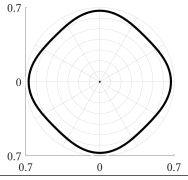
80	$N_{11} = 2.06626$ $N_{12} = 37.8291$ $N_{21} = 2.13054$ $N_{22} = 33.4730$ $b_1 = 0.59936*$ $b_2 = 0.76616*$ $1.0e-01$ $3.0e-01$ $E_1 = 0.0.51146E_2$	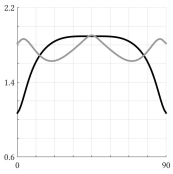	$\begin{bmatrix} 2.041 & -0.497 & 0 \\ -0.497 & 2.041 & 0 \\ 0 & 0 & 1.879 \end{bmatrix}$	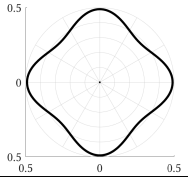
70	$N_{11} = 2.29124$ $N_{12} = 37.8291$ $N_{21} = 2.82609$ $N_{22} = 33.4730$ $b_1 = 0.99346*$ $b_2 = 1.08432*$ $1.0e-01$ $8.34e-02$ $E_1 = 0.60395E_2$	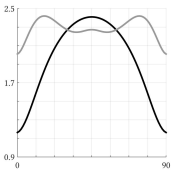	$\begin{bmatrix} 2.190 & -0.440 & 0 \\ -0.440 & 2.190 & 0 \\ 0 & 0 & 2.973 \end{bmatrix}$	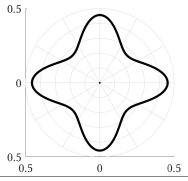
60	$N_{11} = 3.01247$ $N_{12} = 1.36192$ $N_{21} = 3.21320$ $N_{22} = 3.53546$ $b_1 = 1.12583*$ $b_2 = 1.07905*$ $7.0e-02$ $3.3e-01$ $E_1 = 0.76362E_2$	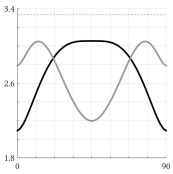	$\begin{bmatrix} 2.667 & -0.461 & 0 \\ -0.461 & 2.667 & 0 \\ 0 & 0 & 5.046 \end{bmatrix}$	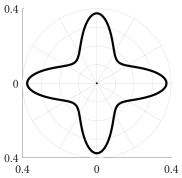

A.4 Variable Thickness Plate Approach

Table A.7: Optimal designs for the minimization of the maximum stress for the $\langle\sigma_1\rangle = \langle\sigma_2\rangle$ macroscopic load – Variable thickness plate approach – Part 1

V [%]	$\sigma_{Max}^{Theo.}$	E/E_{Max}	$\sigma^{VM}/\sigma_\infty$	w $[J/m^3]$	$\sigma_{Max}^{VM}/\sigma_\infty$	Reduction [%]
99	2.0202	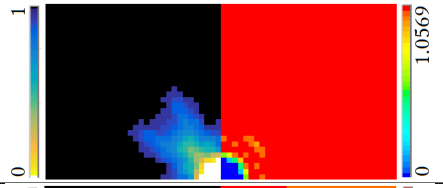		788.120	1.0569	47.64
95	2.1053	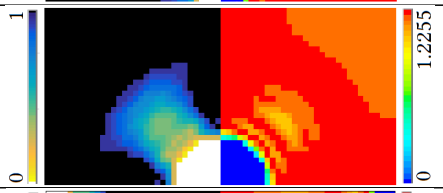		973.504	1.2255	41.79
90	2.2222	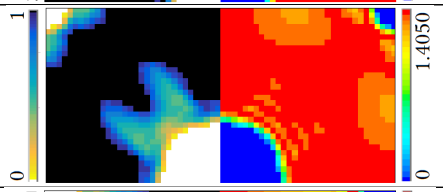		1183.05	1.4050	36.78
80	2.5000	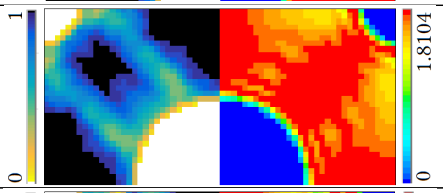		1771.12	1.8104	27.58
70	2.8571	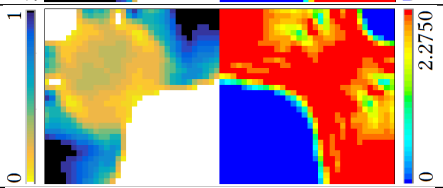		5541.98	2.2750	20.38
60	3.3333	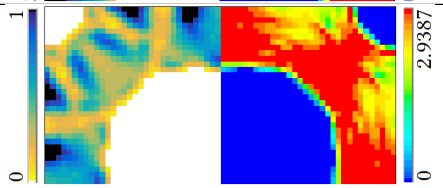		5881.19	2.9387	11.84

Table A.8: Optimal designs for the minimization of the maximum stress for the $\langle\sigma_1\rangle = \langle\sigma_2\rangle$ macroscopic load – Variable thickness plate approach – Part 2

V [%]	Initial Design	$10^9 * C^H$	$E^H_{11}(\theta)$	Variable Thickness Plate
99	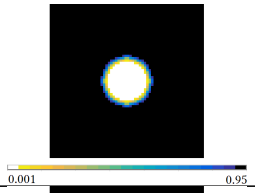	$\begin{bmatrix} 1.121 & -0.333 & 0 \\ -0.333 & 1.121 & 0 \\ 0 & 0 & 0.737 \end{bmatrix}$	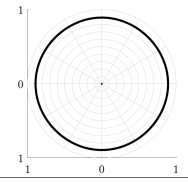	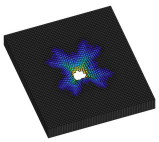
95	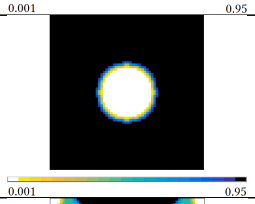	$\begin{bmatrix} 1.356 & -0.383 & 0 \\ -0.383 & 1.356 & 0 \\ 0 & 0 & 0.951 \end{bmatrix}$	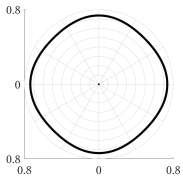	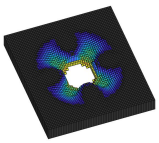
90	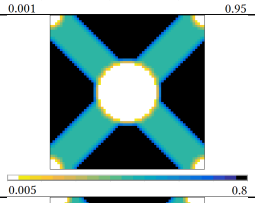	$\begin{bmatrix} 1.685 & -0.502 & 0 \\ -0.502 & 1.685 & 0 \\ 0 & 0 & 1.173 \end{bmatrix}$	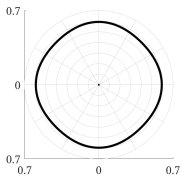	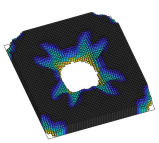
80	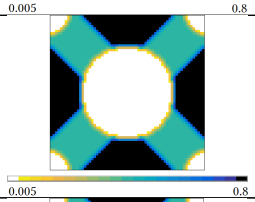	$\begin{bmatrix} 2.712 & -0.941 & 0 \\ -0.941 & 2.712 & 0 \\ 0 & 0 & 1.822 \end{bmatrix}$	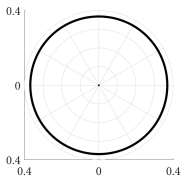	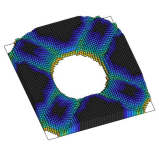
70	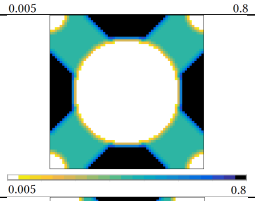	$\begin{bmatrix} 8.358 & -2.816 & 0 \\ -2.816 & 5.358 & 0 \\ 0 & 0 & 7.815 \end{bmatrix}$	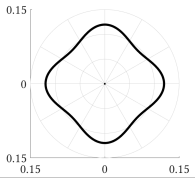	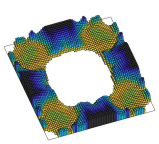
60	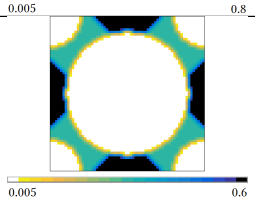	$\begin{bmatrix} 9.268 & -3.386 & 0 \\ -3.386 & 9.268 & 0 \\ 0 & 0 & 12.30 \end{bmatrix}$	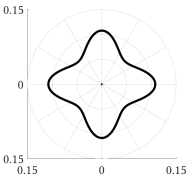	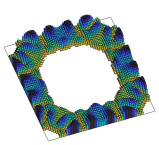

Appendix B

Optimal Designs - Biaxial Load

B.1 SMSO - k-Type Gielis Formula

Table B.1: Optimal designs for the minimization of the maximum stress for the $\langle\sigma_1\rangle = 2\langle\sigma_2\rangle$ macroscopic load – Single material Shape Optimization using the k-type Gielis Formula parametrization – Part 1

V [%]	$\sigma_{Max}^{Theo.}$	E/E_{Max}	$\sigma^{VM}/\sigma_\infty$	w [J/m^3]	$\sigma_{Max}^{VM}/\sigma_\infty$	δ [%]	Δ [%]
90	2.2222	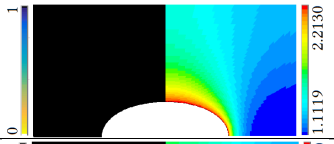		1065.8616	2.2130	0.4170	0.0543
80	2.5000	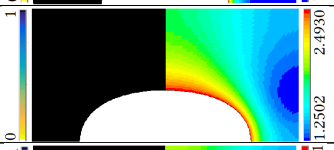		1343.1715	2.4930	0.2794	0.1374
70	2.8571	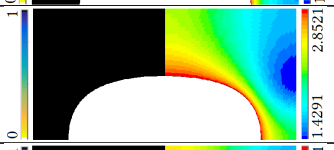		1700.1294	2.8521	0.1781	0.3616
60	3.3333	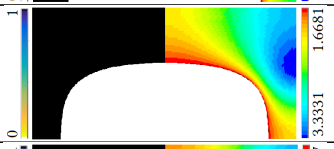		2176.9168	3.3331	0.0064	0.4529
50	4.0000	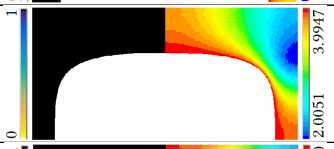		2841.6323	3.9947	0.1315	0.9288
40	5.0000	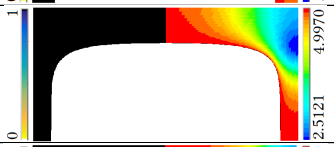		3840.4627	4.9970	0.0608	0.9409
30	6.6666			5505.0547	6.6849	0.2742	0.6061
20	10.000			8828.0825	10.0225	0.2252	0.6270
10	20.000			18815.728	20.0546	0.2728	1.9399

Table B.2: Optimal designs for the minimization of the maximum stress for the $\langle\sigma_1\rangle = 2\langle\sigma_2\rangle$ macroscopic load – Single material Shape Optimization using the k-type Gielis Formula parametrization – Part 2

V [%]	Design Variables	$\sigma^{VM}(\theta)\Big\|_\Gamma/\sigma_\infty$	$10^9 * C^H$	$E^H_{11}(\theta)$
90	$N_{11} = 1.99276$ $N_{12} = 2.14441$ $N_{21} = 1.99754$ $N_{22} = 2.02225$ $N_{31} = 1.97404$ $N_{32} = 2.10110$ $a_1 = 4.13e-2$ $a_2 = 5.34e-3$ $b_1 = 2.17e-2$ $b_2 = 8.25e-3$	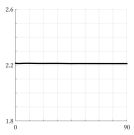	$\begin{bmatrix} 1.206 & -0.380 & 0 \\ -0.380 & 1.495 & 0 \\ 0 & 0 & 0.949 \end{bmatrix}$	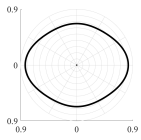
80	$N_{11} = 1.77516$ $N_{12} = 2.31389$ $N_{21} = 1.96322$ $N_{22} = 2.65331$ $N_{31} = 1.93724$ $N_{32} = 2.75417$ $a_1 = 5.95e-2$ $a_2 = 3.30e-2$ $b_1 = 3.76e-2$ $b_2 = 2.20e-2$	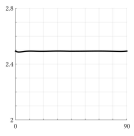	$\begin{bmatrix} 14.57 & -0.451 & 0 \\ -0.451 & 28.27 & 0 \\ 0 & 0 & 4719 \end{bmatrix}$	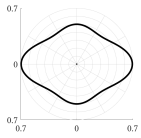
70	$N_{11} = 1.71857$ $N_{12} = 3.67914$ $N_{21} = 1.90192$ $N_{22} = 3.18860$ $N_{31} = 1.83150$ $N_{32} = 3.04650$ $a_1 = 2.49e-2$ $a_2 = 3.63e-2$ $b_1 = 1.35e-2$ $b_2 = 1.96e-2$	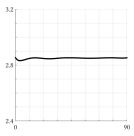	$\begin{bmatrix} 1.716 & -0.447 & 0 \\ -0.447 & 2.578 & 0 \\ 0 & 0 & 2.582 \end{bmatrix}$	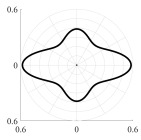
60	$N_{11} = 2.49994$ $N_{12} = 4.65403$ $N_{21} = 4.11109$ $N_{22} = 3.66517$ $N_{31} = 1.83672$ $N_{32} = 3.82612$ $a_1 = 7.27e-2$ $a_2 = 3.15e-2$ $b_1 = 1.97e-3$ $b_2 = 2.46e-2$	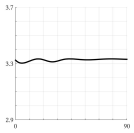	$\begin{bmatrix} 2.078 & -0.453 & 0 \\ -0.453 & 3.305 & 0 \\ 0 & 0 & 5.070 \end{bmatrix}$	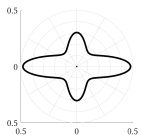
50	$N_{11} = 4.78037$ $N_{12} = 5.71621$ $N_{21} = 3.66022$ $N_{22} = 6.88514$ $N_{31} = 4.17789$ $N_{32} = 5.15750$ $a_1 = 2.35e-2$ $a_2 = 4.89e-2$ $b_1 = 2.97e-2$ $b_2 = 1.27e-2$	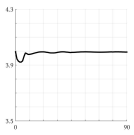	$\begin{bmatrix} 2.579 & -0.455 & 0 \\ -0.455 & 4.304 & 0 \\ 0 & 0 & 11.51 \end{bmatrix}$	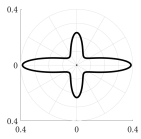
40	$N_{11} = 5.73927$ $N_{12} = 6.16810$ $N_{21} = 3.46219$ $N_{22} = 13.1399$ $N_{31} = 5.91983$ $N_{32} = 4.69346$ $a_1 = 1.08e-2$ $a_2 = 1.65e-1$ $b_1 = 5.63e-2$ $b_2 = 6.52e-3$	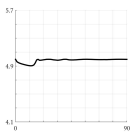	$\begin{bmatrix} 3.331 & -0.455 & 0 \\ -0.455 & 5.794 & 0 \\ 0 & 0 & 30.85 \end{bmatrix}$	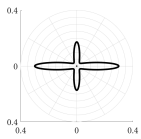
30	$N_{11} = 5.78583$ $N_{12} = 11.7792$ $N_{21} = 5.17688$ $N_{22} = 12.4782$ $N_{31} = 7.92193$ $N_{32} = 9.17411$ $a_1 = 2.05e-2$ $a_2 = 6.92e-2$ $b_1 = 7.02e-2$ $b_2 = 2.34e-2$	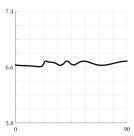	$\begin{bmatrix} 4.579 & -0.454 & 0 \\ -0.454 & 8.299 & 0 \\ 0 & 0 & 101.9 \end{bmatrix}$	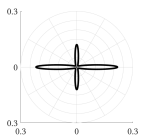
20	$N_{11} = 12.6367$ $N_{12} = 15.6486$ $N_{21} = 8.96475$ $N_{22} = 19.8344$ $N_{31} = 12.4869$ $N_{32} = 15.5960$ $a_1 = 1.28e-2$ $a_2 = 9.09e-2$ $b_1 = 4.07e-2$ $b_2 = 4.40e-2$	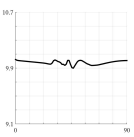	$\begin{bmatrix} 7.066 & -0.453 & 0 \\ -0.453 & 13.31 & 0 \\ 0 & 0 & 466.9 \end{bmatrix}$	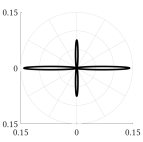
10	$N_{11} = 19.7296$ $N_{12} = 37.8291$ $N_{21} = 24.5525$ $N_{22} = 33.4730$ $N_{31} = 18.8192$ $N_{32} = 38.7323$ $a_1 = 5.99e-2$ $a_2 = 4.68e-2$ $b_1 = 2.84e-2$ $b_2 = 6.39e-2$	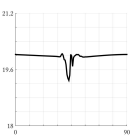	$\begin{bmatrix} 14.57 & -0.451 & 0 \\ -0.451 & 28.27 & 0 \\ 0 & 0 & 4719 \end{bmatrix}$	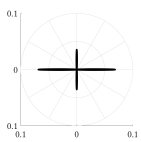

B.2 MMSO - Superellipse Parametrization

Table B.3: Optimal designs for the minimization of the maximum stress for the $\langle\sigma_1\rangle = 2\langle\sigma_2\rangle$ macroscopic load – Multi-material Shape Optimization using the superellipse parametrization – Part 1

V [%]	$\sigma_{Max}^{Theo.}$	E/E_{Max}	$\sigma^{VM}/\sigma_\infty$	w $[J/m^3]$	$\sigma_{Max}^{VM}/\sigma_\infty$	Reduction [%]
99	2.0202	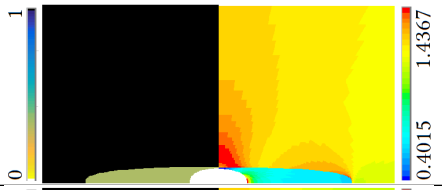		914.1909	1.4367	28.88
95	2.1053			1070.4752	1.6414	22.03
90	2.2222	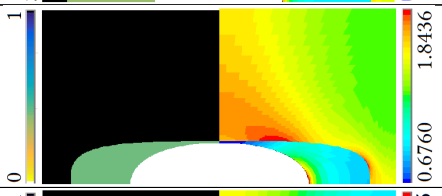		1198.7442	1.8436	17.03
80	2.5000	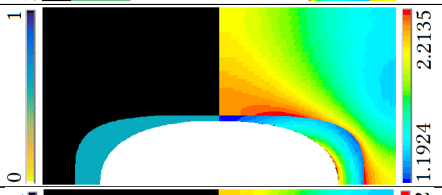		1469.2935	2.2135	11.46
70	2.8571	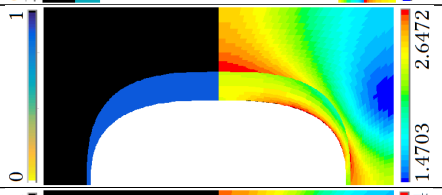		1771.5671	2.6472	7.34
60	3.3333	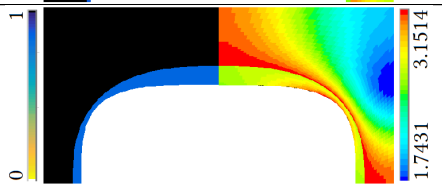		2249.3975	3.1514	5.46

Table B.4: Optimal designs for the minimization of the maximum stress for the $\langle\sigma_1\rangle = 2\langle\sigma_2\rangle$ macroscopic load – Multi-material Shape Optimization using the superellipse parametrization – Part 2

V [%]	Design Variables	$\sigma^{VM}(\theta)\Big\|_{\Gamma_1,\Gamma_2}/\sigma_\infty$	$10^9 * C^H$	$E^H_{11}(\theta)$
99	$N_1 = 2.29945$ $N_2 = 2.64605$ $a_1 = 0.54721*$ $a_2 = 1.26299*$ $3.0e-02$ $6.0e-02$ $b_1 = 0.51225*$ $b_2 = 0.43419*$ $1.5e-02$ $2.0e-02$ $E_1 = 0.31340E_2$	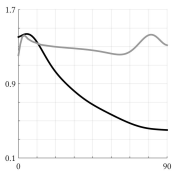	$\begin{bmatrix} 1.050 & -0.318 & 0 \\ -0.318 & 1.185 & 0 \\ 0 & 0 & 0.758 \end{bmatrix}$	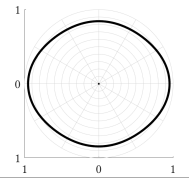
95	$N_1 = 2.35640$ $N_2 = 3.57218$ $a_1 = 0.90780*$ $a_2 = 1.07931*$ $4.0e-02$ $8.0e-02$ $b_1 = 0.82869*$ $b_2 = 0.75955*$ $1.8e-02$ $2.3e-02$ $E_1 = 0.35261E_2$	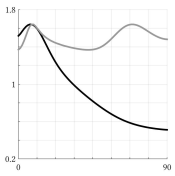	$\begin{bmatrix} 1.157 & -0.355 & 0 \\ -0.355 & 1.608 & 0 \\ 0 & 0 & 1.026 \end{bmatrix}$	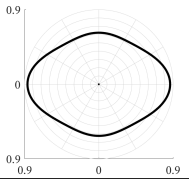
90	$N_1 = 2.20609$ $N_2 = 3.76710$ $a_1 = 1.01678*$ $a_2 = 1.41884*$ $5.0e-02$ $6.0e-02$ $b_1 = 0.96699*$ $b_2 = 0.84573*$ $2.5e-02$ $3.0e-02$ $E_1 = 0.40954E_2$	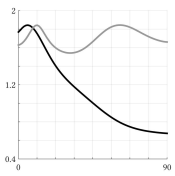	$\begin{bmatrix} 1.246 & -0.382 & 0 \\ -0.382 & 1.939 & 0 \\ 0 & 0 & 1.271 \end{bmatrix}$	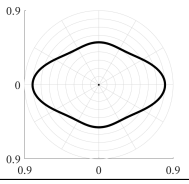
80	$N_1 = 2.37445$ $N_2 = 3.83856$ $a_1 = 1.12135*$ $a_2 = 1.02297*$ $6.0e-02$ $8.0e-02$ $b_1 = 0.79276*$ $b_2 = 0.71192*$ $4.5e-02$ $5.5e-02$ $E_1 = 0.57164E_2$	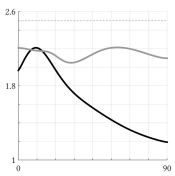	$\begin{bmatrix} 1.464 & -0.420 & 0 \\ -0.420 & 2.435 & 0 \\ 0 & 0 & 1.879 \end{bmatrix}$	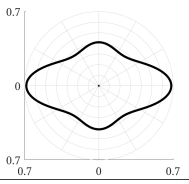
70	$N_1 = 2.80415$ $N_2 = 2.99241$ $a_1 = 0.97091*$ $a_2 = 0.88603*$ $8.0e-02$ $9.0e-02$ $b_1 = 0.94688*$ $b_2 = 0.98085*$ $5.5e-02$ $6.5e-02$ $E_1 = 0.84526E_2$	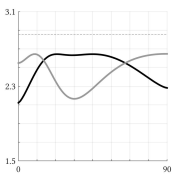	$\begin{bmatrix} 1.770 & -0.440 & 0 \\ -0.440 & 2.653 & 0 \\ 0 & 0 & 2.839 \end{bmatrix}$	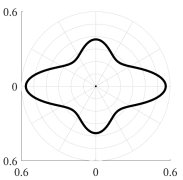
60	$N_1 = 3.87209$ $N_2 = 2.69007$ $a_1 = 0.97383*$ $a_2 = 0.92478*$ $8.0e-02$ $9.0e-02$ $b_1 = 0.92722*$ $b_2 = 0.95198*$ $6.0e-02$ $7.0e-02$ $E_1 = 0.83709E_2$	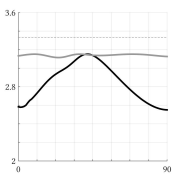	$\begin{bmatrix} 2.120 & -0.442 & 0 \\ -0.442 & 3.415 & 0 \\ 0 & 0 & 5.811 \end{bmatrix}$	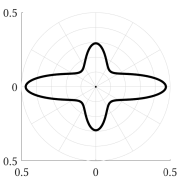

B.3 MMSO - Supershape Parametrization

Table B.5: Optimal designs for the minimization of the maximum stress for the $\langle\sigma_1\rangle = 2\langle\sigma_2\rangle$ macroscopic load – Multi-material Shape Optimization using the supershape parametrization – Part 1

V [%]	$\sigma_{Max}^{Theo.}$	E/E_{Max}	$\sigma^{VM}/\sigma_\infty$	w $[J/m^3]$	$\sigma_{Max}^{VM}/\sigma_\infty$	Reduction [%]
99	2.0202			941.9517	1.4293	29.25
95	2.1053	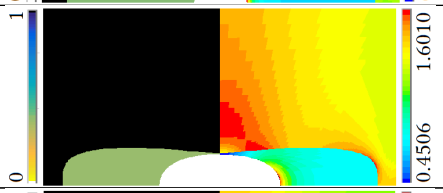		1098.8338	1.6010	23.95
90	2.2222	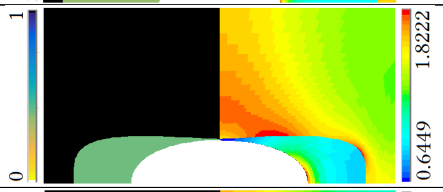		1075.8468	1.8222	18.00
80	2.5000	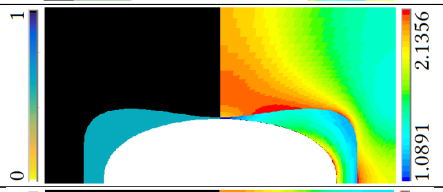		1474.7510	2.1356	14.58
70	2.8571	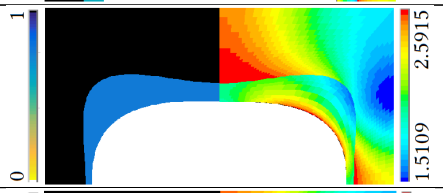		1831.5594	2.5915	9.30
60	3.3333	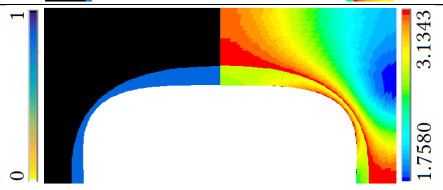		2251.6658	3.1346	5.96

Table B.6: Optimal designs for the minimization of the maximum stress for the $\langle\sigma_1\rangle = 2\langle\sigma_2\rangle$ macroscopic load – Multi-material Shape Optimization using the supershape parametrization – Part 2

V [%]	Design Variables	$\sigma^{VM}(\theta)\Big\|_{\Gamma_1,\Gamma_2}/\sigma_\infty$	$10^9 * C^H$	$E^H_{11}(\theta)$
99	$N_{11} = 2.23847$ $N_{12} = 2.45499$ $N_{21} = 2.29795$ $N_{22} = 2.48023$ $N_{31} = 2.34517$ $N_{32} = 3.02595$ $a_1 = 0.54732*$ $a_2 = 1.47590*$ $b_1 = 0.49675*$ $b_2 = 0.39634*$ $E_1 = 0.37529E_2$	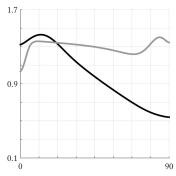	$\begin{bmatrix} 1.080 & -0.326 & 0 \\ -0.326 & 1.222 & 0 \\ 0 & 0 & 0.791 \end{bmatrix}$	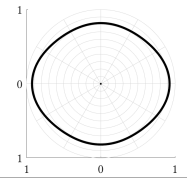
95	$N_{11} = 2.39203$ $N_{12} = 3.25527$ $N_{21} = 2.43948$ $N_{22} = 3.34770$ $N_{31} = 2.32086$ $N_{32} = 3.95514$ $a_1 = 0.91429*$ $a_2 = 1.19949*$ $b_1 = 0.91814*$ $b_2 = 1.64151*$ $E_1 = 0.35331E_2$	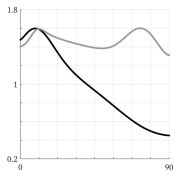	$\begin{bmatrix} 1.118 & -0.358 & 0 \\ -0.358 & 1.654 & 0 \\ 0 & 0 & 1.081 \end{bmatrix}$	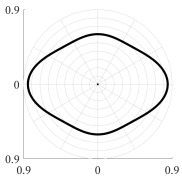
90	$N_{11} = 2.31536$ $N_{12} = 3.68235$ $N_{21} = 2.26324$ $N_{22} = 3.75802$ $N_{31} = 2.20994$ $N_{32} = 4.18707$ $a_1 = 0.93913*$ $a_2 = 1.09803*$ $b_1 = 0.82266*$ $b_2 = 1.32502*$ $E_1 = 0.41220E_2$	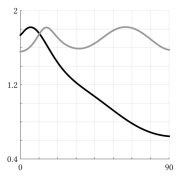	$\begin{bmatrix} 1.164 & -0.348 & 0 \\ -0.348 & 1.581 & 0 \\ 0 & 0 & 0.975 \end{bmatrix}$	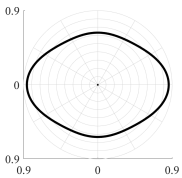
80	$N_{11} = 2.80039$ $N_{12} = 3.64307$ $N_{21} = 2.37163$ $N_{22} = 4.19153$ $N_{31} = 2.40550$ $N_{32} = 5.11810$ $a_1 = 0.67728*$ $a_2 = 1.35943*$ $b_1 = 0.46904*$ $b_2 = 1.75197*$ $E_1 = 0.83709E_2$	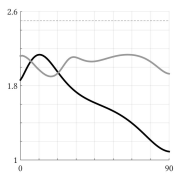	$\begin{bmatrix} 1.481 & -0.420 & 0 \\ -0.420 & 2.391 & 0 \\ 0 & 0 & 1.871 \end{bmatrix}$	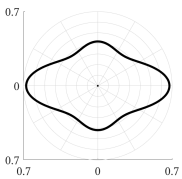
70	$N_{11} = 2.30546$ $N_{12} = 3.49993$ $N_{21} = 2.86199$ $N_{22} = 4.57056$ $N_{31} = 2.63663$ $N_{32} = 5.23018$ $a_1 = 1.66514*$ $a_2 = 1.86378*$ $b_1 = 1.44835*$ $b_2 = 2.31543*$ $E_1 = 0.76826E_2$	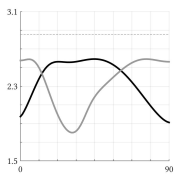	$\begin{bmatrix} 1.810 & -0.441 & 0 \\ -0.441 & 2.768 & 0 \\ 0 & 0 & 3.052 \end{bmatrix}$	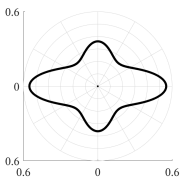
60	$N_{11} = 3.05603$ $N_{12} = 3.55773$ $N_{21} = 5.00439$ $N_{22} = 3.29131$ $N_{31} = 2.99754$ $N_{32} = 2.70281$ $a_1 = 2.54895*$ $a_2 = 0.71113*$ $b_1 = 0.81201*$ $b_2 = 0.33824*$ $E_1 = 0.83709E_2$	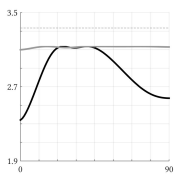	$\begin{bmatrix} 2.115 & -0.442 & 0 \\ -0.442 & 3.439 & 0 \\ 0 & 0 & 5.924 \end{bmatrix}$	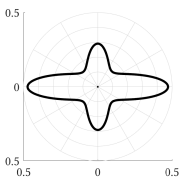

B.4 Variable Thickness Plate Approach

Table B.7: Optimal designs for the minimization of the maximum stress for the $\langle\sigma_1\rangle = 2\langle\sigma_2\rangle$ macroscopic load – Variable thickness plate approach – Part 1

V [%]	$\sigma_{Max}^{Theo.}$	E/E_{Max}	$\sigma^{VM}/\sigma_\infty$	w $[J/m^3]$	$\sigma_{Max}^{VM}/\sigma_\infty$	Reduction [%]
99	2.0202	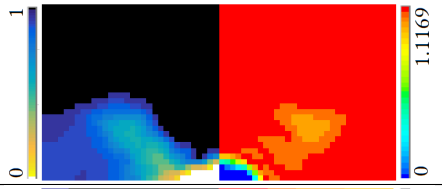		867.7284	1.1169	44.71
95	2.1053	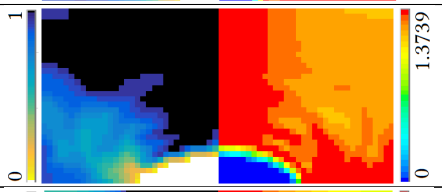		1128.9648	1.3739	34.74
90	2.2222	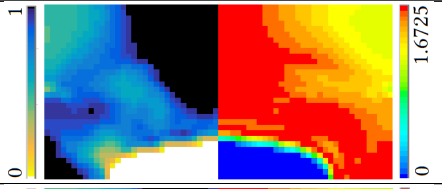		1511.7336	1.6725	24.74
80	2.5000	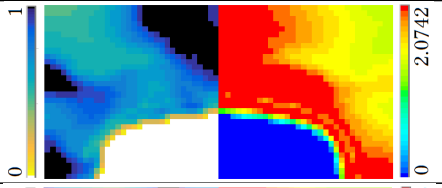		2006.3524	2.0742	17.03
70	2.8571	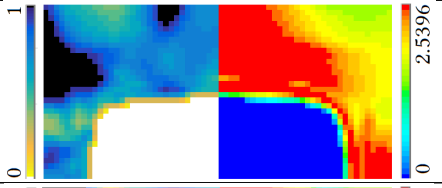		2652.3728	2.5396	11.11
60	3.3333	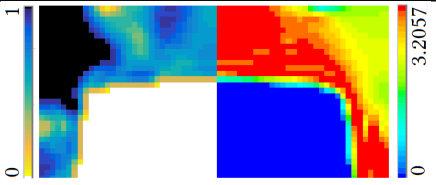		3398.7144	3.2057	3.83

Table B.8: Optimal designs for the minimization of the maximum stress for the $\langle\sigma_1\rangle = 2\langle\sigma_2\rangle$ macroscopic load – Variable thickness plate approach – Part 2

V [%]	Initial Design	$10^9 * C^H$	$E^H_{11}(\theta)$	Initial Design
99	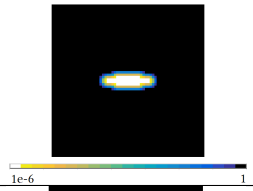	$\begin{bmatrix} 1.130 & -0.351 & 0 \\ -0.351 & 1.309 & 0 \\ 0 & 0 & 0.803 \end{bmatrix}$	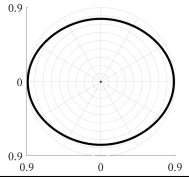	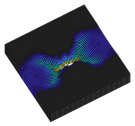
95	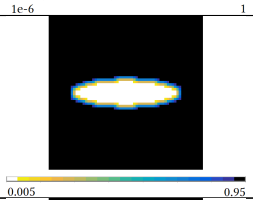	$\begin{bmatrix} 1.249 & -0.408 & 0 \\ -0.408 & 1.941 & 0 \\ 0 & 0 & 1.106 \end{bmatrix}$	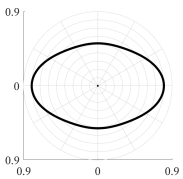	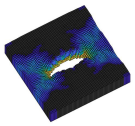
90	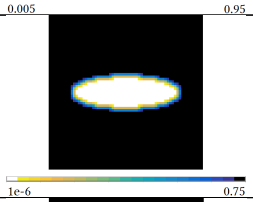	$\begin{bmatrix} 1.561 & -0.561 & 0 \\ -0.561 & 2.806 & 0 \\ 0 & 0 & 1.549 \end{bmatrix}$	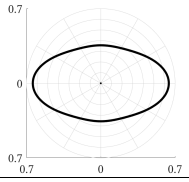	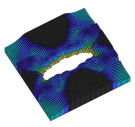
80	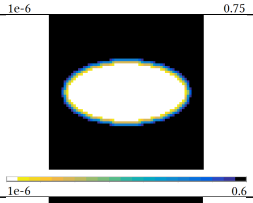	$\begin{bmatrix} 2.089 & -0.670 & 0 \\ -0.670 & 3.354 & 0 \\ 0 & 0 & 2.542 \end{bmatrix}$	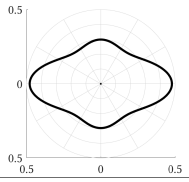	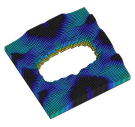
70	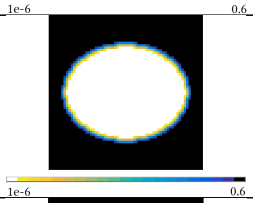	$\begin{bmatrix} 2.453 & -0.510 & 0 \\ -0.510 & 4.164 & 0 \\ 0 & 0 & 5.660 \end{bmatrix}$	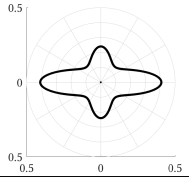	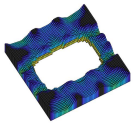
60	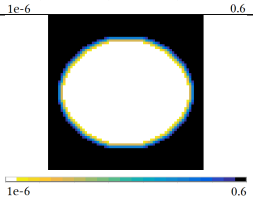	$\begin{bmatrix} 3.063 & -0.428 & 0 \\ -0.428 & 4.755 & 0 \\ 0 & 0 & 10.49 \end{bmatrix}$	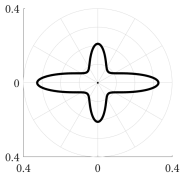	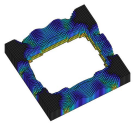

Appendix C

Optimal Designs - Shear Load

C.1 SMSO - Minimization of Strain Energy

Table C.1: Optimal designs for the minimization of the strain energy for the $\langle\sigma_1\rangle = -\langle\sigma_2\rangle$ macroscopic load – Single Material Shape Optimization using the supershape parametrization – Part 1

V [%]	E/E_{Max}	$\sigma^{VM}/\sigma_\infty$	w $[J/m^3]$	$\sigma^{VM}_{Max}/\sigma_\infty$
90	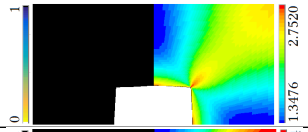		1657.7420	2.7520
80	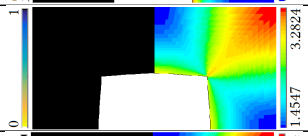		2015.8429	3.2824
70	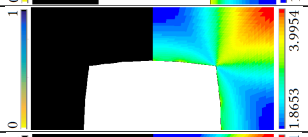		2417.0229	3.9954
60	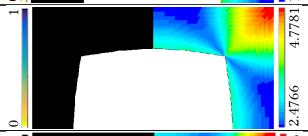		2912.6789	4.7781
50	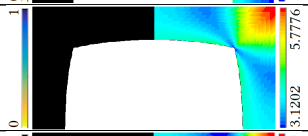		3585.3223	5.7776
40	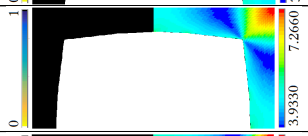		4585.1458	7.2660
30			6268.5579	9.9320
20	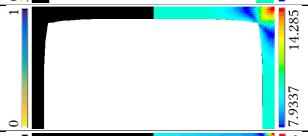		9579.3166	14.2854
10			19639.6649	31.8132

Table C.2: Optimal designs for the minimization of the strain energy for the $\langle\sigma_1\rangle = -\langle\sigma_2\rangle$ macroscopic load – Single Material Shape Optimization using the supershape parametrization – Part 2

V [%]	Design Variables	$10^9 * C^H$	$E^H_{11}(\theta)$
90	$N_1 = 4.50547$ $N_2 = 4.02469$ $N_3 = 4.12400$ $a_1 = 4.34e-2$ $b_1 = 2.35e-2$	$\begin{bmatrix} 1.311 & -0.350 & 0 \\ -0.350 & 1.311 & 0 \\ 0 & 0 & 1.017 \end{bmatrix}$	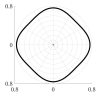
80	$N_1 = 7.50886$ $N_2 = 1.58022$ $N_3 = 6.26760$ $a_1 = 7.30e-1$ $b_1 = 2.49e-2$	$\begin{bmatrix} 1.643 & -0.373 & 0 \\ -0.373 & 1.643 & 0 \\ 0 & 0 & 1.702 \end{bmatrix}$	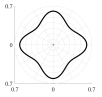
70	$N_1 = 3.83646$ $N_2 = 2.34381$ $N_3 = 2.98467$ $a_1 = 7.54e-2$ $b_1 = 2.49e-2$	$\begin{bmatrix} 2.027 & -0.390 & 0 \\ -0.390 & 2.027 & 0 \\ 0 & 0 & 2.954 \end{bmatrix}$	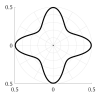
60	$N_1 = 3.33799$ $N_2 = 3.10067$ $N_3 = 2.45226$ $a_1 = 1.95e-1$ $b_1 = 2.46e-2$	$\begin{bmatrix} 2.510 & -0.402 & 0 \\ -0.402 & 2.510 & 0 \\ 0 & 0 & 5.338 \end{bmatrix}$	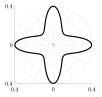
50	$N_1 = 3.65743$ $N_2 = 1.42656$ $N_3 = 2.76356$ $a_1 = 1.44e-2$ $b_1 = 3.16e-2$	$\begin{bmatrix} 3.179 & -0.406 & 0 \\ -0.406 & 3.179 & 0 \\ 0 & 0 & 10.60 \end{bmatrix}$	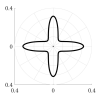
40	$N_1 = 2.68878$ $N_2 = 1.70457$ $N_3 = 2.13431$ $a_1 = 1.49e-1$ $b_1 = 4.16e-2$	$\begin{bmatrix} 4.188 & -0.400 & 0 \\ -0.400 & 4.188 & 0 \\ 0 & 0 & 24.41 \end{bmatrix}$	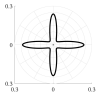
30	$N_1 = 3.35547$ $N_2 = 1.26462$ $N_3 = 2.82509$ $a_1 = 4.93e-1$ $b_1 = 5.40e-2$	$\begin{bmatrix} 5.883 & -0.386 & 0 \\ -0.386 & 5.883 & 0 \\ 0 & 0 & 71.36 \end{bmatrix}$	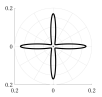
20	$N_1 = 3.82052$ $N_2 = 4.21327$ $N_3 = 3.94783$ $a_1 = 1.60e-1$ $b_1 = 9.72e-1$	$\begin{bmatrix} 9.168 & -0.411 & 0 \\ -0.411 & 9.168 & 0 \\ 0 & 0 & 286.0 \end{bmatrix}$	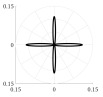
10	$N_1 = 4.94184$ $N_2 = 4.38887$ $N_3 = 4.85204$ $a_1 = 2.48e-1$ $b_1 = 9.12e-2$	$\begin{bmatrix} 19.26 & -0.379 & 0 \\ -0.379 & 19.26 & 0 \\ 0 & 0 & 2919 \end{bmatrix}$	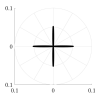

C.2 SMSO - Minimization of Maximum Stress

Table C.3: Optimal designs for the minimization of the maximum equivalent stress for the $\langle\sigma_1\rangle = -\langle\sigma_2\rangle$ macroscopic load – Single Material Shape Optimization using the supershape parametrization – Part 1

V [%]	E/E_{Max}	$\sigma^{VM}/\sigma_\infty$	w [J/m^3]	$\sigma^{VM}_{Max}/\sigma_\infty$
90	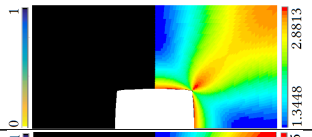		1655.23	2.8813
80	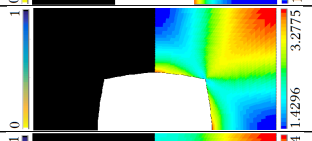		2019.07	3.2775
70	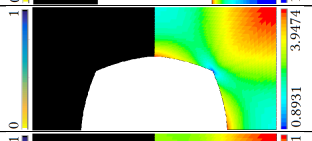		2441.69	3.9474
60	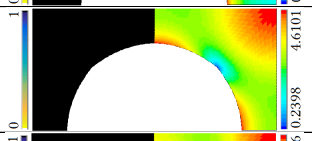		3021.68	4.6101
50	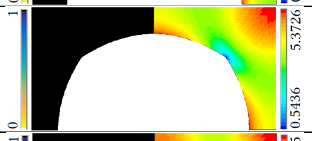		3696.75	5.3726
40	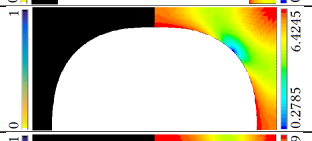		4829.02	6.4245
30	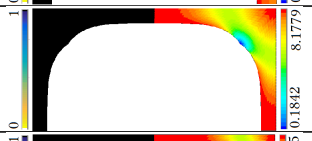		6608.09	8.1779
20			10030.0	11.5946
10			20105.8	21.6176

Table C.4: Optimal designs for the minimization of the maximum equivalent stress for the $\langle\sigma_1\rangle = -\langle\sigma_2\rangle$ macroscopic load – Single Material Shape Optimization using the supershape parametrization – Part 2

V [%]	Design Variables	$10^9 * C^H$	$E^H_{11}(\theta)$
90	$N_1 = 4.50547$ $N_2 = 4.02469$ $N_3 = 4.12400$ $a_1 = 7.82e-2$ $b_1 = 3.14e-2$	$\begin{bmatrix} 1.304 & -0.351 & 0 \\ -0.351 & 1.304 & 0 \\ 0 & 0 & 1.003 \end{bmatrix}$	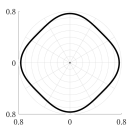
80	$N_1 = 7.50886$ $N_2 = 1.58022$ $N_3 = 6.26760$ $a_1 = 6.73e-2$ $b_1 = 3.59e-2$	$\begin{bmatrix} 1.629 & -0.390 & 0 \\ -0.390 & 1.629 & 0 \\ 0 & 0 & 1.585 \end{bmatrix}$	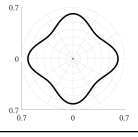
70	$N_1 = 3.83646$ $N_2 = 2.34381$ $N_3 = 2.98467$ $a_1 = 1.05e-1$ $b_1 = 3.38e-2$	$\begin{bmatrix} 2.005 & -0.436 & 0 \\ -0.436 & 2.005 & 0 \\ 0 & 0 & 2.418 \end{bmatrix}$	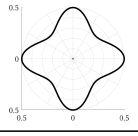
60	$N_1 = 3.33799$ $N_2 = 3.10067$ $N_3 = 2.45226$ $a_1 = 9.59e-2$ $b_1 = 7.83e-3$	$\begin{bmatrix} 2.538 & -0.483 & 0 \\ -0.483 & 2.538 & 0 \\ 0 & 0 & 3.796 \end{bmatrix}$	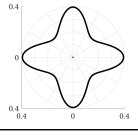
50	$N_1 = 3.65743$ $N_2 = 1.42656$ $N_3 = 2.76356$ $a_1 = 1.01e-1$ $b_1 = 1.77e-2$	$\begin{bmatrix} 3.215 & -0.482 & 0 \\ -0.482 & 3.215 & 0 \\ 0 & 0 & 7.398 \end{bmatrix}$	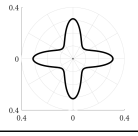
40	$N_1 = 2.68878$ $N_2 = 1.70457$ $N_3 = 2.13431$ $a_1 = 4.39e-1$ $b_1 = 3.38e-2$	$\begin{bmatrix} 4.331 & -0.498 & 0 \\ -0.498 & 4.331 & 0 \\ 0 & 0 & 17.29 \end{bmatrix}$	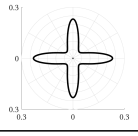
30	$N_1 = 3.35547$ $N_2 = 1.26462$ $N_3 = 2.82509$ $a_1 = 1.47e-1$ $b_1 = 7.93e-2$	$\begin{bmatrix} 6.103 & -0.505 & 0 \\ -0.505 & 6.103 & 0 \\ 0 & 0 & 54.33 \end{bmatrix}$	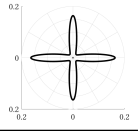
20	$N_1 = 3.82052$ $N_2 = 4.21327$ $N_3 = 3.94783$ $a_1 = 2.08e-1$ $b_1 = 9.08e-2$	$\begin{bmatrix} 9.524 & -0.506 & 0 \\ -0.506 & 9.524 & 0 \\ 0 & 0 & 250.2 \end{bmatrix}$	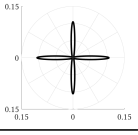
10	$N_1 = 4.94184$ $N_2 = 4.38887$ $N_3 = 4.85204$ $a_1 = 6.79e-3$ $b_1 = 9.54e-2$	$\begin{bmatrix} 19.60 & -0.505 & 0 \\ -0.505 & 19.60 & 0 \\ 0 & 0 & 2563 \end{bmatrix}$	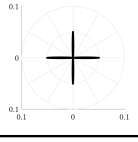

C.3 Variable Thickness Plate Approach - Minimization of Maximum Stress

Table C.5: Optimal designs for the minimization of the maximum equivalent stress for the $\langle\sigma_1\rangle = -\langle\sigma_2\rangle$ macroscopic load – Variable thickness plate approach – Part 1

V [%]	E/E_{Max}	$\sigma^{VM}/\sigma_\infty$	w $[J/m^3]$	$\sigma^{VM}_{Max}/\sigma_\infty$
95	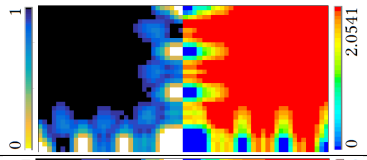		1700.6453	2.0541
90	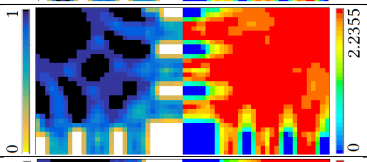		2052.8983	2.2355
80	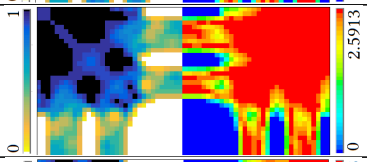		3165.9249	2.5913
70	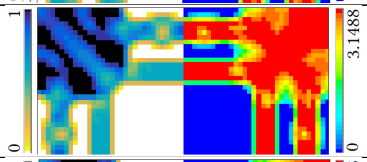		3901.2150	3.1488
60	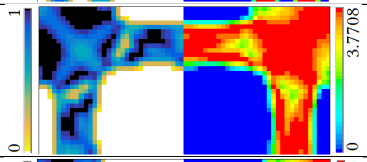		4055.6482	3.7708
50	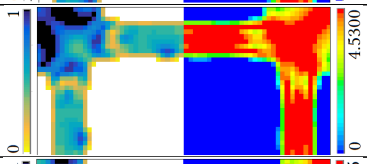		6866.9235	4.5300
40	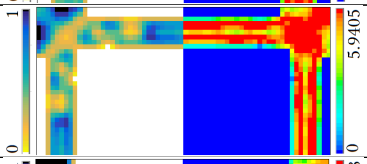		12053.2822	5.9405
30	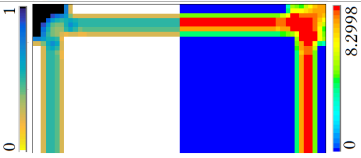		14570.4113	8.2998

Table C.6: Optimal designs for the minimization of the maximum equivalent stress for the $\langle\sigma_1\rangle = -\langle\sigma_2\rangle$ macroscopic load – Variable thickness plate approach – Part 2

V [%]	Initial Design	$10^9 * C^H$	$E^H_{11}(\theta)$	Initial Design
95	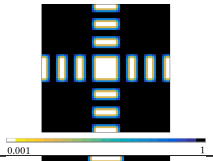	$\begin{bmatrix} 1.357 & -0.344 & 0 \\ -0.344 & 1.357 & 0 \\ 0 & 0 & 1.269 \end{bmatrix}$	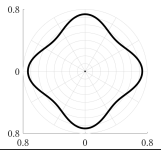	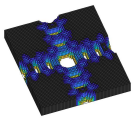
90	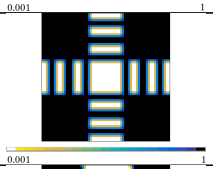	$\begin{bmatrix} 1.694 & -0.359 & 0 \\ -0.359 & 1.694 & 0 \\ 0 & 0 & 2.842 \end{bmatrix}$	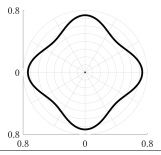	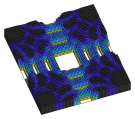
80	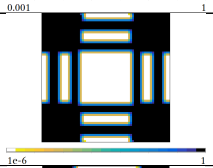	$\begin{bmatrix} 2.776 & -0.390 & 0 \\ -0.390 & 2.776 & 0 \\ 0 & 0 & 8.173 \end{bmatrix}$	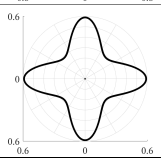	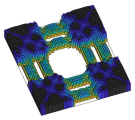
70	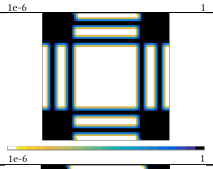	$\begin{bmatrix} 3.500 & -0.401 & 0 \\ -0.401 & 3.500 & 0 \\ 0 & 0 & 29.33 \end{bmatrix}$	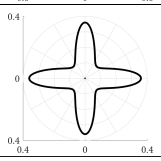	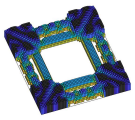
60	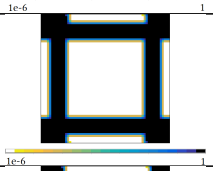	$\begin{bmatrix} 3.602 & -0.454 & 0 \\ -0.454 & 3.602 & 0 \\ 0 & 0 & 17.70 \end{bmatrix}$	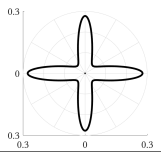	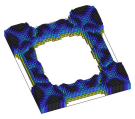
50	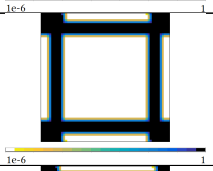	$\begin{bmatrix} 6.401 & -0.466 & 0 \\ -0.466 & 6.401 & 0 \\ 0 & 0 & 68.64 \end{bmatrix}$	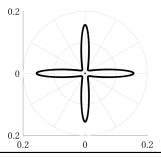	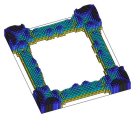
40	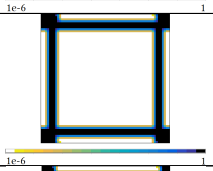	$\begin{bmatrix} 11.10 & -0.957 & 0 \\ -0.957 & 11.10 & 0 \\ 0 & 0 & 304.9 \end{bmatrix}$	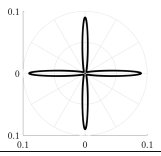	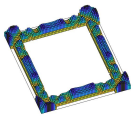
30	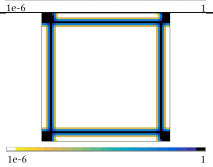	$\begin{bmatrix} 14.05 & -0.518 & 0 \\ -0.518 & 14.05 & 0 \\ 0 & 0 & 800.9 \end{bmatrix}$